https://mrs2021.sciencesconf.org

26th and 27th October 2021

Strasbourg

Amphitheater of Collège Doctoral Européen

The Institute for Earth & Environment of the CNRS & the University of Strasbourg, welcome participants from universities, research institutes, state geological surveys, governmental authorities as well as from companies.

Organized in hybrid form (**both on-site and visio-conference**), the meeting will take place **from 26 to 27 October 2021,** two days exchanging on use of magnetic resonance methods for near surface investigations, particularly for those related to groundwater.

Many new developments will be addressed under topics covering measurement technology, signal processing, modelling, and inversion as well as for NMR rock physics or soil sciences. A large number of case studies in different hydrogeological settings and exploration objectives will highlight again the usefulness and power of the method and the information gained.

This event is sponsored by the CNRS, the University of Strasbourg and Mission Investissement d'Avenir, and ADEME (French Agency of Energy and Environment), and IRIS-Instruments.

Contact: mrs2021@sciencesconf.org

Comittees

Local organization comittee

Jean-François Girard, ITES/University of Strasbourg.

Nolwenn Lesparre, ITES/University of Strasbourg.

Anatoly Legchenko, IRD, Grenoble.

Scientific comittee

Jakob Juul Larsen, Aarhus university, Denmark.

Denys Grombacher, Aarhus university, Denmark.

Ling Wan, Jilin university, China.

Naomi Mazzilli, University of Avignon, France.

Marie Boucher, IRD, France / Niger.

Mike Mueller-Petke, LIAG Hannover, Germany.

Tingting Lin, Jilin university, China.

Jean Roy, IGP, Canada.

Jean-Michel Baltassat, BRGM, France.

Frederic Nguyen, University of Liège, Belgium.

Jean Bernard, Olivet, France.

MRS2021 - Detailed technical program

Session	Speaker	TITLE
Tue 26 / 9h (CET)	Organizing comittee	Welcome & introduction
Tue 26 / 9h-10h30 (CET) ***Case studies & monitoring***	Li Kaitian	The use of Surface Nuclear Magnetic Resonance to characterize the alluvium of the Er Mine in Kuche, China
	Bertrand Mathieu	Groundwater fast drainage dynamics in the Barrois limestones; evidences from an MRS monitoring.
	Yang Zhang	Noise attenuation of magnetic resonance sounding signal using fully convolutional networks
	Costabel Stephan	First field experiences using surface nuclear magnetic resonance with prepolarization (SNMR-PP)
	Hanqing Zhao	The Progress of Shutoff Circuit Design and Estimation for Pre-polarization SNMR Technique
Tue 26 / 11h-12h30 (CET) ***Borehole NMR & noise reduction***	Shushakov Oleg	Heat exchange impact on NMR logging while drilling
	Gaikwad Nikhil	Thermal Model of the Apsu Transmitter for Lightweight and Compact Heat Sink Design
	Legchenko Anatoly	Surface-Borehole NMR Sensor
	Michel Hadrien	Application of BEL1D for sNMR data interpretation
	Pengfei Wang	A Special Construction Loop for Harmonic Noise Cancellation in Situ
	Larsen Jakob Juul	Mitigation of powerline noise in surface NMR data: Estimation of the fundamental frequency using convolutional neural networks
Tue 26 / 14h-15h30 (CET) ***Case studies & monitoring***	Lutz Pascale	Study and characterization of the groundwater resource of the Sandricourt domain (Oise, France) using Magnetic Resonance Sounding and Electrical Resistivity Tomography
	Vang Mathias	Resolving regional variations in groundwater table using SNMR
	Girard Jean-François	Magnetic resonance in weathered & fractured granite aquifer: case studies in Alsace
	Irons Trevor	Small-loop surface NMR and high resolution ERT soil evolution monitoring at the Midtre Lovenbreen glacial forefield in Ny-Alesund, Svalbard
	Baltassat Jean-Michel	3-D SNMR monitoring of the Tête-Rousse glacier - 2012-2018
Tuesday 26/10 ***evening***	on-site participants	City Tour Gala dinner
Wed 27 / 9h-10h30 (CET) ***MRS & hydro models***	Li Yulin	Application of Magnetic Resonance Soundind and Electrical Resistivity Tomography to investigate the lateral seepage of the Yellow River in Liaocheng area, China
	Lesparre Nolwenn	Global sensitivity analysis of Magnetic Resonance Sounding simulated responses to the hydraulic parameters of a catchment hydrogeological model
	Shushakov Oleg	Examples of the Bloch-Siegert effect in MRS
	Skibbe Nico	COMET - A toolbox for modelling and inversion of surface SNMR
	Legchenko Anatoly	Investigation on unsaturated water flow in karst limestone of the Beauce aquifer (France) using time-lapse MRS measurements
Wed 27 / 11h-12h30 (CET) ***Advanced sequences & modeling***	Grombacher Denys	A steady-state approach to surface NMR
	Hiller Thomas	Accounting for the excitation pulse shape in modelling prepolarized surface nuclear magnetic resonance (SNMR-PP)
	Griffiths Matthew	A surface NMR forward model for steady-state free-precession excitations
	Mueller-Petke Mike	State-of-the-art and progress using prepolarization for surface Nuclear-Magnetic-Resonance
	Liu Lichao	Signal extraction of surface NMR steady-state free precession sequence data
Wed 27 / 14h-14h45 (CET) ***Discussion & Outlooks***	remote & on-site participants	Discussion about the state of the art - trends - future developments and several topics to be proposed
Wed 27 / 15h-17h00 (CET) ***Overview of MRS softwares***	remote & on-site participants	Short demonstrations of available MRS softwares (opensource or free). Planned software & speakers: Akvo : T. Irons MRSmatlab : N. Skibbe Comet : M. Müller-Petke Samovar : A. Legchenko

Table of contents

Groundwater fast drainage dynamics in the Barrois limestones; evidences from an MRS monitoring.

[1-3]Bertrand Mathieu [2]Valois Rémi [2]Mazzilli Naomi [3]Gigleux Sylvain
[1-3]Lise-Marie Girod [1]Denimal Sophie [1]Bertrand Catherine
[2]Chalikakis Konstantinos

[1] University of Franche-Comté
Besançon, France
Mathieu.bertrand@univ-fcomte.fr

[2] University of Avignon
Avignon, France

[3]Andra
Bure, France

SUMMARY

MRS geophysical investigations were carried out in fractured and karstified limestones of the Barrois (Meuse). The measurements were reproduced under various hydrological conditions. The main result is the presence of water at very low levels, which has never been quantified before by this method.

Key words: MRS, Barrois limestone, Low water content.

INTRODUCTION

One of the mission of Andra, the French national agency for radioactive waste management, is to study and develop solutions for sustainable management of radioactive waste that do not yet have a final disposal method. In this context, Andra has been carrying out research to design the deep geological repository for high level and intermediate-level long-lived radioactive waste. This project, called Cigéo (Centre Industriel de stockage GÉOlogique), should be built in the interdepartmental area of Meuse - Haute Marne near the Andra underground research laboratory in Bure town. Figure 1, below, shows the geographical location of the study site.

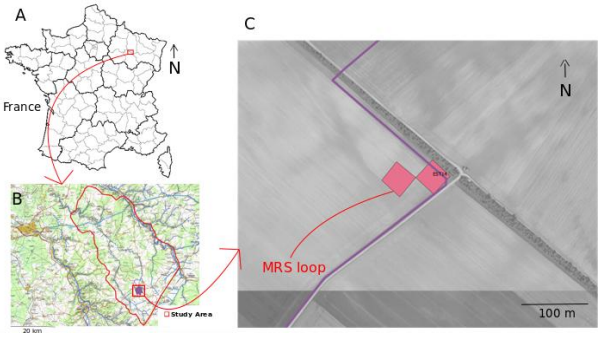

Figure 1. Location of the study site (A and B) and positioning of the MRS loop (C).

Within the framework of the surface infrastructures installation impact assessment in connection with the Cigéo project, Andra is seeking to refine the characterisation of the flow dynamics within the Barrois limestones, formations of Tithonian age present in the outcrop in this area (ANDRA 2011). Several MRS (Magnetic Resonance Sounding) campaigns were carried out between 2014 and 2017. They revealed that the hydrosystem of the Barrois limestones contains very little water. However, signal-to-noise ratio conditions during these campaigns only allowed to quantify the upper limit of these water contents.

METHODS

This abstract presents the results of a monitoring conducted in summer 2021. The monitoring was done in order to follow the effect of rainfall on the Barrois limestone. It was carried out after a fine mapping of electromagnetic noise over the whole area, shown in figure 2. This has allowed the identification of the most favourable zones for data acquisition via the MRS method.

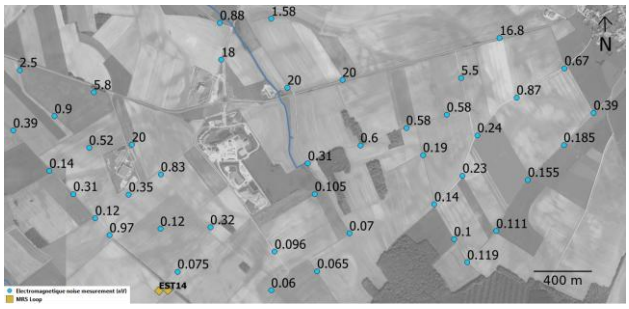

Figure 2. Distribution of electromagnetic noise measurements in preparation for monitoring.

The monitoring comprises 6 soundings in a lapse of time of 38 days (table 1). During this period, the cumulative rainfall was 165 mm with a daily maximum of 40 mm in mid-July. The soundings for this monitoring have a square 8-loop of 40m square. The number of consecutive days without rain was 8 days between the fourth and fifth acquisition (from 15 July to 23 July). Soundings were made at different times after the rains (see table 1).

souding number	date	day number	Days since last rain	Cumulated Rainfall (mm) since Beginning of the Experiment	Cumulated Rainfall (mm) since Last Sounding Was Performed
1	23-juin	1	3	0	0
2	24-juin	2	0	19	19
3	25-juin	3	1	19	0
4	28-juin	6	4	21	2
5	23-juil	31	8	152	131
6	30-juil	38	3	166	14

Table 1. Distribution of surveys for monitoring and associated rainfall (mm).

RESULTS

The soundings from this monitoring are associated with exceptionally low noise levels (< 2.6 nV after stacking), allowing the demonstration of exponential decays of the MRS signal associated with very low initial amplitudes (down to 5 nV). Such a low signal level has never been observed or published to our knowledge.

Table 2 shows the first data from surveys of monitoring.

souding number	date	Average Stacks Number	Average Signal-to-Noise (S/N) Ratio	Mean T2* (ms)	average signal noise (nV)	maximum amplitude on the survey (nV)
1	23-juin	283	2.50	392.31	1.01	6.39
2	24-juin	362	1.53	536.29	1.82	8.13
3	25-juin	297	1.73	302.25	1.45	6.13
4	28-juin	294	2.63	379.50	0.98	5.40
5	23-juil	297	1.24	475.56	2.61	8.29
6	30-juil	249	2.98	221.00	0.83	6.00

Table 2. Surveys details and non-inverted signal parameters.

During this monitoring, the average maximum amplitude of the soundings is 6.7 nV. The average signal noise is 1.45 nV. On average the signal to noise ratio is 2.1. The average T2* is 384.5 ms over the monitoring, although there are disparities between surveys (between 221 and 536 ms).

Non inverted soundings results are shown in Figure 3 below.

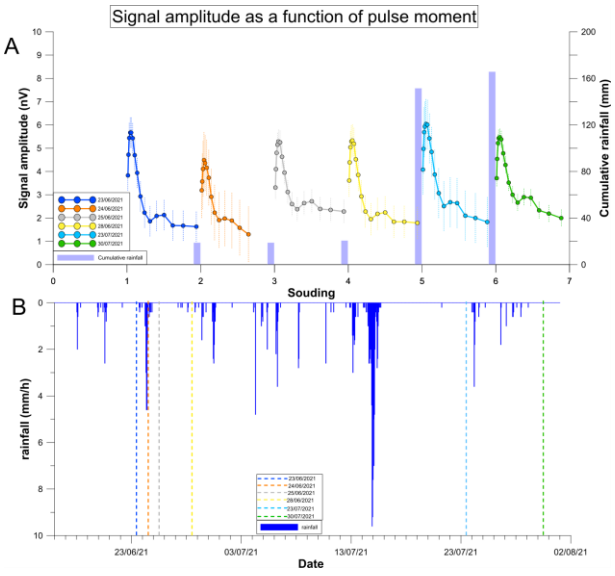

Figure 3. a) Signal amplitude (nV) as a function of pulse moment (A.ms) for each sounding and cumulative rainfall (mm) since the start of monitoring; b) Daily rainfall time series (mm/h) with reporting of sounding dates.

Figure 3 that MRS signal amplitude is relatively stable during this monitoring. Whether it rains or not, for a long time or not, the signal amplitudes do not overtake 8.3 nV. This shows that the Barrois limestone is probably very transmissive in this area.

Other studies have been conducted in fractured and karstified limestone contexts. In (Mazzilli, Chalikakis, et Carrière 2020) much higher initial amplitudes are present (between 105 and 160 nV) in unsatured zone. In (Chalikakis 2007), amplitudes of 10 to 80 nV were obtained by searching for a karst conduit. The context of extremely low electro-magnetic noise allows these measurements to be of good quality and with initial amplitudes between 5.40 nV and 8.29 nV.

The particular context of these MRS measurements highlights the absence of water storage in the limestone matrix of this zone. This lack of storage even in the micro-fractured matrix of limestones is not found in studies such as (Cholet 2017) in a nearby geological and hydrological context. These advances will provide a better understanding of the hydrodynamic functioning of this Barrois limestone system.

CONCLUSIONS

These results show that under favourable conditions, MRS can characterise such water quantities as low as 6.72 nV. They also indicate that the water content stored in these carbonates are very low despite an MRS time-lapse survey carried out during periods of intense rainfall. The limestone drainage is therefore very efficient. The inversion of these results to quantify water content will be the first perspective following this work. The data from this first monitoring will have to be completed by a winter campaign in order to see the possible changes due to the different hydrological context.

ACKNOWLEDGMENTS

I would like to thank Lise-Marie GIROD (trainee at Andra) for accompanying me in the field in all weathers.

REFERENCES

ANDRA. 2011. « La formation du Barrois ». Rapport interne D.RP.ASMG.11.0044.

Chalikakis, Konstantinos. 2007. Application de méthodes géophysiques pour la reconnaissance et la protection de ressources en eau dans les milieux karstiques . Thèse de doctorat université Paris 6. 224pp.

Cholet, Cybèle. 2017. Fonctionnement hydrogéologique et processus de transport dans les aquifères karstiques du Massif du Jura. Thèse de doctorat université de Franche-Comté. 214pp.

Mazzilli, Naomi, Konstantinos Chalikakis, et Simon D Carrière. 2020. Surface Nuclear Magnetic Resonance Monitoring Reveals Karst Unsaturated Zone Recharge Dynamics during a Rain Event. Water 2020, 12, 3183. 10pp.

3-D SNMR monitoring of the Tête-Rousse glacier - 2012-2018

[1]J-M. Baltassat, [2]A. Legchenko, [3]J-F. Girard, [4]S. Garambois, [2]O. Gagliardini, [2]C. Vincent and [5]E. Thibert

[1] BRGM
Orléans, France
jm.baltassat@brgm.fr

[2] IGE
Grenoble, France
a.legtchenko@ird.fr
christian.vincent@univ-grenoble-alpes.fr
olivier.gagliardini@univ-grenoble-alpes.fr

[3] ITES
Strasbourg, France
jf.Girard@unistra.fr

[4] ISTerre
Grenoble, France
stephane.garambois@ujf-grenoble.fr

[5] IRSTEA
Saint-Martin d'Hères, France
emmanuel.thibert@inrae.fr

SUMMARY

The small Tête-Rousse glacier is located in the Mont Blanc massif (French Alps) and contains an inner water filled cavity.
We demonstrated the efficiency of the 3-D SNMR for monitoring the water volume variations and proved the cost-effectiveness of the 3-D SNMR mapping compared to drilling and pumping usually used for investigating water accumulation in glaciers. 3-D SNMR monitoring was then undertaken between 2010 and 2018 in order to follow the evolution of the intra-glacial water volumes.
3-D SNMR was extended to the whole glacier and made it possible to detect and accurately locate a new water volume in 2012 in the upper part of the glacier. The monitoring shows a rapid evolution of its water storage : from 2014 to 2018, the water volume has increased by 40 % which is worth to take into account for the hazard assessment.

Key words: SNMR, Glacier, GPR, water, cavity.

INTRODUCTION

The small Tête Rousse glacier (150 x 500 m) is located in the Mont Blanc area (French Alps) at an altitude of 3100 to 3300 m (Figure 1).

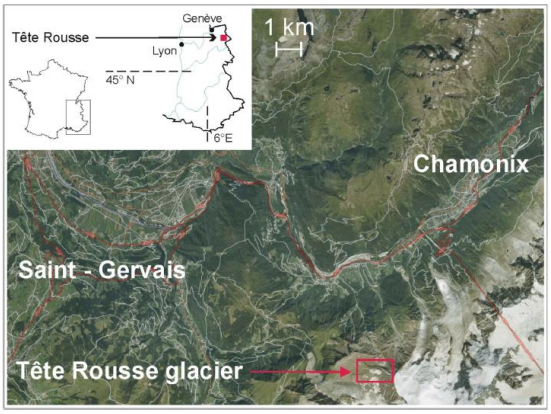

Figure 1. Location of the Tête-Rousse glacier.

In 1892, an outburst flood from this glacier released about 200,000m3 of water mixed with ice, causing much damage. Water circulation in a glacier is an important factor that determines ice dynamics, runoff characteristics, and water quality. The recent, growing, concern over the response of glaciers to future-climate scenarios necessitates understanding of the hydrological processes in ice. A temperate accumulation area and a predominantly cold ablation area characterize the thermal regime of the Tête-Rousse glacier and increase, together with its topology, the potential for water storage within the its drainage system. In 2007, the uncertainty relative to the glacier conditions initiated a GPR survey followed by 3-D-SNMR investigations carried out in 2009. The results show a large water-filled cavern containing about 55,000m3 of water (Vincent et al., 2012). The drilling program of more than 20 boreholes confirmed the existence of a water-filled cavity and defined its location. Boreholes intersecting water-filled cave and further sonar measurement of the cave geometry validated the SNMR cavern location in agreement with GPR (Ground Penetrating Radar) reflexions (Garambois et al. 2016). The cavern was then drained and water pumping validated the water volume estimated by SNMR (Legtchenko et al. 2011).

METHODS

The 3-D field setup is composed of overlapped measuring loops covering the area investigated with SNMR. Under the constraints of high altitude, snowfield conditions and the threat of rock fall, the coincident Tx-Rx loop configuration of measurement was chosen because of its more rapid setup and its lower acquisition duration. All individual soundings are incorporated into one data set for the 3-D inversion. NUMIS^{PLUS} equipment manufactured by IRIS Instruments (France) was used for data acquisition.

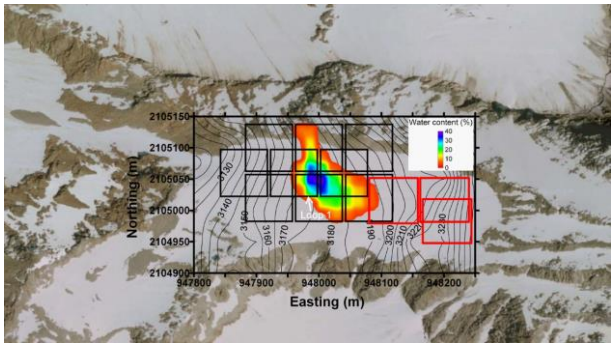

Figure 2. Tête-Rousse cavern location in the central part of the glacier (2009). Squares show position of SNMR loops.

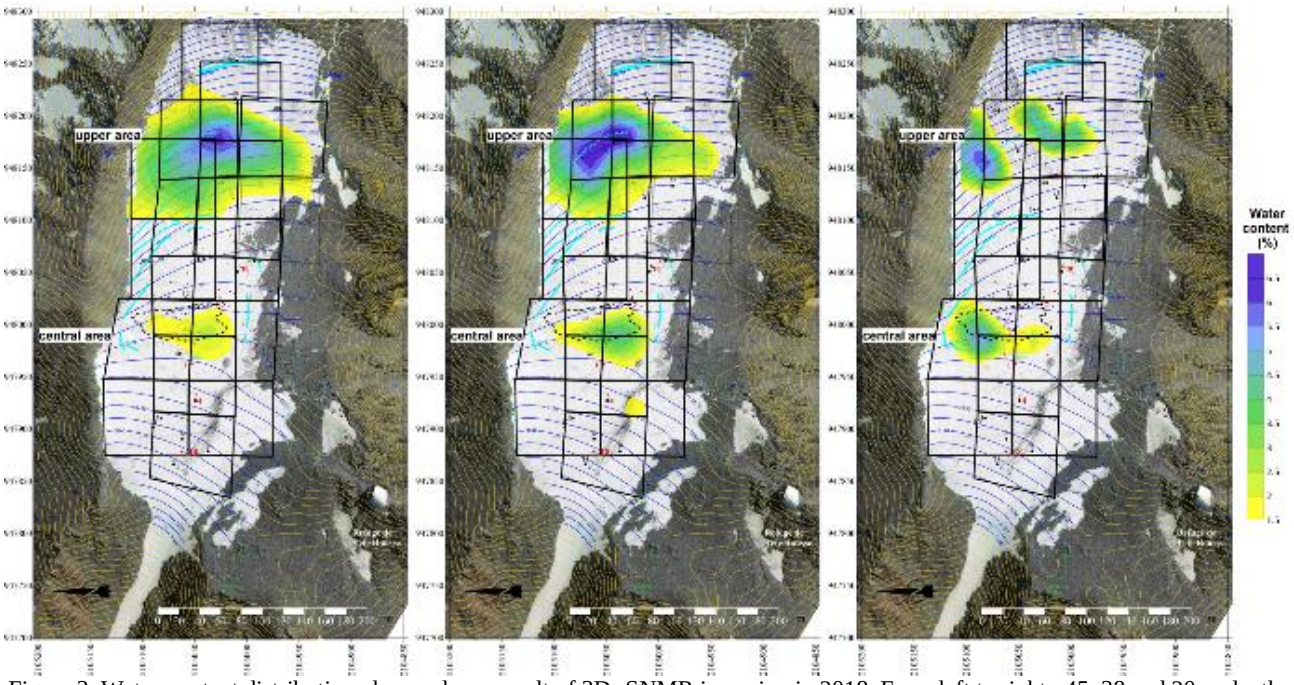

Figure 3. Water-content distribution observed as a result of 3D- SNMR inversion in 2018. From left to right : 45, 38 and 20 m depth. Squares show position of SNMR loops.

Nine loops were used between 2009 and 2011 (Fig. 2; black squares) and three additional loops were added for surveys carried out in 2012 (red squares) after a second water volume was incidentally observed at the glacier up part when testing a remote loop for noise mitigation. As this new water volume was coherent with the general functioning of the water recharge including a winter recharge from a upper reservoir, for the next surveys (2013, 2014, 2015 and 2018), 15 to 16 loops were used in order to investigate the entire glacier area including the upmost area (figure 3).

Data processing and 3-D inversion were done with the SAMOVAR software package developed at the Institut de Recherche pour le Développement (Legchenko et al., 2011, IRD, France). Inversion was conducted according to Tikhonov's regularization method (Tikhonov and Arsenin, 1977) and the conjugate gradient method (Stoer and Bulirsch, 1980) for optimization.

Modelling works by Legchenko and al. 2014, show that small targets cannot be resolved with 3-D-SNMR inversion and consequently small water volumes cannot be accurately measured with one SNMR loop. But with the applied 3-D field setup consisting of several overlapping loops, areas with a different sensitivity for different loops overlap and the overall sensitivity within the 3-D setup is much more homogeneous. Thus SNMR water volumes become significant. An expert approach was developed (Legtchenko and al. 2014) based first on smooth inversion for locating and a preliminary estimation of the water volumes. It comprises then a forward modelling of 100% water volumes located from inversion results and finally an estimation of the maximum and minimum water volumes based on water volume located at high and low sensitivity areas. This approach produced good results when applied to investigations of the Tête Rousse glacier and was validated by the pumping results (Figure 4). It was used for all the presented results hereafter.

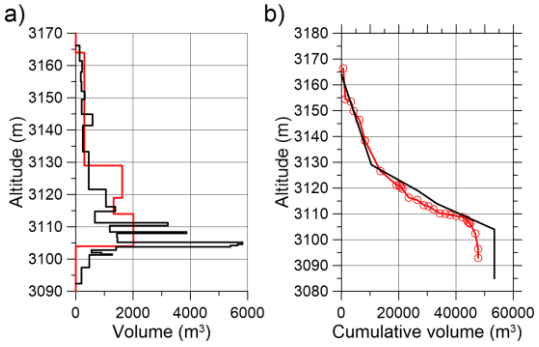

Figure 4. SNMR monitoring of the cavern drainage. a) the volume estimated with 3-D SNMR versus altitude (red line) and the volume pumped from the cavern (black line); b) the corresponding cumulative volumes. The red circles show 3-D SNMR estimates.

RESULTS

From 2012 to 2018 SNMR monitoring was continued over the whole glacier (including the upper part where a new water volume was discovered in 2012). SNMR results obtained in june 2018 are the followings :

The upper cavity size increases; it becomes wider and deeper. We interpret this cavern as an increasing water filled crevasse in the ice body. :

- The water volumes in the lower part of the glacier are estimated between 5100 and 9100 m3,
- The water volumes in the upper area are estimated between 23300 et 31200 m 3 .
- The total volume for the entire glacier is then between 28425 m^3 et 40330 m^3 while it was 40% lower in 2015.

The minimum volume estimate is considered as robust since amongst the different studied model, taking into account the glacier boundary, none of a lower volume explains the observed data. The maximum volume, on the contrary, remains poorly determined because of the resolution loss with increased depth.

SNMR water volume estimates show the following evolution from 2012 to 2018 : i) for the central cavity, a stabilization in the method sensitivity limits, at the beginning of the period and then a decrease of less than 20% from 2014 to 2018 of while ii) the upper cavity show a significant increase (+40%°) from 2015 to 2018 (Figure 5).

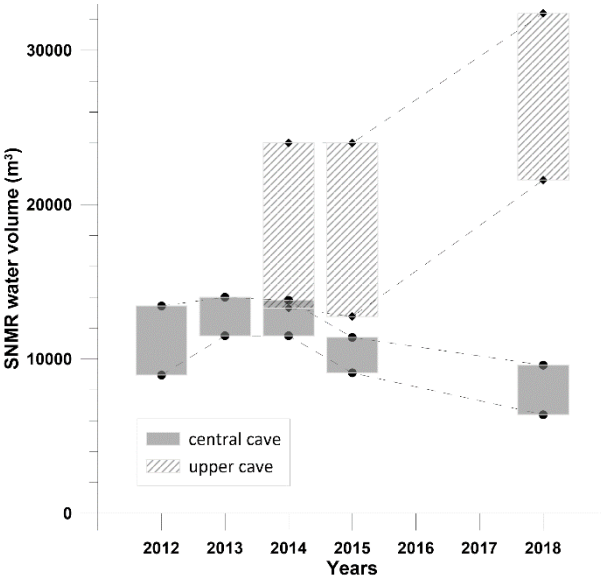

Figure 5 : Evolution of minimum and maximum water volumes estimated from SNMR in the central and upper part of the glacier.

Water content distribution in the upper part of the glacier show a remarkable coherence with GPR reflexions in agreement with the location of visible crevasse at the surface and the glacier depth as defined from boreholes results (figure 6). This coherence is geometrical (location, depth and inclination) and for physical principles: higher SNMR water contents correspond to well-marked GPR reflexions which are the expected responses of high dielectric contrast interfaces between ice and water.

The three independent data set (GPR, SNMR, drilling) agree to globally envisage a water volume developped around a crevasse set between 30 and 60 m depth, deepening and crossing the whole glacier along a bit less than 100 m distance from north to south.

Different interpretations are proposed in order to explain the observed geophysical responses: i) bulk water filling subvertical open crevasse; ii) water filling insterstitial pores within ice grains of the whole glacier thickness ; iii) 100 % bulk water volume at the glacier base.

Uncertainty of GPR results concerning the glacier depth authorizes the hypothesis of an intercalated water bearing sediment layer at the basement top. Further SNMR modelling and new geophysical investigations are recommended in order to test this hypothesis. The geophysical results yet obtained nevertheless confirm the hypothesis previously proposed by glaciologists of an open and water filled at depth crevasse system in this temperate ice region of the glacier.

CONCLUSIONS

Our results show that 3-D-SNMR method is a reliable and effective tool for investigating water in a glacier. Unambiguous identification of liquid water in ice, localization of water-storage areas, and the possibility of estimating the water volume stored in a glacier are three advantages of 3-D-SNMR compared to traditional geophysical methods.

Between 2010 and 2012, 3-D SNMR monitoring makes it possible comparing the water volume estimates with the volumes extracted by pumping, which shows a good correlation in-between.

Further 3-D SNMR monitoring of the intra-glacier water volume shows a rapid evolution. A new water reservoir was discovered in 2012 in the upper part of the glacier. The monitoring of this new reservoir shows a 40% increase of the water volume observed from 2014 to 2018 that is worth taking into account for the hazard assessment.

ACKNOWLEDGMENTS

We thank the Mairie de St-Gervais-les-Bains (Haute-Savoie), the RTM Haute-Savoie (Restauration des Terrain en Montagne) and the Direction Generale de Prevention des Risques, DGPR (part of Ministère de la Transition Ecologique et Solidaire, MTES) for having founded this works.

REFERENCES

Garambois S., A. Legchenko, C. Vincent & E. Thibert, 2016, Ground Penetrating Radar and Surface Nuclear Magnetic resonance monitoring of an englacial water-filled cavity in the polythermal glacier of Tête Rousse, Geophysics, Vol. 81, N° 1, WA131-WA146.

Legchenko, A., Descloitres, M., Vincent, C., Guyard, H., Garambois, S., Chalikakis, K., and Ezerski, M. (2011). Three-dimensional magnetic resonance imaging for groundwater, New J. Phys., 13, 025022, doi:10.1088/1367-2630/13/2/025022.

Legchenko A and 10 others (2014.) Monitoring water accumulation in a glacier using magnetic resonance imaging. Cryosphere, 8, 155–166 (doi: 10.5194/tc-8-155-2014).

Vincent, C., Descloitres, M., Garambois, S., Legchenko, A., Guyard, H., Lefebvre, E., and Gilbert, A. (2012a). Detection of a subglacial lake in Glacier de Tete Rousse (Mont Blanc area, France), J. Glaciol., 58, 866–878, doi:10.3189/2012JoG11J179.

Vincent, C., Descloitres, M., Garambois, S., Legchenko, A., Guyard, H., Thibert, E., Gilbert, A., Karr, N., and Tairraz, V. (2012b). Détection d'une poche d'eau au glacier de Tête Rousse en 2010 et mesures préventives pour éviter une catastrophe, La Houille Blanche, 2, 34–41, doi:10.1051/lhb/2012013.

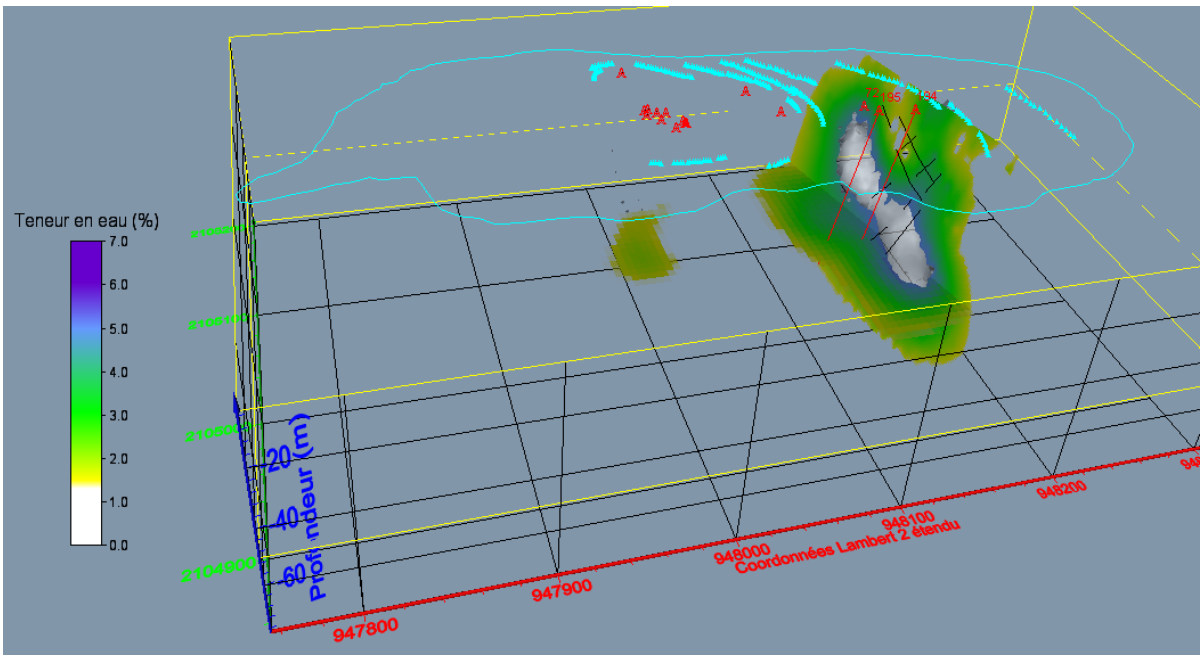

Figure 6 : Illustration of water content extracted from the 3D model resulting of 2018 SNMR investigation of Tete-Rousse glacier through a depth horizontal slice at -50m and an oblique slice corresponding approximatively with GPR reflexions (black segments). The grey surface envelops SNMR water content higher than 4%. Glacier boundary and crevasse location at the topographical surface are drawn as light blue lines and boreholes location are in red.

First field experiences using surface nuclear magnetic resonance with prepolarization (SNMR-PP)

[1]Stephan Costabel **[2,4]Thomas Hiller** **[3]Raphael Dlugosch** **[4]Mike Müller-Petke**

[1] BGR
Berlin, Germany
stephan.costabel@bgr.de

[2] BGR
Berlin, Germany
thomas.hiller@bgr.de

[3] BGR
Hanover, Germany
raphael.dlugosch@bgr.de

[4] LIAG
Hanover, Germany
mike.mueller-petke@leibniz-liag.de

SUMMARY

Surface nuclear magnetic resonance (SNMR) using prepolarization (PP) is expected to enable soil moisture measurements on the small scale, i.e., using measurement coils with diameters smaller than 2 m. We conducted field experiments to validate this expectation. In two soil physical irrigation scenarios, a sprinkling and a ponding experiment, we demonstrate that SNMR-PP provides reliable signals and allows to monitor the water infiltration process. However, due to the effective dead time of the SNMR-PP prototype (11 ms), a certain proportion of the pore water in the partially saturated soil is undetectable. This limits the quantification of soil moisture to date. We are confident that technical improvements can overcome this limitation in the future.

Key words: Prepolarization, Soil water content.

INTRODUCTION

In contrast to the classical application of SNMR for groundwater exploration using surface cable loops with diameters of at least 20 m, the feasibility of the method for vadose zone investigations with smaller loop areas of just a few m^2 is strongly limited. This is mainly due to the weak signals naturally associated with the corresponding small measurement volumes below these coils. To date, soil moisture measurements at depths below one meter are not possible at all or are at least too time-consuming and thus impractical due to very long averaging times (Costabel, 2019).

Thus, the technique of prepolarization (PP) to enhance the SNMR signal on the footprint of a small transmitter-receiver coil configuration has come into the focus of recent research. Using PP, the spin magnetization vector is directly amplified by a static magnetic field, which is generated by an additional coil for a few seconds before the usual excitation pulse is transmitted. The first published studies within this young research field deal with the theoretical implications on the forward modelling (de Pasquale and Mohnke, 2014; Hiller et al., 2020) or test the feasibility of SNMR using PP over pure water reservoirs (Lin et al., 2018; Costabel et al., 2019). This abstract reports our first field experiences using SNMR-PP on real soil and considers, from the soil physical point of view, realistic experimental irrigation scenarios.

METHODS

Sprinkling test

We conducted an irrigation experiment using a conventional sprinkler on the Schillerslage test site North of Hanover - the simulation of a heavy rainfall experiment with a duration of, in total, one hour and an irrigation rate of 0.5 mm/min. We took SNMR-PP measurements using a coincident coil setup as depicted in Fig.1a and b at the beginning and at the end of the sprinkling period. Seven TDR probes were placed within the irrigation area of about 5x5 m^2 for accompanying soil moisture measurements at depths between 0.03 and 0.23 m. The corresponding reference data (Fig.1c) indicate a high level of heterogeneity of the infiltration process with water contents ranging from 2 to 6 vol% before and 16 to 26 vol% after irrigation.

Ponding test

We conducted a ponding test on the Horstwalde test site south of Berlin using a circular tub with a diameter of 1.4 m (Fig. 2a), the bottom of which was removed to allow infiltration into the natural soil. We arranged the same PP coil as in the sprinkling experiment on the outside of the pond vessel, while the Tx/Rx coils (1 turn/20 turns), realized as figure-of-eight (Fig8), were placed on the inside. The measurement coils were lifted a few cm to allow a water table of 2 cm above the surface. We realized steady state inflow conditions into the pond that, by being in balance with the infiltration rate, kept the water table constant. Eight TDR probes (Fig. 2b) monitored the infiltration process inside the pond at a depth range from 0.11 to 0.34 m. As depicted in Fig. 2c, the corresponding TDR water contents lie between 10 and 15 vol% before the experiment and increase to values ranging from 20 to 33 vol% after 140 min of inflow.

Data acquisition and processing

The SNMR-PP measurements for both irrigation experiments were conducted using 4 on-resonant pulse moments ranging from 0.01 to 0.1 As and a length of about 2 ms (4 periods at a Larmor frequency of about 2110 Hz). The effective PP current of 1150 A was switched off after 2 seconds. The ramp-down within 1 ms exhibits the shape of a half cosine function (Hiller et al., 2020; 2021). Two SNMR-PP measurements were conducted before and after the sprinkling experiment, each with 64 repetitions, resulting in a total time of about 40 min for one complete run of the 4 subsequent pulse moments. Because we expected a higher infiltration velocity during the ponding compared to sprinkling, we shortened the measurement time to 15 min by conducting only 16 measurement repetitions for each pulse moment.

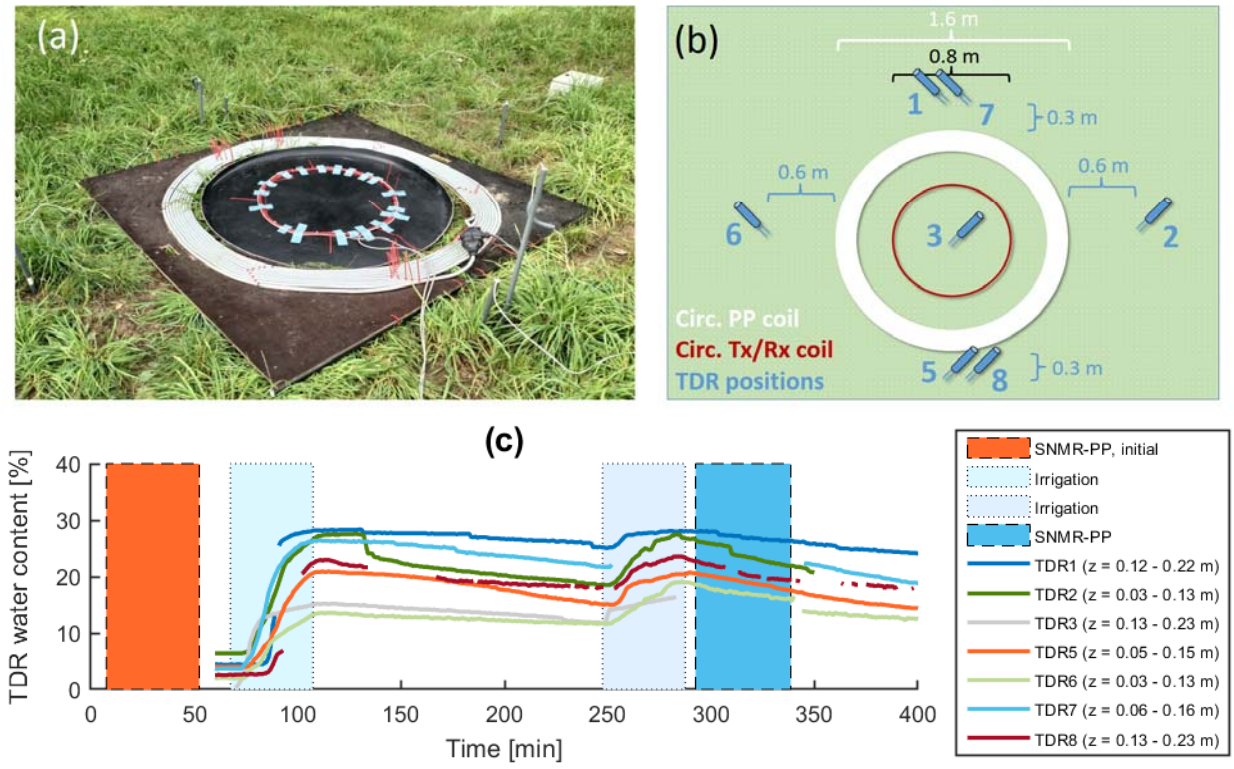

Figure 1: (a) Photograph and (b) sketch of the experimental setup for the sprinkling experiment and (c) corresponding TDR monitoring data.

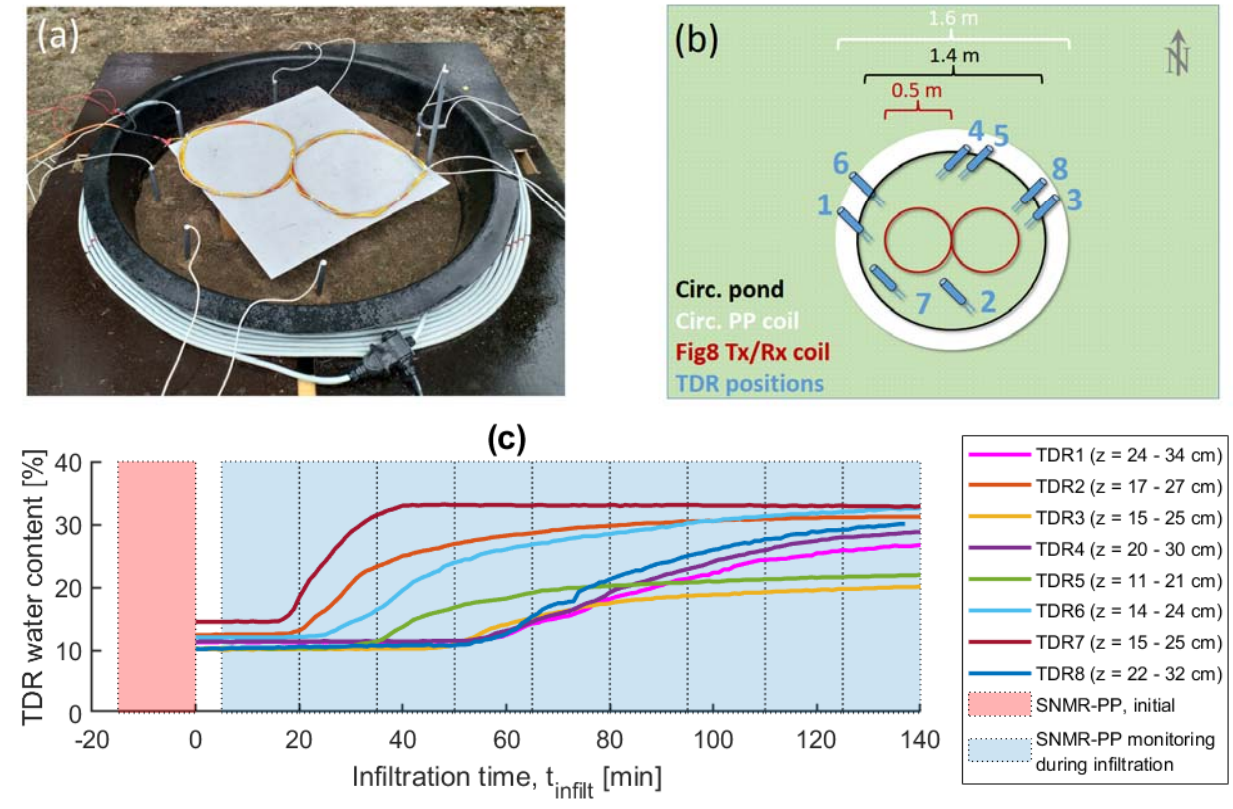

Figure 2: (a) Photograph and (b) sketch of the experimental setup for the ponding experiment and (c) corresponding TDR monitoring data.

The data processing was similar to the standard SNMR processing, which includes despiking, reference noise cancellation, band pass filtering (200 Hz), digital quadrature detection, and stacking. We used a three-channel multi-component antenna as noise reference as suggested by Costabel (2019) for areas dominated by nearby anthropogenic noise sources. Unfortunately, the noise level in Horstwalde heavily increased during the experiment for an unknown reason and we decided to stop the monitoring after 140 min. For the experiment times > 40 min, we had to stack the data for different subsequent measurements to be able to fit the resulting time series.

Water content calibration

We tested the two coil configurations described above and the corresponding pulse sequences on a water reservoir (halfspace with 100 vol% water) with varying distance to the water table. These data sets serve, on the one hand, as referencing benchmarks for the forward modelling approaches developed by Hiller et al. (2021). One the other hand, these data sets provide the opportunity to calibrate the infiltration data, similar to the standard process in the laboratory. Consequently, we normalize our measured SNMR-PP signal amplitudes over soil directly to values of volumetric water content.

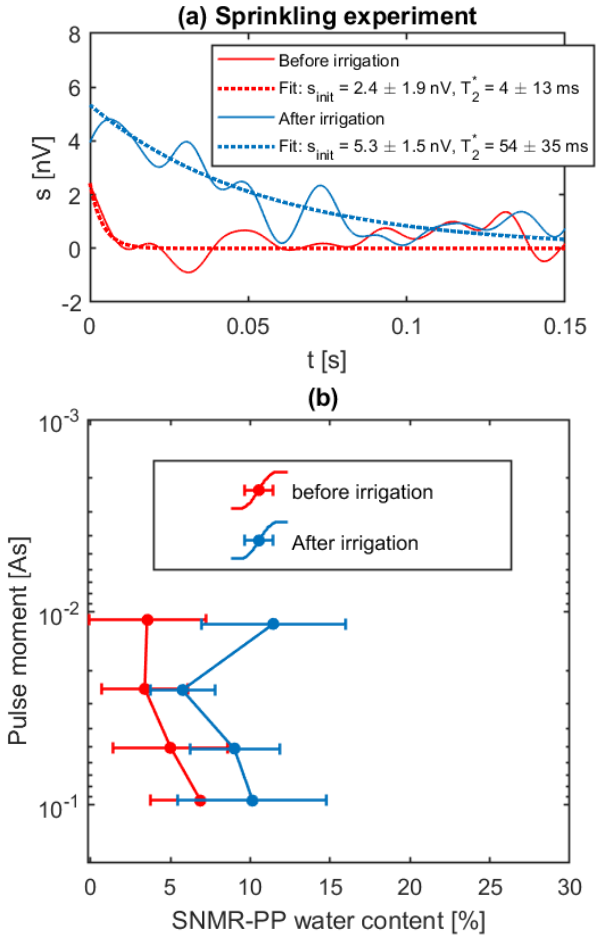

Figure 3: (a) SNMR-PP data examples of the sprinkling experiment after postprocessing and stacking (at q = 0.05 As), (b) initial signal amplitudes before after the irrigation period normalized to values of volumetric water content.

However, the results of this procedure must be considered to be only rough estimates of the mean water content inside the sensitive volume of the SNMR-PP measurement. Their effective accuracy depends on many details of the experimental setup (distance of coils to the ground/water table, direction of Fig8, inclination and strength of the Earth's magnetic field, etc.). Future interpretation will include the correct forward modelling for the given conditions including the exact spin dynamics (for details see Hiller et al., 2021).

RESULTS

Sprinkling test

Figure 3a shows the SNMR-PP data before and after irrigation at a pulse moment q of 0.05 As. The corresponding focus depth of investigation lies between 20 and 35 cm. Obviously, a clear NMR signal is captured after infiltration, whereas the initial signal of the dry soil is much weaker. Actually, under the initial dry condition, the NMR signal is not even reliably detected when considering the uncertainty intervals of the mono-exponential fitting parameters s_{init} (initial amplitude) and T_2^* (relaxation time).

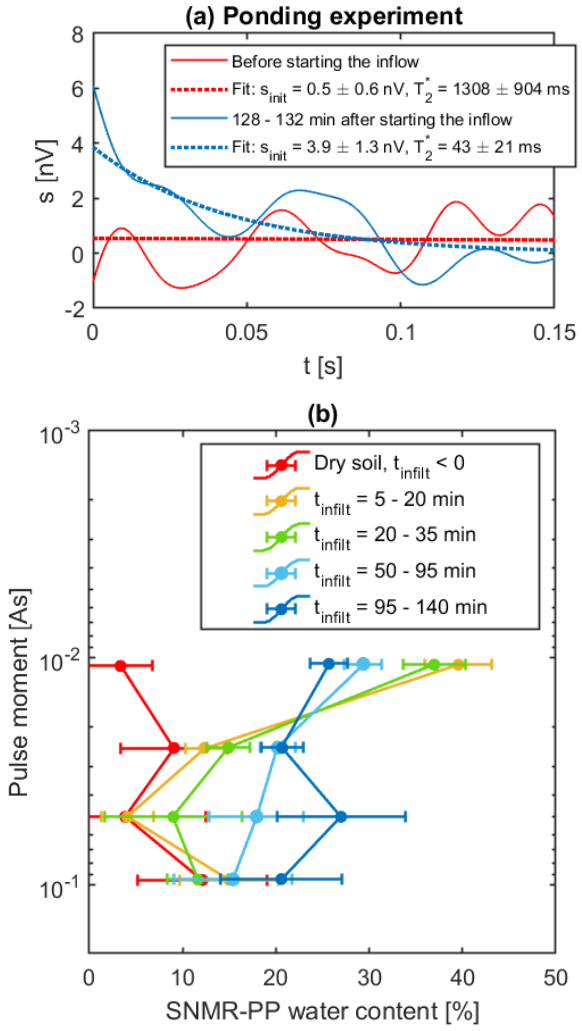

Figure 4: (a) SNMR-PP data examples of the ponding experiment after postprocessing and stacking (at q = 0.05 As), (b) initial signal amplitudes before and during the infiltration normalized to values of volumetric water content.

Figure 3b shows the initial amplitudes of the other pulse moments normalized to values of water content. We observe a general increase from about 5 to 10 Vol%, i.e., the SNMR-PP measurements clearly underestimate the real water content compared to the TDR references (16 to 26 Vol%).

The sprinkling experiment was complemented by laboratory NMR experiments using sample material and a forward modelling study, reported by Hiller et al. (2021), which provide evidence for the fact that only a fraction of ~0.4 of the real water content after infiltration is measured by SNMR-PP. This is because a certain portion of the pore water with short T_2^* remains invisible due to the effective dead time of 11 ms.

Ponding test

Figure 4a depicts two SNMR-PP data examples (at q = 0.05 As) before and at the end of the ponding experiment. For the Fig8 coil setup used in this experiment and considering the fact that the coils were lifted above the pond, we observe the change of the NMR signal at a focus depth of only 10 to 20 cm. No signal was detectable for the dry soil. However, after starting the inflow into the pond and with it the infiltration of water into the soil, NMR signals are detected and could reliably be quantified with uncertainty intervals of 5 to 10 Vol%.

In Fig.4b, we observe the changes of the initial amplitudes with infiltration time. As in Fig.3, the signal amplitudes are normalized to values of water content. The signals at q = 0.01 As are most likely overestimated, because the free water on top of the surface inside the pond vessel is also captured in addition to the pore water infiltrating into the soil. For q > 0.01 As, the results are reliable and are in accordance to the reference water content range of 20 to 32 Vol% as measured by the TDR probes. However, also for this experiment, we expect that a certain portion of the pore water is not detected within the 11 ms dead time of the SNMR-PP measurement. We hypothesize that the apparent agreement of SNMR-PP results and TDR reference is also due to the free water on top of the pond that adds a signal also to the data for q > 0.01 As.

CONCLUSIONS

Our results demonstrate that SNMR-PP measurements on real soil are possible and can provide information on the infiltration dynamics in corresponding soil physical experiments. However, a reliable quantification of the water content is difficult due to effective dead time that is too high to capture all water fractions in partially saturated soil. This is in particular true for fine-grain soils.

Further technical improvements could overcome this serious limitation and could make water proportions visible that are currently undetectable with the SNMR-PP prototype available: The timing between PP and Tx pulse can be improved to decrease the effective dead time. Higher PP currents, i.e., generated by superconductive coils, will increase the signal amplification.

The benefits of applying the SNMR-PP method for soil physical investigations compared to existing methods are obvious: Spatially integrated water content information is provided in contrast to conventional soil physical point information and the option of direct water content measurements, once available, is an excellent complement to indirect geophysical methods for soil moisture investigations.

ACKNOWLEDGMENTS

For the experiments in this study, we used the MRS-Midi Equipment in combination with a specific PP module of Radic Research based on a copper cable. We thank the German Federal Institute for Materials Research and Testing for providing us with the necessary logistics to conduct our field experiments.

REFERENCES

Costabel, S. (2019). Noise analysis and cancellation for the underground application of magnetic resonance using a multi-component reference antenna – Case study from the rock laboratory of Mont Terri, Switzerland. Journal of Applied Geophysics, 169, 85.

Costabel, S., Hiller, T., Radic, T., Dlugosch, R., & Müller-Petke, M. (2019). Surface Nuclear Magnetic Resonance Measurements in Berlin - Proof-Of-Concept for Applying the Prepolarisation Technique in Urban Areas. In Conference proceedings, 25th european meeting of environmental and engineering geophysics (Vol. 2019, pp. 1).

de Pasquale, G., & Mohnke, O. (2014). Numerical Study of Prepolarized Surface Nuclear Magnetic Resonance in the Vadose Zone. Vadose Zone Journal, 13 (11), 1.

Hiller, T., Dlugosch, R., & Müller-Petke, M. (2020). Utilizing pre-polarization to enhance SNMR signals - effect of imperfect switch-off. Geophysical Journal International, 222 (2), 815-826.

Hiller, T., Costabel, S., Radic, T., Dlugosch, R., & Müller-Petke, M. (2021). Feasibility study on prepolarized surface nuclear magnetic resonance for soil moisture measurements. Vadose Zone Journal, e20138.

Lin, T., Yang, Y., Teng, F., & Müller-Petke, M. (2018). Enabling surface nuclear magnetic resonance at high-noise environments using a pre-polarization pulse. Geophysical Journal International, 212 (2), 1463.

Thermal Model of the Apsu Transmitter for Lightweight and Compact Heat Sink Design

[1]Nikhil B Gaikwad, [2]Lichao Liu, [3]Matthew Griffiths, [4]Mathias Vang, [5]Denys Grombacher, [6]Jakob Juul Larsen

[1, 3, 6] Department of Electrical and Computer Engineering
Aarhus University, 8000 Aarhus C, Denmark
Email : [1]nbg@ece.au.dk, [3]mpg@ece.au.dk, [6]jjl@ece.au.dk

[2,4,5] Hydrogeophysics Group, Department of Geoscience,Aarhus University, Denmark
[2]lichao@geo.au.dk, [4]mva@geo.au.dk, [5]denys.grombacher@geo.au.dk

SUMMARY

The compact and flexible Apsu instrument has been developed to deliver 105 A and up to 150 kW of instantaneous power during the transmission. The Apsu transmitter unit (ApsuTx) control and regulate this high current where some amount of transmission power is dissipated as thermal energy. Therefore, thermal management of this unused power becomes an impotent concern for reliable operation of the ApsuTx, especially for new steady-state sequences. We briefly introduce the ApsuTx circuit and provide a mathematical formulation for electrical power dissipation. This formulation is used to design the thermal model of ApsuTx and it is evaluated using different input sequences. The comparison results showed that 33.93 W is dissipated by steady-state sequences, which is approximately ten times more than with conventional pulses. This power can only be dissipated safely by a heatsink with a maximum thermal resistance of 1.832 ^{o}C/W. A small size heat sink (300 mm × 200 mm × 8 mm) has been designed and installed with a lower thermal resistance than the calculated value. This provides a compact and lightweight solution for remote field measurements.

Key words: Apsu instrument, thermal management, heatsink, electrical systems.

INTRODUCTION

Surface nuclear magnetic resonance (NMR) has emerged as an effective groundwater investigation method in recent years. The compact and flexible Apsu has been developed at Aarhus University, Denmark to investigate groundwater down to 30 meters depth using a transmitter with an effective peak current of 105 A (Larsen et al., 2020). Because of such high currents, the Apsu transmitter unit (ApsuTx) can draw up to 150 kW of instantaneous power during the transmission. The majority of this power is dissipated as heat in the ApsuTx and transmitter coil. The thermal management of this dissipated heat power is an essential system requirement for the reliable and safe working of the instrument (Lohrasbi et al., 2020).

The Apsu instrument draws power from a generator connected to an AC to DC converter, which in turn is connected to a 20-mF capacitor bank. The capacitor bank supplies variable voltage up to 600 V (Larsen et al., 2020). The ApsuTx converts this DC input supply into flexible AC sequences, i.e. NMR transmitter pulses using an IGBT based H-Bridge that is connected to a 50 m × 50 m coil. The H-Bridge, damping resistor (DR), and transmitter coil are the primary sources of heat dissipation in the Apsu instrument. The transmitter coil has a high advantage in heat dissipation because of only 1-ohm of resistance (R) and 200 meters of extended length. The H-Bridge and DR are the main concerns for thermal management because they are spaced closely within the ApsuTx box. In conventional systems (Lohrasbi et al., 2020), heat sinks are the proven solution for effective thermal management. However, the design of a compact and lightweight heat sink is critical to meet our field requirements (Keating et al., 2018). This work focuses on thermal modelling of the ApsuTx and evaluates the heartsink's thermal resistance. This thermal resistance is used to design a suitable heatsink with optimum dimensions and weight.

METHODS

ApsuTx has been designed to transmit bidirectionally varying magnetic fields at the Larmor frequency to excite the nuclear spin of hydrogen nuclei in underground water molecules (Liu et al., 2019). This magnetic field is generated using a high amplitude current flowing through the transmitter coil controlled and regulated by H-Bridge in ApsuTx. The Apsu instrument uses an untuned transmitter coil, where the H-Bridge generates bidirectional triangular waveforms at the Larmor frequency with variable amplitude. In this paper, we focus on the Apsu instrument operating with the steady-state pulses sequences with 10% of transmission time and 90% of NMR signal acquisition time (Grombacher et al., 2021).

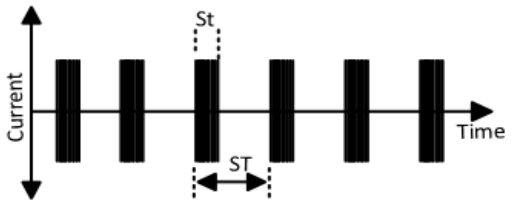

Figure 1. Schematic overview of a steady-state current sequence.

Figure 1 shows a schematic overview of a steady-state sequence where transmitter pulses (St milliseconds long) are interleaved with acquisition time (ST - St milliseconds long). This steady-state sequence contains bipolar triangular pulses switching at the Larmor frequency for a duration of St milliseconds in each sequence. Figure 2 shows a simplified circuit of the H-bridge where the supply voltage and IGBT gate inputs are controlled by the Apsu controller (ApsuTxC). The 220-ohm damping resistor also contributes to the heat dissipation and is included in the thermal model of the system. In the H-Bridge, the coil current changes according to the gate

pulse pattern, where rise time depends on the collective impedance of the coil and the DR.

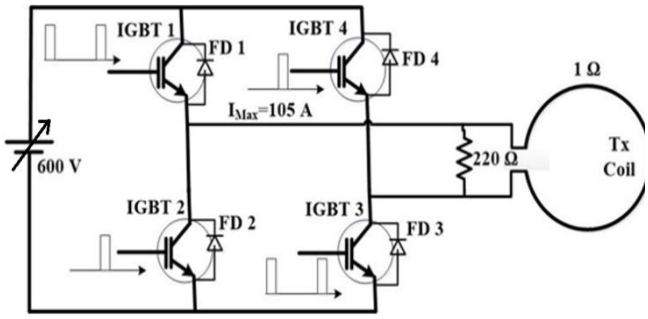

Figure 2: H-Bridge switching circuit with four IGBTs in the ApsuTx.

As shown in Figure 3, the positive rising current is delivered to the coil when IGBT 1 and IGBT 3 are ON. The negative rising current is given to the coil when IGBT 2 and IGBT 4 are ON. Once the current value reaches the peak, all IGBT's get switched OFF, then the current starts dropping at the same rate, mainly because of the inductance offered by the coil.

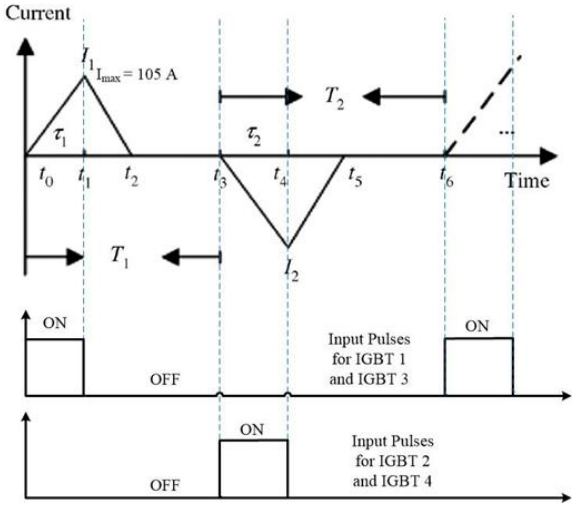

Figure 3: Timing diagram for the IGBT switching circuit.

The thermal modelling has been done by considering the following assumptions. The maximum ambient temperature is considered as 60 ^{o}C. Also, the Freewheeling Diodes (FWD) in the IGBTs are conducting during the switching operation. The peak coil current (Imax) is 105 A, the thermal resistance of the interface between the IGBT case and heatsink (Rth_interface) is assumed as 0.1 W/^{o}C, and the maximum IGBT Junction Temperature is 125 ^{o}C. An IGBT power loss (P_{IGBT}) is divided into turn ON and OFF switching loss and conduction loss. P_{IGBT} is calculated using

$$P_{IGBT} = P_{On} + P_{Off} + P_{\text{Conduction Loss}} \quad (1)$$

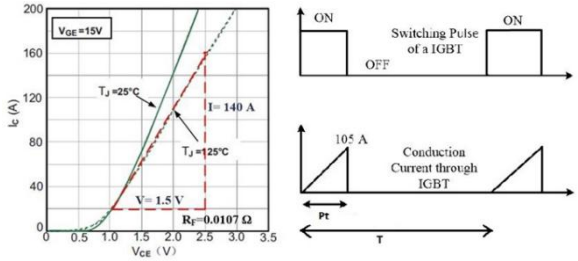

Figure 4: Forward characteristics of the IGBT and the forward current through the IGBT

Where Turn ON Energy (E_{on}) and OFF Energy (E_{off}) per Switching is 10 mJ with a test condition of T j = 125 C, VCC = 600V, IC = 105A and Inductive Load. So, power can be calculated by multiplying the total number of pulses per second, i.e. F_s, for extreme test conditions. Figure (4) shows forward characteristics of IGBT where the forwarded resistance (RF) is 0.0107 Ohm and an IGBT conduct for a duration of Pt seconds. The energy loss because of conduction per pulse is calculated using

$$\text{E Conduction Loss} = R_F \times I_c^2 \times Pt \times 0.5 \quad (2)$$

Where 0.5 signifies the area undercover for the triangular pulse is half compared with a square pulse. Finally, P_{IGBT} and F_s are calculated with

$$P_{IGBT} = (E_{on} + E_{off} + R_F \times I_c^2 \times Pt \times 0.5) \times F_s \quad (3)$$

$$F_s = F_L \times (St/ST) \quad (4)$$

Other than IGBT power loss, Freewheeling Diodes (P_{FWD}) and Damping Resistance (P_{DR}) also contribute to the total power dissipation in the ApsuTx. P_{FWD} and P_{DR} are calculated from

$$P_{FWD} = E_{on} \times F_s \quad (5)$$

$$P_{DR} = (105A / 221\ \Omega)^2 \times 220\ \Omega \times 4Pt \times F_s = 198.64 \times Pt \times F_s \quad (6)$$

All the above parameters are used in the thermal model of ApsuTx, which is shown in Figure 5. The thermal resistance of the IGBT and Freewheeling Diode is used from the IGBT datasheet. This thermal model has been used to analyze the heat dissipation of ApsuTx and also it is used to decide the thermal resistance and dimensions of the heat-sink.

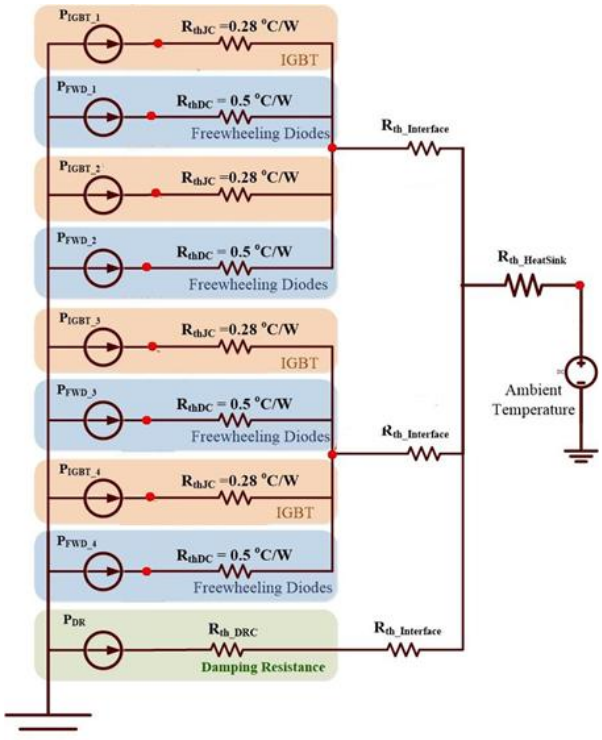

Figure 5: Thermal model of ApsuTx including H bridge and Damping resistance.

RESULTS

As shown in Figure 2, this thermal model is used to decide the final dimensions of the ApsuTx heat sink. This model has been evaluated for a steady-state sequence and a

conventional pulses. Here, the thermal resistance of DR ($R_{th\ DRC}$) is 1.2 ^{o}C/W and the thermal resistance of the interface ($R_{th\_Interface)}$ is assumed to be 0.1 ^{o}C/W. P_{IGBT}, P_{FWD} and P_{DR} are calculated for both cases. As seen in Table 1, a total of 33.93-W is dissipated by the steady-state sequence, which is approximately ten times more than forconventional pulses, i.e., 3.4 W. Also, the maximum heat-sink thermal resistance has been evaluated using P_{IGBT}, P_{FWD}, P_{DR} with the thermal model independently for both types of transmission pulses. The results show that the thermal resistance of the heat-sink need not be more than 1.832 ^{o}C/W for both steady-state sequences and 19.01 ^{o}C/W for the conventional pulses. Finally, a heatsink has been designed, manufactured and installed with dimensions of 300 mm × 200 mm × 8 mm in the ApsuTx.

Table 1: Power dissipation of ApsuTx Components and Maximum thermal resistance of ApsuTx Heat-sink for Steady-State and Conventional Sequences.

	Steady State Sequence 1 (Grombacher et al., 2021)	Conventional Transmitter (Larsen et al., 2020)
Transmission Time (St)	10 millisecond per pulse	50 milliseconds (one pulse)
Receiving Time (ST)	100 millisecond per pulse	5 Second
P_{IGBT}	5.52 W	0.55 W
P_{FWD}	1.935 W	0.1935 W
P_{DR}	4.11 W	0.41 W
Total Power Dissipation of ApsuTx	33.93 W	3.4 W
Maximum Heat-sink Thermal Resistance	1.832 ^{o}C/W	19.01 ^{o}C/W

CONCLUSIONS

The new type of steady-state sequences brings new challenges for the Apsu system, particularly in the high-power transmitter. These continuous pulses result in higher electrical power dissipation in the ApsuTx. Therefore, thermal management becomes an essential component of the Apsu instrument development. This work focused on the thermal modelling of ApsuTx, which is used for the final design and development of the heatsink. Results showed that up to 33.93 W is dissipated by steady-state sequences, which are approximately ten times more than conventional pulses. This power can only be dissipated safely by the heatsink with a maximum thermal resistance of 1.832 ^{o}C/W. Finally, the heat sink has been designed and installed that has a lower thermal resistance than the maximum value. It is small, compact, and lightweight and provides great flexibility during remote field surveys.

ACKNOWLEDGMENTS

Funding for this work was provided by the Independent Research Fund Denmark. The authors like to thank Dr. Pradip Kumar Maurya and Christian Lundager Nedergaard for their significant contribution in this work.

REFERENCES

Larsen, J.J., Liu, L., Grombacher, D., Osterman, G. and Auken, E., 2020. Apsu—A new compact surface nuclear magnetic resonance system for groundwater investigation. Geophysics, 85(2), pp.JM1-JM11.

Lohrasbi, S., Hammer, R., Essl, W., Reiss, G., Defregger, S. and Sanz, W., 2020. A Comprehensive Review on the Core Thermal Management Improvement Concepts in Power Electronics. IEEE Access, 8, pp.166880-166906.

Keating, K., Binley, A., Bense, V., Van Dam, R.L. and Christiansen, H.H., 2018. Combined geophysical measurements provide evidence for unfrozen water in permafrost in the Adventdalen valley in Svalbard. Geophysical Research Letters, 45(15), pp.7606-7614.

Liu, L., Grombacher, D., Auken, E. and Larsen, J.J., 2019. Apsu: a wireless multichannel receiver system for surface nuclear magnetic resonance groundwater investigations. Geoscientific Instrumentation, Methods and Data Systems, 8(1), pp.1-11.

Grombacher D., Liu L., Griffiths M.P., Vang M.Ø. and Larsen J.J. 2021. Steady-state surface NMR for mapping of groundwater. (Under Review)

Magnetic resonance in weathered & fractured granite aquifer: case studies in Alsace

[1]JF Girard, [1]C Jodry, [1]PD Matthey, [1]J Porte, [2]C Dezayes, [2]C Lerouge, [1]MC Pierret, [1]N Lesparre

[1] Unistra, ITES
Strasbourg, France
jf.girard@unistra.fr

[2] BRGM
Orléans, France
c.dezayes@brgm.fr

SUMMARY

Hard-rock aquifers are known to be highly heterogeneous. Despite a low water content, they are useful but fragile water resources, especially in medium mountains in Alsace, north-east of France.

Exhumed crystalline basement rocks often exhibit altered facies, with fractures and faults either due to geological stresses or weathering process. They are particularly vulnerable to erosion and act as conduits, barrier or storage to fluids.

Thus, studying these structures, close to the surface or in depth, provides insights on exploitable aquifers for drinking water but also toward a better understanding of deep aquifers or geothermal resources.

Two studied sites were chosen for somehow a common lithology and providing boreholes data and outcrop respectively, allowing a description of the spatial distribution of physical properties. Magnetic resonance sounding and geoelectrical measurements were acquired on such sites to inform on their underground structrure and water content distribution.

Key words: MRS, geoelectrical methods, granite, fractures, Vosges mountains.

INTRODUCTION

Exhumed crystalline basement rocks often exhibit altered facies, with fractures and faults either due to geological stresses or weathering process. They are particularly vulnerable to erosion and act as conduits, barrier or storage to fluids (Roques et al., 2014). Therefore, hydrogeological behaviour is complex in the damage zone of the rocks with alteration products that can precipitate locally and increase or decrease permeability and porosity.

In this paper, geoelectrical measurements and Nuclear Magnetic Resonance Sounding measurements (MRS) have been performed on several sites in Alsace. Two of them are presented here, to evaluate the hydrological parameters and storage capacity of a granitic basement rock.

Geophysical surveys have already been used to characterize such heterogeneous medium (e.g. Baltassat et al., 2005). The aim of this study is to target the zones of expected higher porosity and permeability, i.e. the damage zone in fractured parts and the generally most altered zone at the top of the basement: the transition zone between the sediments and the crystalline rocks.

The selected sites have been investigated in the recent years for various objectives and their descriptions can be found in the literature (Pierret et al.,; Dezayes et al., 2021). Both sites are situated in the North East of France in the Vosges Mountain.

ST PIERRE BOIS QUARRY

The St Pierre Bois (SPB) site is included in an exploited carrier with a manmade outcrop allowing to visualise the geological contact between the granitic basement and the arkose overlying sediments (sandstone enriched in quartz, with a moderate porosity). It is particularly interesting to have access to the limit between basement rocks and sediment layers as this zone is often referred as a permeable target at depth down to several kilometres and cannot be easily studied. As it is, this particular outcrop can be considered as an analogue of the same transition zone at depth and its study aims at a better understanding of the hydrogeological properties and change in physical properties between the two compartments.

Figure 1. Picture of a man-made outcrop with – in red – bedding of the sedimentary deposit (sandstone) and – dotted white line – the geological limit between sandstone and the crystalline basement rock.

Three geophysical methods have been applied to acquire various and complementary physical properties. The electrical resistivity tomography (ERT) and the MRS were used to evaluate the resistivity of the medium and an estimate of its water content (i.e. saturated porosity). For the very shallowest part, some ground penetrating radar profiles allowed to describe, at a high resolution, the layers in the sedimentary part, until a maximum depth of 2.5m with 100 MHz antenna.

The outcrop of the quarry has been carefully described. Petrophysics properties have been evaluated for a selection of

samples, mainly providing matrix properties (Kushnir, 2018). Fracturation density and orientations (but also deposits in fractures) have been mapped and related to the regional context (Dezayes et al., 2021).

THE STRENGBACH CATCHMENT

The Strenbach catchment is a small basement watershed (80 ha) located at an altitude between 880 to 1150 m. Mainly covered by spruce forest, it benefits from a long-term hydrological and geochemical monitoring (since 1986): rainfall / snowfall, runoff, vegetation surveying, etc… (Pierret et al., 2018).

This site has been (and still today) thoroughly investigated with surface geophysics, including MRS (Boucher, 2015), ERT (Gance et al., 2015) and more recently with active surface and borehole seismic (Lesparre et al., 2020b) and passive seismic imaging and monitoring.

More than 25 MRS soundings performed at Strengbach site allowed estimating the varying thickness of the top weathered zone between 8 to 24 m which has the larger MRS porosity (3-5%), see figure 2 for instance. The underlying rock is characterized by a porosity < 2%, which is a higher value than fresh granite matrix porosity.

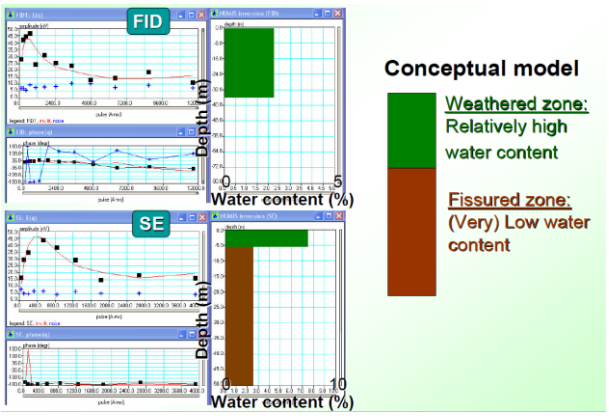

Figure 2. Sample of MRS data at a favorable site (n°5), both FID and spin echo (SE) sequences were used.

RESULTS & CONCLUSIONS

Spatial variations of MRS combined with soil, geology and geochemical information led to a hydrological model of Strengbach catchment with 5 zones. These zones were then used to define an initial hydrodynamic model, later refined after optimisation to fit the observed MRS data and hydrological records (Lesparre et al., 2020a).

In St Pierre Bois quarry, the upper sedimentary layer revealed a mean resistivity of 80 Ω.m and the presence of a perched aquifer within a 2 to 4% MRS porosity. Deeper, an increase of MRS water content, up to 3% far below the resistive contact with the basement was observed, revealing a significant storage at the top of basement.

On both studied sites, the signal to noise ratio is a key issue for MRS as in general on hard-rock aquifers. Surface MRS results were confirmed with borehole nuclear magnetic logging (NML), i.e. spatially variable water content within a weathered layer with ~ 3-5 % porosity overlying a thick hard rock aquifer with an average porosity < 2%.

ACKNOWLEDGMENTS

Many results used in this study were obtained during Master thesis financially supported by the ANR-15-CE06-0014 Cantare, the ANR-17-CE06-0012, and ADEME (French Agency of Energy and Environment) in the framework of the DEEP-EM project. The borehole NML data where acquired with the collaboration of LIAG, especially R. Dlugosch. We acknowledge the St Pierre Bois quarry owner for authorizing and facilitating the access to the site. We thank M. Boucher, M. Dumont, and many others who contributed to the field acquisitions on the Strengbach catchment. This MRS acquisition campaign was funded by CRITEX, INSU, and REALISE projects.

REFERENCES

Baltassat, J.M., Legchenko, A., Ambroise, B., Mathieu, F., Lachassagne, P., Wyns R., Mercier, J.L. and Schott J.J., 2005. Magnetic resonance sounding (MRS) and resistivity characterisation of a mountain hard rock aquifer: the Ringelbach Catchment, Vosges Massif, France. Near Surface Geophysics, 3(4), 267-274.

Boucher M., Pierret M.C., Dumont M., Viville D., Legchenko A., Chevalier A. and Penz S., 2015. MRS characterisation of a mountain hard rock aquifer : the Strengbach Catchment, Vosges Massif, France. MRS2015 :6th. 1-3

Dezayes, C., Lerouge, C., Innocent, C., Lach, P., 2021. Structural control on fluid circulation in a graben system: Constraints from the Saint Pierre Bois quarry (Vosges, France). Journal of Structural Geology, 104323.

Gance, J., Sailhac, P., Malet, J. P., Viville, D., & Pierret, M. C. (2015). Identification of weathered structures and aquifers from resistivity observations in the Strengbach catchment (Vosges, France). In EGU General Assembly Conference Abstracts (p. 12552).

Kushnir A, Heap M, Baud P, Gilg A, Reuschlé Th, Lerouge C, Dezayes Ch, Duringer Philippe (2018) Characterizing the physical properties of rocks from the Paleozoic to Permo-Triassic transition in the Upper Rhine Graben. Kushnir et al. Geotherm Energy (2018) 6:16.

Lesparre, N., Girard, J. F., Jeannot, B., Weill, S., Dumont, M., Boucher, M., Viville, D., Pierret, M.C., Legchenko, A., Delay, F. 2020a. Magnetic resonance sounding measurements as posterior information to condition hydrological model parameters: Application to a hard-rock headwater catchment. Journal of Hydrology, 587, 124941.

Lesparre, N., Pasquet, S., Ackerer, P., 2020b. Aquifer structure at the catchment scale inferred from a geostatical analysis of seismic refraction data. In AGU Fall Meeting Abstracts (Vol. 2020, pp. H129-04).

Pierret, M.-C., Cotel, S., Ackerer, P., Beaulieu, E., Benarioumlil, S., Boucher, M., Boutin, R., Chabaux, F., Delay, F., Fourtet, C., Friedmann, P., Fritz, B., Gangloff, S., Girard, J.-F., Legtchenko, A., Viville, D., Weill, S., Probst, A., 2018. The Strengbach Catchment: A Multidisciplinary Environmental Sentry for 30 Years. Vadose Zone Journal, 17(1), 180090.

Roques, C., Bour, O., Aquilina, L., Dewandel, B., Leray, S., Schroetter, J.M., Longuevergne, L., Le Borgne, T., Hochreutener, R., Labasque, T., Lavenant, N., Vergnaud-Ayraud, V. and Mougin, B., 2014. Hydrological behavior of a deep subvertical fault in crystalline basement and relationships with surrounding reservoirs. Journal of Hydrology, 509, 42-54

A surface NMR forward model for steady-state free-precession excitations

[1]M.P. Griffiths, [2]D.Grombacher, [2]M. Ø. Vang, [2]L. Liu and [1]J.J.Larsen

[1] Department of Electrical and Computer Engineering, Aarhus University, Aarhus, Denmark.
[2] Department of Geoscience, Aarhus University, Aarhus, Denmark.

SUMMARY

Steady-state free-precession (SSFP) sequences are a new style of surface NMR acquisition. Traditional processing and modelling workflows require adaptation to model this new style of aquisition. Here, we outline necessary modifications to model SSFP data that have been processed using a SSFP-specific version of spectral analysis. We validate our modelling by jointly inverting 12 unique SSFP sequences, with a resulting data-misfit of 1.01

Key words: surface NMR, multi-pulse excitations, numerical methods.

INTRODUCTION

Although steady-state free-precession (SSFP) excitations (Carr, 1958) have been widely employed in NMR, they have not been previously implemented in surface NMR. An example of these sequences is shown in Fig. **1a**. The critical difference between SSFP and single pulse excitations is that SSFP do not wait for a re-establishment of equilibrium with earth's ambient magnetic field between sub-sequent pulses. This means a much larger portion of the acquisition time translates to useable signal time-series. The distinct nature of these excitations requires a processing and modelling workflow tailored to match the train-style acquisition, compared with traditional SNMR measurements like the FID.

Here we outline a method of modelling SSFP excitations for SNMR. Our model directly predicts the response of SSFP sequence processed using a modified version of Spectral Analysis (SA) as formulated by Liu et al. (2019). As validation, we jointly invert 12 different SSFP sequences and find our model is capable of reproducing the SA envelopes.

METHODS

For all aspects, except the temporal components of the excitation, we follow the theory outlined by Weichman et al. (2000). While no fundamental reasons prevent the use of Weichman's framework to predict the full-time series of SSFP measurements, computational practicality associated with the sheer length of SSFP excitations prohibit this. Instead, we directly consider how the signal will manifest itself under a SA processing scheme.

The key characteristic of SSFP is that fact that magnetization eventually enters a steady-state. Figure **1** shows the magnetization response to a SSFP excitation, modelled using the Bloch equation (Bloch, 1946). The overlying in-phase magnetization, shown in Fig. **1a**, has entered a repeatable steady-state equilibrium around the 2 second mark of the pulse train. Sampling the magnetization immediately after each pulse, Figures **1b,c** show how with increasing time (coded with colours transitioning from purple to red), both the in-phase **(b)** and quadrature **(c)** components of the magnetization enter this

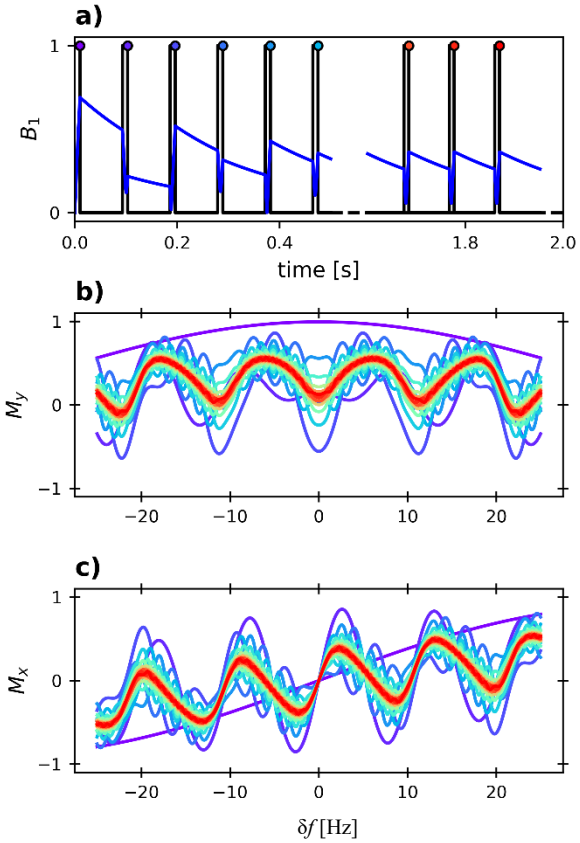

Figure 1. Magnetization response to steady-state free-precession excitation. ***a)*** *Excitation timing (black) with M_y overlying (blue). Colour dots mark the end of pulse timing where the magnetization has been sampled and have associated coloured curves in panels (b) and (c).* ***b)*** *M_y as a function of frequency offset (δf)* ***c)*** *M_x as a function of frequency offset (δf).*

steady-state equilibrium, for a range of frequency offsets (δf). We denote this SSFP equilibrium state as $M_{\perp}^{ssfp}(\delta f)$.

Using the analytical solution of the Bloch equation, we consider how a component of $M_{\perp}^{ssfp}(\delta f)$ contributes to the Fourier transform at the Larmor frequency over the course of a free-precession window:

$$X[t_i, \delta f] = \int_{t_{st}}^{t_{end}} M_{\perp}^{i}(\delta f)\, e^{\frac{-t}{T_2}} \cdot e^{i2\pi(f_0+\delta f)t} \cdot e^{-i2\pi f_0 t} dt \quad (1)$$

Carrying out the integration, we arrive at the expression,

$$X[t_i, \delta f] = M_{\perp}^{i}(\delta f) \frac{1}{-\beta} \cdot \left(e^{-\beta t_{end}} - e^{-\beta t_{st}}\right), \quad (2)$$

where $\beta = {}^{1}/_{T_2} - i2\pi\delta f$. From this, we observe that even though a magnetization component has a frequency offset from the transmit frequency, it contributes to the signal at this frequency. We refer to this frequency offset weighting as the

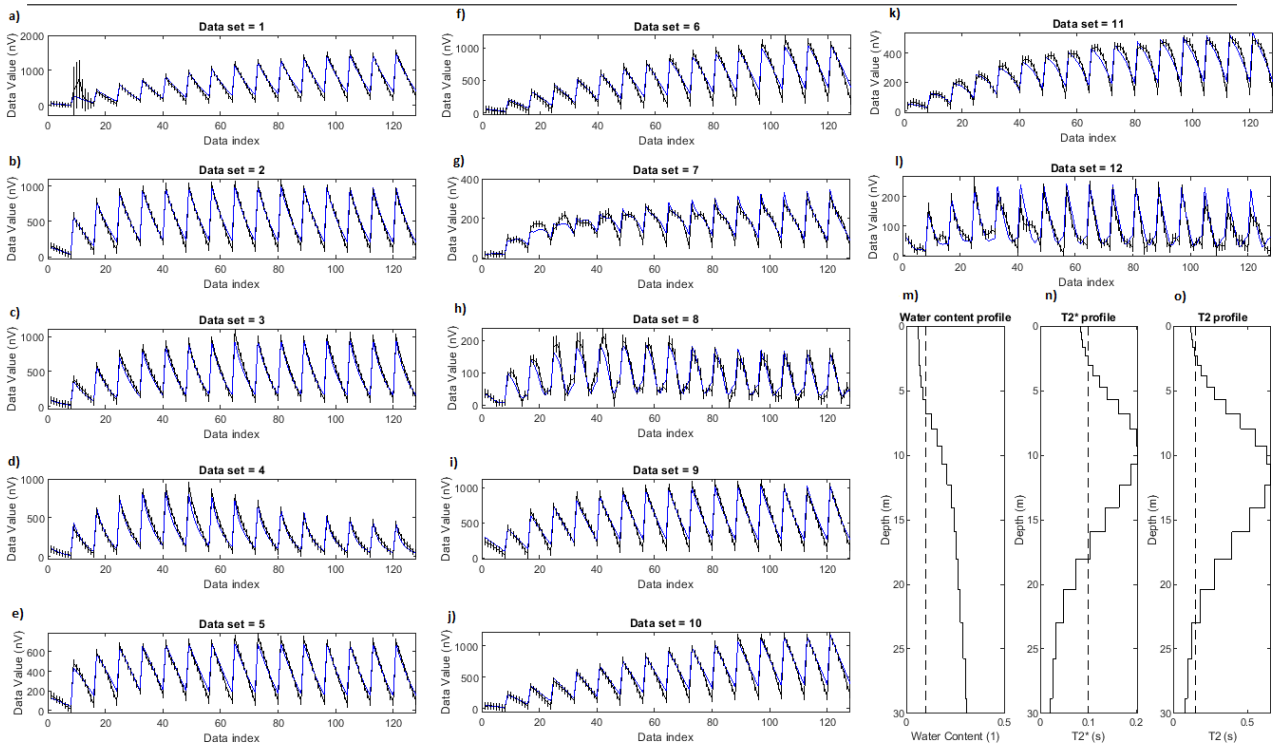

Figure 2 The twelve sequence inversion. ***(a)-(l)*** *Comparison of observed (black) and model (blue) data for each sequence (see Table 1).* ***m)*** *Inverted water content profile* ***n)*** *Inverted T2* profile* ***o)*** *Inverted T2 profile.*

projection efficiency. Relaxation time dependence is retained by sliding the start time (t_{st}) further along the free-precession window, creating a SA-decay curve. Based on the inhomogeneity of the background field, the components $M_{\perp}^{i}(\delta f)$ are weighted and summed to obtain the response due to particular voxel. The overall SNMR response is then computed by summing over all the voxels in the subsurface volume. On a practical level, we use two levels of fast-mapping based implementations. First, $M_{\perp}^{ssfp}(\delta f)$ solutions are fit with polynomials of T_2 using a GPU based solver (Griffiths et al., 2021). Next, fast-mapping polynomials are made for SNMR kernels in the likes of Grombacher et al. (2020) making subsequent inversions rapid.

RESULTS

A large suite of SSFP sequences (See Table 1) were acquired at a low-noise, high-signal site near Silkeborg, DK. The acquisition consisted of both alternating and in-phase steady state sequence transmitted on-resonance and at +/- 5Hz off-resonance. Each sequence has 16 current values between 1-80 amps. A smooth vertical-constraint was applied to regularize the inversion. The observed and modelled data are compared in **Fig. 2(a-l)** and the associated inverted model is displayed in **Fig. 2(m-o).** With a data misfit of 1.01, we see that the model nicely reproduces the SA decay curves, with only a few exceptional points being outside the error intervals. We consider the fact that a single model is capable predicting such a wide range of measurements as a good indication of the validity of our forward model (i.e. fitting 12 separate sequences simultaneously, that include multiple delay times, variable train type (in-phase versus out-of-phase), pulse durations, and transmit offsets). Furthermore, the layered structure seen in the relaxation profiles is consistent with structures found from TEM data acquired at the site. The fast-mapping based implementation of the forward allows for joint inversions of SSFP sequence suites in 30-40 seconds.

Fig. 2 panel	τ [ms]	delay [µs]	Style	$\delta f_{Transmit}$ [Hz]
a	10	92781	alt	0
b	10	92781	reg	0
c	10	185563	reg	0
d	40	371126	alt	0
e	10	92997	alt	-5
f	10	92997	reg	-5
g	10	185994	reg	-5
h	40	371989	alt	-5
i	10	92567	alt	+5
j	10	92567	reg	+5
k	10	185133	reg	+5
l	40	370267	alt	+5

Table 1 Parameters for sequences used in joint inversion. The pulse duration is τ , delay refers to how often pulses are repeated. An alternating (alt)-style sequence has a 180° phase shift between each pulse, regular (reg) –style sequence has all pulses in-phase with each other.

CONCLUSIONS

The introduction of SSFP excitation schemes to SNMR shows tremendous promise in the field of SNMR, primarily due to the efficiency gains in data acquisition. In a practical sense, the nature of these new excitation schemes requires a tailored modelling framework. Here, by formulating our forward model in terms of the product of spectral analysis processing, we find that modelling these measurements is practically realizable. Validation of our modelling is based on the joint inversion of 12 distinct steady-state sequences. The misfit of the inverted model is 1.01.

REFERENCES

Bloch, F., 1946. Nuclear induction, *Physical Review,* 70(7-8), 460-474

Carr, H., 1958. Steady-state free-precession in nuclear magnetic resonance, *Physical Review*, 112(5).

Griffiths, M.P., Grombacher D., & Larsen J. J., 2021. Efficient numerical Bloch solutions for multipulse surface NMR, *Geophysical Journal International*, 227(3), 1905–1916.

Grombacher, D., Kass, M. A., Auken, E., & Larsen J. J., 2020. An approximate fast-mapping approach to the surface NMR forward problem, *Geophysical Journal International*, 221(2), 928–937.

Liu, L., Grombacher, D., Auken, E., & Larsen, J. J. (2019). Complex envelope retrieval for surface nuclear magnetic resonance data using spectral analysis. *Geophysical Journal International*, 217(2), 894-905.

Weichman, P. B., Lavely, E. M., & Ritzwoller, M. H., 2000. Theory of surface nuclear magnetic resonance with applications to geophysical imaging problems, *Physical Review E,* 62(1 B), 1290-1312

A steady-state approach to surface NMR

[1]D Grombacher, [1]L. Liu, [2]M. Griffiths, [1]M.Ø. Vang, [2]J.J. Larsen

[1] Geoscience Department
Aarhus, Denmark

[2] Department of Electrical and Computer Engineering
Aarhus, Denmark

SUMMARY

Signal quality remains a major challenge in surface NMR, where it is common that multi-hour acquisitions are required at each site to produce satisfactory results. A major contributor to the long-measurement times is the need for a several seconds wait time in between subsequent measurements. Here we discuss the suitability of pulse train style acquisitions, called steady-state measurements, for surface NMR. We demonstrate its feasibility in the field and show data from several sites where a steady-state approach is able to produe a high fidelity NMR signal in a scenario where traditional free-induction decay measurements are unable to produce an observable signal given equal acquisition times. Ultimately, the steady-state scheme shows great potential to signficantly enhance signal quality and accelerate mapping speeds in surface NMR.

Key words: steady-state, signal-to-noise ratio

INTRODUCTION

A major challenge in surface NMR is the signal-to-noise ratio, as it is common that long measurement times return low-quality signals. The problem stems from the need to measure a low amplitude surface NMR signal in a high ambient noise background. Significant advances have been made in surface NMR signal processing[1,2], in receive[3,4], and transmit schemes[5,6], yet noise remains an issue. A pragmatic solution to improving signal quality involves time-consuming averaging of repeated measurements, which often results in excessively long measurement times that limit the number of sites that can be measured per day and reduces the regional mapping capabilities of surface NMR.

Here we show that a steady-state scheme for surface NMR, enabled by recent advances in transmitter capabilities[7] and numerical modeling[8], delivers orders of magnitude signal enhancements compared to traditional free-induction decay schemes. The new technique is a highly efficient measurement style that is both narrowband and utilizes the full measurement interval in contrast to traditional approaches. We demonstrate both the feasibility of a steady-state protocol for surface NMR and that it enables high-fidelity groundwater measurements at high-speeds in hitherto inaccessible areas.

METHODS

To produce images of the subsurface water contents and relaxation times using surface NMR, a sounding approach is employed that involves measuring the NMR signal produced by excitation pulses of varying peak current amplitude. The variable currents manipulate the spatial origin of the measured signals, allowing an inversion framework to be used to image the underlying water contents and relaxation times consistent with the data. Standard field practices in surface NMR involve the use of a measurement called a free-induction decay (FID), which measures the NMR signal produced by a single pulse (Fig. 1A). An FID measurement involves a several seconds long wait time in between subsequent measurements to allow the magnetization to return to equilibrium prior to the next measurement. This return to equilibrium is necessary to satisfy an implicit assumption in standard surface NMR forward modelling and is a major reason for slow acquisition speeds in surface NMR. For example, it is common that at least 50 repeated measurements for 15-20 different current amplitudes are required to produce satisfactory data quality and depth resolution. This translates to measurements lasting many hours at each site.

Although the FID is the staple measurement in surface NMR, other NMR disciplines employ far more complex acquisition sequences, often involving the use of pulse trains consisting of closely separated pulses. For example the CPMG measurement, which has been implemented previously in surface NMR[9]. Of interest in this work is steady-state measurements that involve the use of trains of identical pulses separated by a constant repetition time t_{rep} (Fig. 1A). The primary advantage of these pulse train measurements is that the close separation of the pulses enormously reduces the wait time between subsequent measurements.

For steady-state measurements, the defining sequence parameters are the flip angle θ induced by each pulse and t_{rep}. If one knows the T_1 relaxation time, a θ and t_{rep} pair can be selected to optimize the signal intensity; this is referred to as the Ernst angle (equation 1).

$$\cos(\theta_E) = e^{-t_{rep}/T_1} \quad \Leftrightarrow \quad t_{rep} = -T_1 \ln cos(\theta_E). \quad (1)$$

Unfortunately, it's not so straightforward to optimize a steady-state sequence for surface NMR. Firstly, we don't know what T_1 is at depth, and secondly, we are unable to produce a uniform flip angle everywhere in the subsurface. However, we can constrain the range of plausible T_1 we're likely to encounter, as well as the range of applied magnetic field strengths (B_1) generated by a surface NMR pulse. If we select a representative pulse duration, eg. 20 ms, equation 2 can be used to calculate the flip angle produced by each B_1 in the subsurface.

$$\theta \quad = \gamma B_1 \tau \quad (2)$$

γ and τ the gyromagnetic ratio of the hydrogen nuclei, and pulse duration, respectively. Consider a toy problem where we pose the question, if the flip angle induced at each location in the subsurface did correspond to the Ernst angle, what t_{rep} would be required to optimize the signal intensity? This is a non-physical scenario, but posed here to gain insights into what range of t_{rep} are needed to optimize signal intensity within a voxel where a uniform flip angle has been produced. Figure 1B illustrates the optimal t_{rep} for a range of B_1 representative of surface NMR transmit conditions (where the flip angle at each x-position is calculated using equation 2 and τ=20 ms). The three curve correspond to three T_1 values, spanning the range of commonly encountered relaxation times. Note that the curves in Figure 1B generally fall in the 10s to 100s of milliseconds range – several orders of magnitude smaller than the standard ~3 s wait times commonly employed in surface NMR (highlighted by the horizontal black line in Figure 1B). This significant gap in wait times between standard practice and that calculated by equation 1 suggest significant gains may be realized through a dramatic reduction in wait times. Note that one can only select a single t_{rep} at a time, so it is not possible to optimize performance for every single B_1 value simultaneously. But what is possible, is

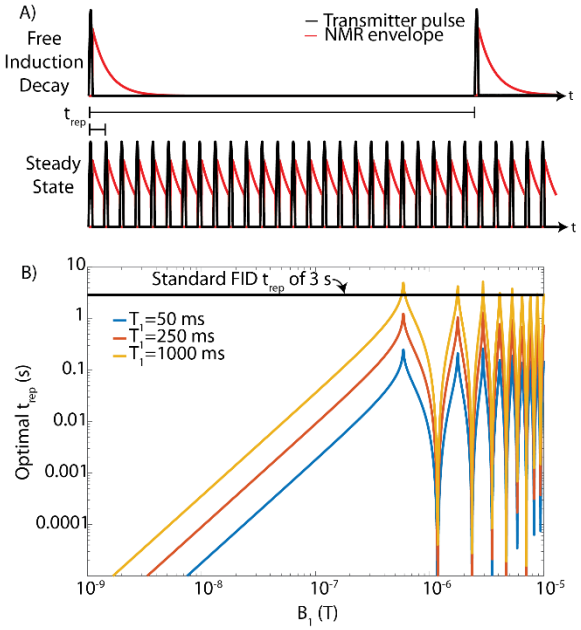

the selection of a single t_{rep} that is significantly closer to these optimal values than the current 3 second wait time.

Figure 1. A) Illustrations of the standard free-induction decay measurement, a steady-state measurement, and their different repetition times. A single bump (black) corresponds to the envelope of a single transmitter pulse. The envelope of the NMR signal is shown in red. Measurement intervals correspond to times when the transmitter current is off, i.e. flat black intervals. B) *The repetition time leading to optimum signal intensity based on the Ernst angle equation for a typical range of surface NMR conditions. The black line shows the standard surface NMR repetition time.*

RESULTS

Here we present data collected at 4 sites across Jutland, Denmark, representative of typical agricultural settings in Denmark. Two acquisition schemes are compared: 1) the standard FID using a 40 ms on-resonance pulse with a 3 s repetition time and 2) a steady-state scheme employing a 10 ms on-resonance pulse with a 93 ms repetition time. The two acquisition schemes are given equivalent acquisition durations for head-to-head comparison.

For each site, representative steady-state and FID spectra are presented in the left column of Figure 2. A high-quality NMR signal will appear as a clear peak at the local Larmor frequency. We also present sounding curves in the right column of Figure 2, which are formed by measuring the NMR signal peak at the Larmor frequency as a function of the pulse index, where small and large pulse indices correspond to small and large currents, respectively. A high-quality signal corresponds to a smooth curve where amplitudes clearly exceed the noise. The circled data point in the sounding curves correspond to the spectra illustrated in the left column of Figure 2.

NMR peaks are easily identified (highlighted by black arrows) in the steady-state spectra (left column of Figure 2, black curves). In Fig. 2A, C, G, we observe peaks that rise out of the noise by a factor of 20-50. In Fig. 2E, higher ambient noise levels and lower signal amplitude lead to a steady-state peak that exceeds the noise by a factor of ~4. In contrast, a clear NMR peak is impossible to locate in the FID spectra (Fig. 2A, C, E red curves) and these spectra show only background noise. A clear FID peak is seen in Fig. 2G (red arrow). This is a low noise site, where the traditional approach also produces a clear NMR signal. Note that the different frequency resolution in the spectra is a consequence of the different processing workflows in each case, where both cases are given identical processing steps – except that the steady-state spectra is formed by concatenating the entire time series, zeroing the pulse-corrupted portions, and then taking the Fourier transform. In contrast, all one second FID measurements are stacked to form a single averaged one second time series, which is then Fourier transformed resulting in the lower ~ 1 Hz frequency resolution. The sounding curves show similar results (right column of Figure 2). Smooth large amplitude curves are obtained with the steady-state approach (black), while the FID approach (red) is unable to produce a clear NMR signal. It is only in Fig. 2h that the FID sounding curve is smooth and clearly exceeds the noise level, but with an amplitude significantly less than for the steady-state case. Note that the sounding curves formed for the FID cases are produced by taking a discrete Fourier transform at the estimated Larmor frequency – a non-traditional approach to form a FID sounding curve. This alternative approach is done here to provide a more direct comparison of the peak NMR signals in the spectra.

DISCUSSION

The steady-state sequence has several attractive features. Firstly, the enhanced acquisition rate, where repetition times are in the 100s of millisecond range represents an enormous stacking rate increase compared to traditional approaches. The result is that hundred to thousands of stacks can be collected in short durations (eg. roughly 600 or 1200 stacks in approximately 1 or 2 minutes of acquisition for the spectra in Figure 2). The expedited stacking rate allows steady-state schemes to produce large amplitude signals in short durations. Note that on a single stack-to-single stack basis, the FID signal is likely larger than the steady-state signal, but because of the increase in stacking rate, the net stacked signal amplitude may exceed that of the FID.

A second advantage is the collapse of the NMR signal into a very narrow band – observed by noting that the NMR peaks in the steady-state spectra are extremely narrow – much narrower than the expected bandwidth of the NMR signal. The collapse to a narrow peak is a consequence of the train-style acquisition in combination with the processing scheme that involves concatenating the full time series. This collapse has the distinct advantage that the relevant noise bandwidth affecting the

signal-to-noise ratio is extremely small – roughly equal to the inverse of the full time series length (eg. 1/60 Hz for a 60 second time series). This represents a several orders of magnitude reduction in the noise bandwidth compared to traditional synchronous detection approaches employing low-pass filters with several hundred Hz of bandwidth. Secondly, the signal collapse does not prohibit measurement of the full NMR signal's bandwidth – rather all Larmor frequency components are projected in the narrow peak observed in the spectra – thus enabling one to recover the total amplitude of the signal needed to estimate the water content.

A third advantage of the steady-state approach is that it represents a more efficient use of the full measurement interval. Traditional schemes involving longer wait times correspond to acquisitions where the NMR signal is fully decayed (or not being measured) for the majority of the time in the field. For example, 1 second of data is recorded every 3 seconds. In contrast, the steady-state approach drives the signal in to an altered equilibrium that can be repeatedly measured indefinitely. That is, the steady-state signal can be measured for the entire duration without significant "off-times" where the signal is not being measured. Note that the start of each pulse train must be culled while the signal is in a transient stage as it approaches the steady-state. This interval in the range of 2-5 seconds typically.

These first implementations of the steady-state schemes are based on non-optimized combinations of pulse sequences and pulse moment sampling. Future work will investigate optimal combinations of sequence/moments allowing satisfactory resolution with the fewest total measurements.

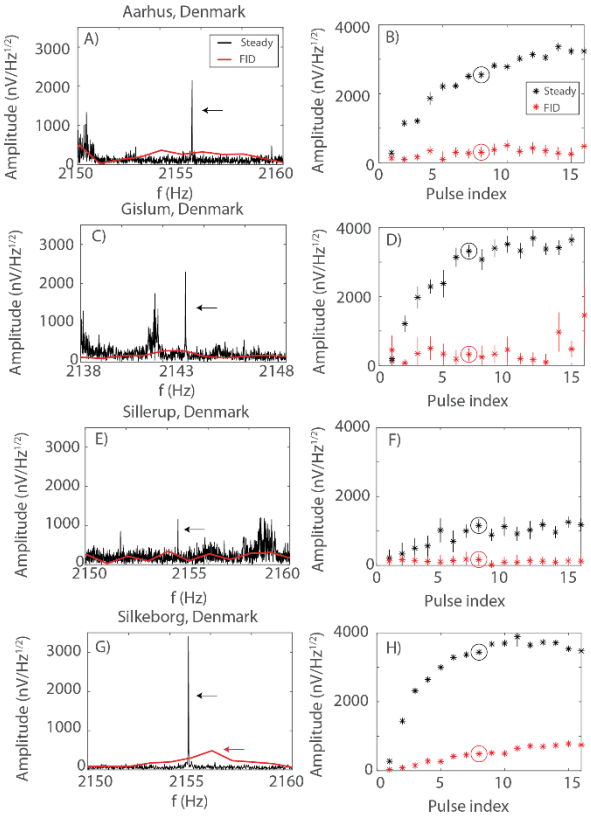

Figure 2. Comparison of data quality for the steady-state approach (black) and the standard free-induction decay (red) at four different sites. The left column shows frequency spectra, and the right column shows the sounding curves obtained at each site. The circles indicate the data shown in the left column. Black arrows in the top row show the measured local Larmor frequency and the location of the steady-state peak. The red arrow in G highlights the FID peak. The FID and steady-state spectra have different frequency resolutions due to the different lengths of the time series used in the DFT.

CONCLUSIONS

A steady-state protocol for surface NMR is demonstrated to be feasible in the field, and to offer significant signal-to-noise benefits compared to the classic free-induction decay approach. The primary advantages of the scheme involve a greatly improved stacking rate, more efficient use of the full measurement interval, and the enabling of processing schemes capable of enormous noise bandwidth reductions. Overall, the steady-state scheme shows great promise to improve signal quality in surface NMR and to enhance mapping speeds.

ACKNOWLEDGMENTS

This work was supported by funding from Independent Research Fund Denmark.

REFERENCES

[1] Müller-Petke, M. & Costabel, S. (2014). Comparison and optimal parameter settings of reference based harmonic noise cancellation in time and frequency domains for surface-NMR: Near Surface Geophysics, **12**, no. 2, 199-210.

[2] Liu, L., Grombacher, D., Auken, E. & Larsen, J. J. (2019). Complex envelope retrieval for surface nuclear magnetic resonance data using spectral analysis. *Geophysical Journal International*, **217**(2), 894-905.

[3] Trushkin, D. V., Shushakov, O. A. & Legchenko, A. V. (1994). The potential of a noise-reducing antenna for surface NMR groundwater surveys in the earth's magnetic field. *Geophysical Prospecting*, **42**(8), 855-862.

[4] Müller-Petke, M. & Costabel, S. (2014). Comparison and optimal parameter settings of reference based harmonic noise cancellation in time and frequency domains for surface-NMR: Near Surface Geophysics, **12**, no. 2, 199-210.

[5] Grunewald, E., Grombacher, D. & Walsh, D. (2016). Adiabatic pulses enhance surface nuclear magnetic resonance measurement and survey speed for groundwater investigations. *Geophysics*, **81**(4), WB85-WB96.

[6] Legchenko, A., Vouillamoz, J.M. & Roy, J. (2010). Applications of the magnetic resonance sounding method to the investigation of aquifers in the presence of magnetic materials, *Geophysics*, **75** (6), L91-L100.

[7] Larsen, J. J., Liu, L., Grombacher, D., Osterman, G. & Auken, E. (2020). Apsu—A new compact surface nuclear magnetic resonance system for groundwater investigation. *Geophysics*, **85**(2), JM1-JM11.

[8] Grombacher, D., Behroozmand, A. A. & Auken, E. (2017). Accounting for relaxation during pulse effects for long pulses and fast relaxation times in surface nuclear magnetic resonance. *Geophysics*, **82**(6), JM23-JM36.

[9] Grunewald, E. & Walsh, D.O. (2013). Multiecho scheme advances surface NMR for aquifer characterization, *Geophysical. Research Letters*, **40**, 6346-6350.

Accounting for the excitation pulse shape in modelling prepolarized surface nuclear magnetic resonance (SNMR-PP)

[1,2]Thomas Hiller, [2]Stephan Costabel, [2]Raphael Dlugosch, [1]Mike Müller-Petke

[1] Leibniz Institute for Applied Geophysics, Hannover, Germany
[2] Federal Institute for Geosciences and Natural Resources, Germany

SUMMARY

Recently, small-scale surface nuclear magnetic resonance (SNMR) measurements with a footprint of a few square meters have gained interest in the SNMR community. By applying a strong static prepolarizing (PP) magnetic field that enhances the measurable magnetization in the subsurface, it is possible to conduct field experiments that investigate water content distributions up to depths of about 1-2m. Several authors have shown the general feasibility of the SNMR-PP approach either on water reservoirs or on real soils. However, when comparing our forward modelling results with real field experiments, we found that there might be differences due to the excitation pulse shape, especially for long pulse times. We present these findings here to open a discussion in the community about the possible origins of the observed discrepancies.

Key words: prepolarization, pulse shape, spin-dynamics.

INTRODUCTION

Surface nuclear magnetic resonance (SNMR) is a well-established method for groundwater exploration and non-invasive aquifer characterization (e.g. Behroozmand et al., 2014). Its main benefit is the direct sensitivity towards the ^{1}H spin magnetization of the water molecule and therefore the ability to detect water in the subsurface. While generally used for aquifer characterization with surface loop sizes of up to 150m, investigations of the soil water content in the vadose zone require loop sizes with a footprint of only a few square meters. Unfortunately, these small-scale SNMR measurements with surface loop sizes of 1-2m diameter, exhibit very small signal amplitudes and therefore poor signal-to-noise ratios. To enhance the measureable SNMR signal strength, de Pasquale and Mohnke (2014) suggested the prepolarization (PP) technique, as known from e.g. Earth's field NMR, and demonstrated its benefit in a theoretical study. By applying a strong prepolarizing B-field prior to the actual spin excitation, the local magnetization is enhanced and therefore creates significantly increased SNMR signal amplitudes. Lin et al. (2018) and Costabel et al. (2019) experimentally demonstrated the success of this approach with measurements on water reservoirs, while Hiller et al. (2021) and Costabel et al. (2021) showed the general feasibility on soil.

Figure 1a compares modelled and measured sounding curves on a water basin for a similar setup as described in Hiller et al. (2021). While the modelled sounding curve fits well to the pulse moments smaller than about 0.1 As, there is an obvious deviation from the measurements with increasing larger pulse moments (marked by arrows). We hypothesize that this could be an effect of the SNMR-PP device and how the particular excitation pulse shapes are generated.

EXCITATION PULSE SHAPES

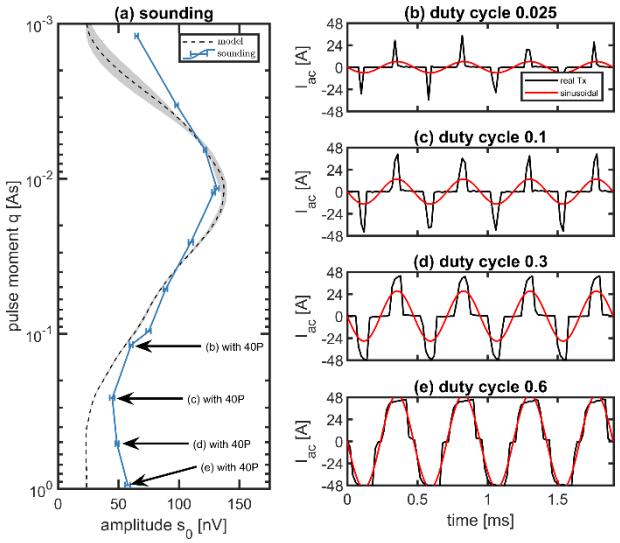

*Figure 1: (**a**) measured (blue) and modelled (black dashed) SNMR-PP sounding curve on a water basin; (**b-e**) first four periods of real Tx-pulse shapes (black) with different duty cycles and corresponding sinusoidal pulses (red).*

The transmitter unit of our SNMR-PP device (NMR MIDI, Radić Research) does not utilize a tuned circuit to amplify the Tx-pulses. Instead, the alternating Tx-field is generated by a series of short rectangular DC-pulses with a pulse rate corresponding to the local Larmor frequency. One advantage of this method is the relatively simple implementation in terms of electronic components compared to a tuned circuit. For this particular setup, the pulse moment can be controlled in two ways: (i) the voltage of the Tx-pulse can be set to either 12V, 24V or 48V or (ii) the duty cycle of the rectangular DC-pulse program can be arbitrarily adjusted from 0.025 to 0.6. With these options, it is possible to generate pulse moments in the range of about 0.001-1As with pulse lengths ranging from 0.5 to 35ms, respectively.

Figure 1b-e shows the first periods of four different excitation pulses each exhibiting a different duty cycle. In this study, the pulse moments in question (cf. Fig. 1a – black arrows) consist of 40 periods yielding a pulse length of about 19ms (at 2210 Hz). The red curves in Fig. 1b-e are the corresponding sinusoidal pulses with an equivalent pulse moment. In the following, we want to focus on the effect of the exact

excitation pulse shape on the forward modelling of the SNMR-PP signal.

FORWARD MODELING OF SNMR-PP

In Figure 2a, we exemplarily show a typical SNMR-PP measurement sequence as used in our previous studies. Note that the timings given in Fig. 2a refer to the measurement protocol as reported by Hiller et al. (2021) and are determined by the available settings of our SNMR-PP device. Initially, a strong static PP-field is generated by a large DC current, driven through a multi-turn cooper loop. The on-time of the PP depends on the T1 relaxation time of the medium under study and is set here (water basin) to the maximum of 5s. At the end of the PP, the PP-field is switched off within 1ms (green curve) by ramping down the PP current with a half cosine shape. After a minimum wait time of 4ms, an on-resonant electromagnetic pulse (Tx) at the local Larmor frequency excites the hydrogen protons and after an additional 5ms dead time, the NMR response, as free induction decay (FID), is recorded.

Until now, most studies considering SNMR-PP applications assume that the PP switch-off is perfectly adiabatic (de Pasquale and Mohnke, 2014; Lin et al., 2018) and that the enhancement of the local magnetization solely depends on the amplification performance of the PP-loop. Conradi et al., 2017 showed that a reasonable degree of adiabaticity can be achieved with adapted switch-off ramp shapes and rather long switch-off times (about 10-20ms). As demonstrated in a numerical study by Hiller et al. (2020), the effect of ramp shape and short ramp times on the orientation of the magnetization after the PP switch-off cannot be neglected. Under relevant practical conditions used for soil moisture investigations, there are always regions below the SNMR-PP loop setup where the PP switch-off is non-adiabatic (Hiller et al., 2021).

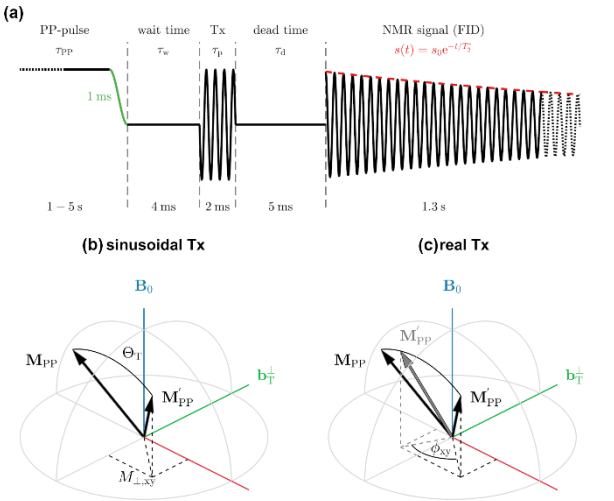

*Figure 2: (**a**) sketch of a SNMR-PP pulse sequence as used by Hiller et al. (2021); (**b+c**) sketch of the geometrical relations; orientation of the enhanced magnetization $\mathbf{M}'_{pp}$ after an imperfect prepolarization switch-off and a subsequent Tx-excitation with (**b**) an idealized sinusoidal and (**c**) a real Tx current wave form (grey); the horizontal phase angle ϕ_{xy} is the angle between the two solutions of (b) and (c).*

We account for the PP switch-off in our SNMR-PP forward modelling by solving the underlying Bloch equation with the software BLOCHUS (Bloch Universal Simulator - https://github.com/ThoHiller/nmr-blochus) and insert the resulting magnetization into the modelling tool MRSMatlab (Müller-Petke et al., 2016). As a result, instead of being parallel with the local Earth's magnetic field $\mathbf{B}_0$ as it would be the case for perfectly adiabatic conditions, the enhanced magnetization $\mathbf{M}_{\mathrm{pp}}$ is deflected from the direction of $\mathbf{B}_0$ after the PP switch-off (cf. Fig. 2b+c).

In addition to the PP switch-off, we now also apply the spin dynamics simulation to the Tx-pulse. This has the advantage that it is possible to consider the exact Tx-pulse shape as recorded by the device. In contrast, MRSMatlab accounts for the Tx-pulse in a rotating frame of reference and hence under the ideal assumption of a sinusoidal excitation pulse. Figure 2b+c sketches the difference between these two approaches. In panel (c) of Fig. 2, the grey arrow $\mathbf{M}'_{\mathrm{pp}}$ indicates the orientation of the enhanced magnetization after the application of a real Tx-pulse shape, while the black arrow $\mathbf{M}'_{\mathrm{pp}}$ refers to the idealized sinusoidal Tx-pulse shape (same as in panel b). We designate the difference between these two solutions with the angle ϕ_{xy}, which is essentially the angle between the two corresponding perpendicular components (perpendicular with respect to the Earth's magnetic field).

RESULTS

Due to the limited availability of computational capabilities, we were not able to model the complete sounding curve of a real measurement for a direct comparison. Doing so, would have required the calculation of sixteen individual pulse wave forms each with a different number of periods and duty cycles for every sub volume of the discretised subsurface. Instead, and to get a brief idea of the possible effects, we calculated the magnetizations $\mathbf{M}'_{\mathrm{pp}}$ in a layer 0.03m below the surface for three different real Tx-pulse shapes and their corresponding sinusoidal equivalents with our software BLOCHUS and compared the individual results to the solutions obtained with MRSMatlab.

Figure 3 summarizes the results of this numerical experiment. In panels (a) to (c) the three Tx-pulses are plotted with their sinusoidal counterparts. The Tx-pulses in panel (a) and (b) have a duty cycle of 0.025 and consist of two and four periods, respectively. The Tx-pulse in panel (c) has a duty cycle of 0.6 and consists of 40 periods. The resulting pulse moment is given in the title of the corresponding panel.

In panels (d) to (f), we plot the angle ϕ_{xy} between the solution for a sinusoidal Tx-pulse shape calculated with BLOCHUS and the rotating frame of reference approach of MRSMatlab. The dashed circles indicate the position of the PP (red) and Tx (black) coil, respectively. Technically, this comparison can be regarded as a numerical benchmark for the BLOCHUS implementation, which solves the Bloch equations in a laboratory frame of reference. Both solutions are identical up to machine precision and the visible pseudo-patterns are attributed to the sensitivity of the trigonometric functions for very small numbers. Note that the colour scale ranges from 0.000001° (blue) to 0.001° (red) and depends solely on the chosen accuracy of the implemented ODE solver.

In strong contrast to these findings are the results for the real Tx-pulse shapes presented in panels (g) to (i). Note that the colour scale now ranges from 0.1° (blue) to 180° (red) and shows therefore a difference of more than five orders of

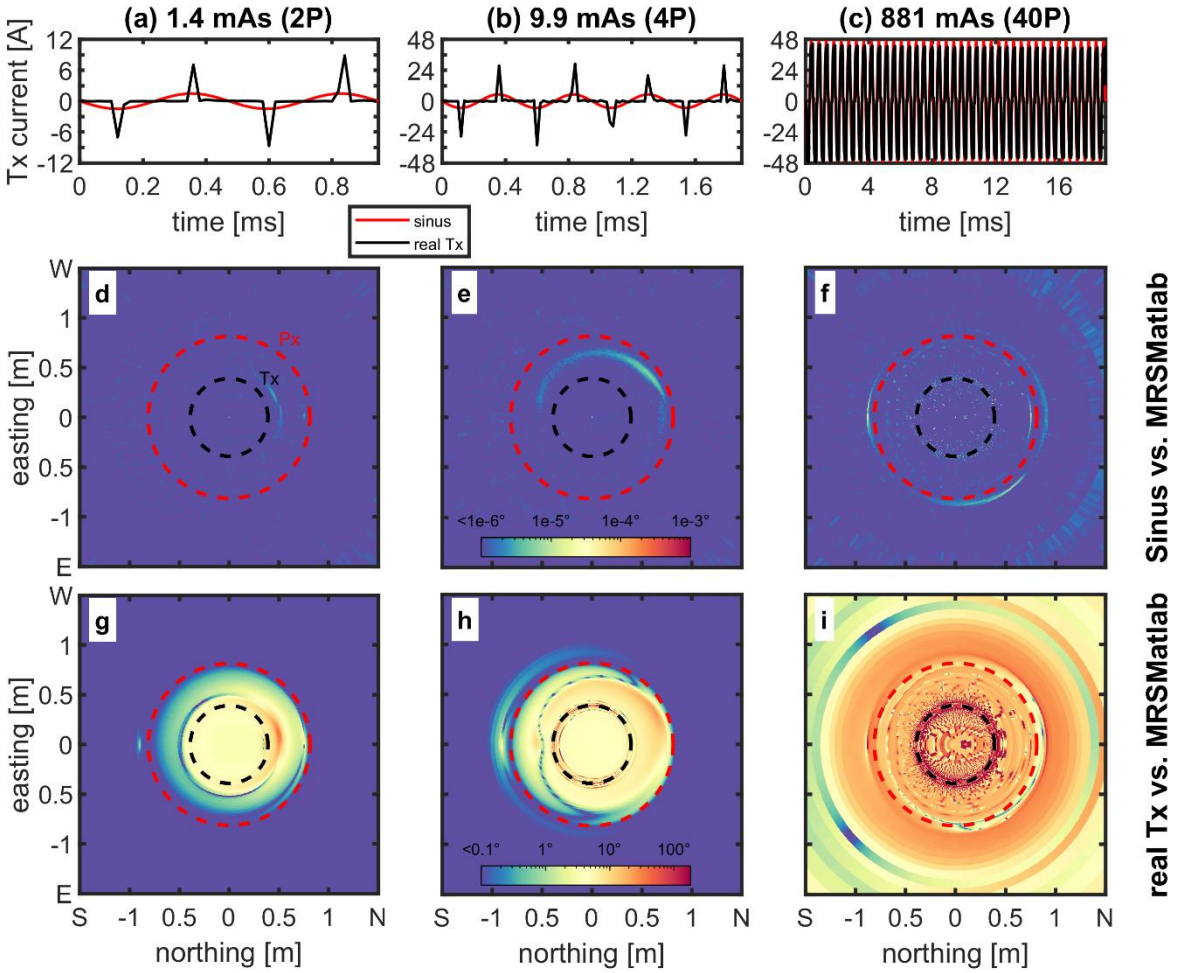

*Figure 3: (**a-c**) Real Tx-current wave form (black) and corresponding idealized sinusoidal wave forms (red) for three different pulse moments; (**d-f**) horizontal angle ϕ_{xy} (cf. Fig. 2c) between the solutions for $\boldsymbol{M}'_{pp}$ calculated by BLOCHUS and MRSMatlab for a sinusoidal Tx-current wave form simulated in a z-layer 0.03m below the surface; (**g-i**) same as (d-f) but for the real Tx-current wave forms; Note that the colour scale for (d-f) is five orders of magnitude smaller compared to the colour scale for (g-i).*

magnitude. Clearly, there is a strong effect of the Tx-pulse shape on the orientation of the magnetization vector. For a pulse moment of q = 1.4mAs (g) the deviations are localized inside the PP-coil and range up to 46°. For a pulse moment of q = 9.9mAs (h) the deviations extend also to the outside region south of the PP-coil but are of similar magnitude. Even more striking are the results in panel (i), where the deviations especially close to the Tx-coil reach up to 180°. Also outside of the PP- coil, there is no region that is unaffected by this effect. It seems that the longer the Tx-pulse is the larger is the deviation from the idealized solution.

DISCUSSION & CONCLUSION

Of course, there remain open questions concerning the findings of our study. First, we need to evaluate if the observed discrepancies in Fig. 3 stem from the combination of a non-adiabatic PP switch-off and the subsequent non-ideal Tx-pulse shape or if this is an effect of the Tx-pulse shape alone. Furthermore, as we only modelled the magnetization in one depth layer, it is not clear how strong the effect is after integrating over the whole volume and how significant are the effects on the final sounding curve.

Besides the use of more performant computational resources, a possible way to overcome the computational limitations could be the application of graphical processing units (GPU) to speed up the calculation of the Bloch equations as shown by Griffiths et al. (2021). However, first an evaluation is necessary how the underlying polynomial approach is suited for the irregular Tx-pulse shapes as used in this study.

As long as the employed Tx-pulse shapes are not sinusoidal and therefore much easier to address numerically, it might be necessary in one way or another to account for the Tx-pulse shape in future studies.

REFERENCES

Behroozmand, A., Keating, K. & Auken, E., 2015. A review of the principles and applications of the NMR technique for near-surface characterization, Surveys in Geophysics, 36(1), 27-85.

Costabel, S., Hiller, T., Radic, T., Dlugosch, R., & Müller-Petke, M. (2019). Surface Nuclear Magnetic Resonance Measurements in Berlin - Proof-Of-Concept for Applying the Prepolarization Technique in Urban Areas. In Conference proceedings, 25th European meeting of environmental and engineering geophysics (Vol. 2019, pp. 1).

Costabel, S., Hiller, T., Dlugosch, R. & Müller-Petke, M., First field experiments using surface nuclear magnetic

resonance with prepolarization (SNMR-PP), 2021, submitted to the 8th International Workshop on Magnetic Resonance Sounding, Strasbourg, France.

Conradi, M.S., Altobelli, S.A., Sowko, N.J., Conradi, S.H. & Fukushima, E., 2017. Pre-polarization fields for earth's field NMR: Fast discharge for use with short T1 and large coils, J. Magnet. Reson., 281(Supplement C), 241-245.

De Pasquale, G., & Mohnke, O., 2014. Numerical study of prepolarized surface nuclear magnetic resonance in the vadose zone. Vadose Zone Journal 13(11), 1-9.

Griffiths, M., Grombacher, D., & Larsen, J., 2021. Efficient numerical Bloch solutions for multipulse surface NMR. Geophysical Journal International, 227(3), 1905-1916.

Hiller, T., Dlugosch, R., & Müller-Petke, M., 2020. Utilizing pre-polarization to enhance SNMR signals - effect of imperfect switch-off. Geophysical Journal International, 222(2), 815-826.

Hiller, T., Costabel, S., Radić, T., Dlugosch, R., & Müller-Petke, M., 2021. Feasibility study on prepolarized surface nuclear magnetic resonance for soil moisture measurements. Vadose Zone Journal, e20138.

Lin, T., Yang, Y., Teng, F. & Müller-Petke, M., 2018a. Enabling surface nuclear magnetic resonance at high-noise environments using a prepolarization pulse, Geophys. J. Int., 212(2), 1463–1467.

Müller-Petke, M., Braun, M., Hertrich, M., Costabel, S. & Walbrecker, J., 2016. MRSmatlab – a software tool for processing, modeling, and inversion of magnetic resonance sounding data, Geophysics, 81(4), WB9–WB21.

Small-loop surface NMR and high resolution ERT soil evolution monitoring at the Midtre Lovénbreen glacial forefield in Ny-Ålesund, Svalbard

[1,2]**Trevor Irons** tirons@mtech.edu
[3]**Mihai Cimpoiasu** mcim@bgs.ac.uk
[3]**Oliver Kuras** oku@bgs.ac.uk
[3]**Harry Harrison** hharr@bgs.ac.uk
[2]**Dane Liljestrand** dane.liljestrand@utah.edu
[5,6]**James A. Bradley** jbradley.earth@gmail.com
[3]**Paul Wilkinson** pbw@bgs.ac.uk
[4]**Pacifica Sommers** Pacifica.Sommers@colorado.edu
[2]**Carlos Oroza** carlos.oroza@utah.edu
[4]**Steve Schmidt** steve.schmidt@colorado.edu
[3]**Jonathan Chambers** jecha@bgs.ac.uk

[1]Montana Tech, Butte, MT, USA
[2]University of Utah, Salt Lake City, UT, USA
[3]British Geological Survey, Nottingham, United Kingdom
[4]University of Colorado, Boulder, Boulder, CO, USA
[5]Queen Mary University of London, London, United Kingdom
[6]GFZ German Research Centre for Geosciences, Potsdam, Germany

SUMMARY

Widespread glacier retreat in the Arctic due to climate change is resulting in rapid ecosystem changes which are not fully understood. Geophysical methods can complement biological and chemical measurements to better understand soil evolution in glacier forefields following glacier retreat. In this study preliminary data from a long-term electrical resistivity tomography installation near Ny-Ålesund, Svalbard are presented with accompanying small loop surface NMR data. The NMR data provides valuable information on liquid-phase water and calibration for the ERT data. Our study provides the first [shallow-depth (<2m) surface NMR] data for a remote Arctic forefield, shedding light on the non-saturated state of the subsurface media.

Key words: vadose zone, soil moisture, small-loop NMR, ERT

INTRODUCTION

Ice retreat in the Arctic exposes vast barren expanses of pioneer soils. Over timescales of decades to thousands of years, these desolate and seemingly lifeless areas transform into arctic tundra—supporting a diverse ecological community. Important biological and geomorphological questions about this transition remain unanswered. These include the net carbon balance, the rate of physical, biological and chemical change, and the processes affecting these developments. Much of the initial soil development is thought to be driven by (micro-)biological processes (Botnen et al., 2020). Biological and ecological modelling can shed light on soil development processes and make predictions (Bradley et al., 2015). Data are critical to these ecological models, including: microbiological data, soil moisture (including aggregate state, i.e. frozen vs. liquid phase), seasonal variability, and soil temperature profiles. Both heterogeneity and temporality of these parameters also play a role in microbiological processes.

Geophysical methods can provide insight into soil property parameters in the High Arctic. Two established methods that are particularly applicable include electrical resistivity tomography (ERT) and surface NMR. Challenges in this setting include the remoteness of the study area, as well as the shallow depth of primary interest (0-2 m).

ERT measures electrical resistivity which is related to soil moisture and organic content of the media. ERT tomography is well-suited for shallow investigations pertinent to the application. Recent advances in semi-permanent installations of time-lapse ERT instrumentation enable processes to be monitored on daily, seasonal, and multi-year timescales. While ERT methods provide a powerful means by which to monitor subsurface processes, the link between soil moisture and electrical conductivity is empirical and requires calibration.

Surface NMR (sNMR) is a unique geophysical method that relies on the inherent nuclear magnetisation of liquid-phase water in the subsurface. As a result, sNMR measurements can provide a direct measure of water content which can be used to calibrate an ERT installation. Surface NMR has been used successfully in the Arctic previously where the remoteness and high magnetic field intensity contribute to generally favourable conditions (Keating et al., 2018). The shallow depth of investigation of sNMR for soil evolution monitoring in this application is challenging as most instruments are designed around deeper targets. As such, an open research question was how successful small loop NMR would be in the Arctic.

This abstract presents preliminary findings of a long term ERT installation and shallow small loop sNMR soundings in the forefield of the Midtre Lovénbreen glacier near Ny-Ålesund, Svalbard. The data were collected as part of SUN-SPEARS, an interdisciplinary and international project integrating geophysical and microbiological data in order to better understand soil development following glacial retreat. The sites represent a chronosequence with longer-exposed sediments present further from the actively retreating snout of the glacier. The data were collected in July 2021 and findings will be incorporated in biological modelling (e.g. Bradley et al., 2017) in later stages of the project.

METHODS

Two ERT systems (BGS-designed, known as PRIME) were installed in the forefield of the Midtre Lovénbreen glacier. Site 1 was near the snout of the glacier (as of July 2021) and Site 2

was found approximately 800 m from the snout (Fig. 1). Surface NMR data were collected at Sites 1 and 2 as well as in between at Site 1.5. The sNMR data were collected over the ERT arrays (Fig. 2) although the volume of investigation varies between the two methods.

The SUN-SPEARS project will also collect subsurface temperature data from buried sensors recorded on a Campbell Scientific data logger and tower installation. These data will also be used to calibrate the ERT data at later stages in the project. The installation of temperature sensors included the auguring of test holes at Sites 1 and 2. Site 1 was dominated by fine glacial sediment, but also included some large cobbles and boulders; the water table was at approximately 75 cm. Site 2 contained more cobbles and boulders than Site 1, especially below ~0.7 m. Auguring did not encounter the water table at Site 2.

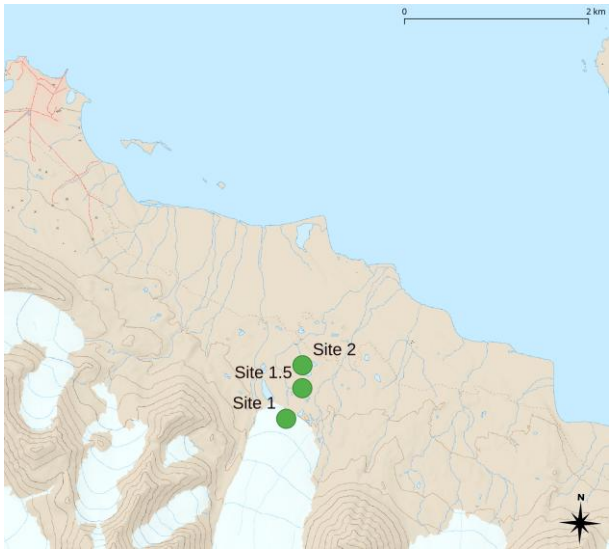

Figure 1. Location of field sites in front of the Midtre Lovénbreen glacier. Sites 1 and 2 include a full PRIME installation, sNMR data were also acquired in between Sites 1 and 2, at Site 1.5. The town of Ny-Ålesund is in the NW corner of the map.

Electrical Resistivity Tomography. Two semi-permanent ERT installations were installed at Sites 1 and 2 in this study. The PRIME system was developed by the British Geological Survey (Holmes et al., 2020) and included solar panels and wind turbines to provide power through the Arctic winter. Each PRIME installation includes 96 electrodes at 60 cm line and electrode separation. A rectangular configuration was adopted with 4 elongated electrode lines of 24 electrodes each. Each PRIME grid therefore covers a 2.4 x 14.4 m rectangular area. The PRIME installations are semi-autonomous and collect a suite of data regularly. Different electrode survey configurations are collected including dipole-dipole and multiple-gradient. The data in this manuscript were processed using Res3DInvX64 (https://aarhusgeosoftware.dk/res3dinv).

Surface NMR. The MRS-MIDI II surface NMR instrument manufactured by Radic Research was used in this study. It is a relatively low power instrument transmitting approximately 30 A peak current at the maximum pulse moment. The MIDI II is relatively lightweight and fits into a backpack for transport to and from the fieldsite. The MIDI II was connected to a lightweight 24 V Li-ION power supply. The transmitter (single turn) and receiver (12 turn) wires were both 40 m long. A combination of coincident single turn 6.4 m circular and 10 m square loops were used. Single pulse FID datasets were collected with 24 evenly spaced pulse moments. In most cases 64 stacks were acquired.

The inducing field was estimated from the International Geomagnetic Reference Field (IGRF) model (accessed through http://noaa.gov). For the survey dates the inclination and declination of B_0 was approximately 82° and 7.6°, respectively. The IGRF field intensity was estimated to be 55 062 nT, corresponding to a Larmor frequency of 2 344 Hz. In the field Larmor frequencies from 2 336–2 342 Hz were observed. The sNMR data were processed and inverted using the Akvo sNMR workbench (akvo.lemmasoftware.org).

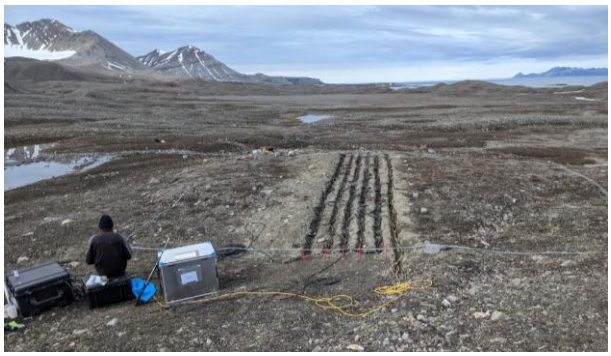

Figure 2. Example of survey configuration at Site 2. The sNMR loop (grey wire) encompassed a larger area than the ERT array (trenches).

RESULTS

Preliminary results from Sites 1 and 2 are discussed below. In both cases the ERT results are based on the inversion of a single dataset (not time lapsed). The NMR inversions are based on a QT-style inversion with a depth of investigation (DOI) derived from a point-spread function. No DOI analysis was performed on the ERT inversions at this stage in the project.

Site 1. The PRIME inversion at Site 1 indicates a more conductive top 0.5 m of soil on the side of the ERT array nearest the glacier (Fig. 3). A sNMR loop was set up on the edge of the array biased towards the conductive edge of the ERT inversion (running from approximately 8 m to 18 m using the same grid). The sNMR data was good quality with a noise floor estimate of 2.7 nV (Fig. 4). The signal was not particularly high, but apparent T_2^* decays were in the range of 200 ms. Inversion of the sNMR data was consistent with increased water content at approximately 0.6 m depth. The water content pinches out near 2 m but increases again at a depth of about 5 m (Fig. 5).

The combination of relatively long decays with low water content may appear paradoxical at first consideration. However, this is consistent with liquid phase water in permafrost. Permafrost often contains substantial quantities of liquid phase water. Most conceptualizations of permafrost are consistent with ice found around the edges of pores with a nucleus of liquid phase water. Since ice has a low surface relaxivity, long NMR decays are often observed in these settings (Kass et al., 2017). The deeper water (6-7 m) could also be another layer of fine sediments below cobbles, similar to Site 2.

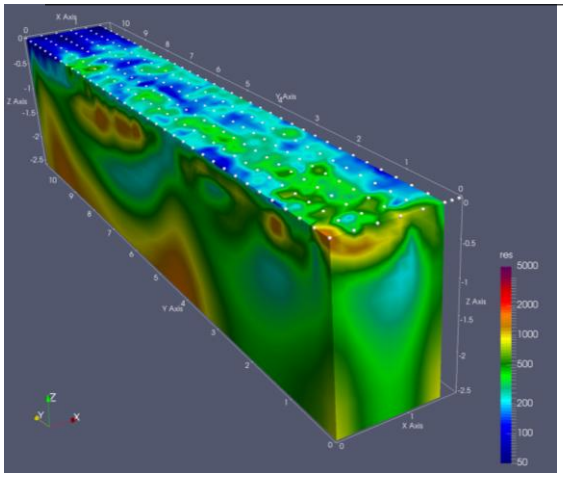

Figure 3. An inversion of PRIME data collected at Site 1. The 'y'-axis runs in the same direction as the glacier and most of the contrast is expected along this line. The area nearest the glacier has higher conductivity in the shallow subsurface.

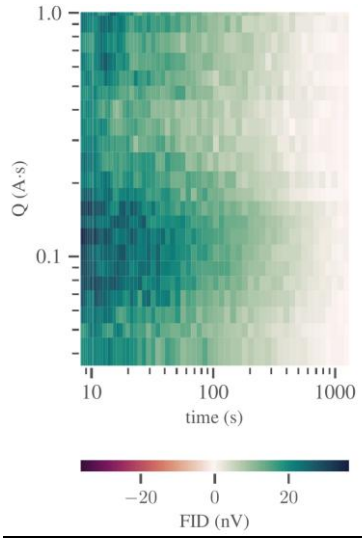

Figure 4. Surface NMR data collected at Site 1. The noise level appeared uniform and was estimated at 2.7 nV.

Site 2. The ERT inversion at Site 2 (Fig. 6) indicates a more homogenous setting along the survey direction (less lateral trend than at Site 1). The ERT data indicate resistive sediments below approximately 70 cm. The auguring of temperature sensor boreholes is consistent with a zone of large cobbles at this depth. The sNMR data collected at Site 2 had a similar noise floor to Site 1 (2.87 nT) but a lower level of NMR signal and shorter decays (Fig. 7). As a result, the S:N at site 2 was lower than Site 1. Less variation in water content with pulse moment was shown in the sNMR data at Site 2 compared to Site 1. Inversion of this dataset yielded a fairly uniform water content model between 0.01 and 0.03 m^3/m^3 with faster T_2^* decay rates than Site 1 (Fig. 8).

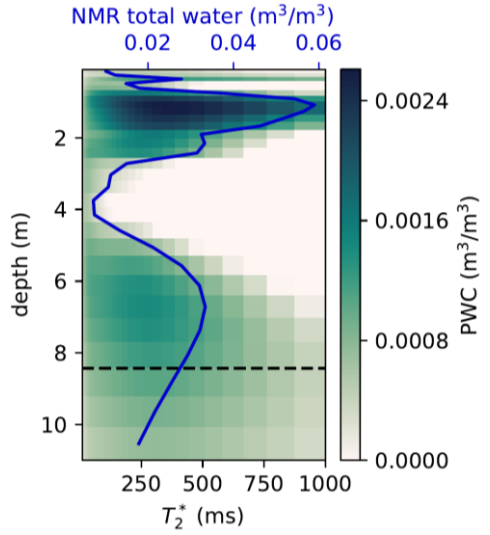

Figure 5. Inversion of sNMR data at Site 1, the black dashed line represents a DOI based on point spread analysis. Total water content is shown in blue.

Interpretation of the geophysical data at Site 2 is consistent with less overall water availability. The large cobbles at Site 2 will have less pore space than the finer sediments at Site 1 and more significantly will contain fewer small pores with the capillary pressure needed to retain water in the presence of drainage forces. For these reasons, it is postulated that the water availability for microorganisms at Site 2 is seasonally dependent on the availability of snowmelt.

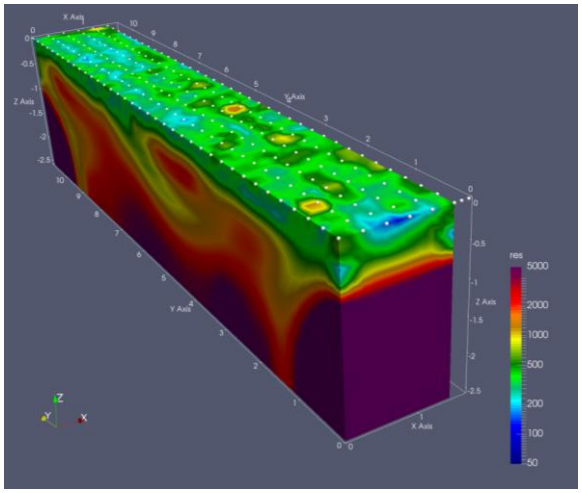

Figure 6. The PRIME inversion at Site 2 indicates more electrically conductive materials down to about 0.5 m at which point a more resistive medium is encountered.

Contrasting Site 1 and Site 2 suggests that water availability for microorganisms is spatially and temporally variable. Sites near the snout of the glacier have an abundant source of water during melt season. Locations even a short distance away from the toe may be significantly drier during summer months.

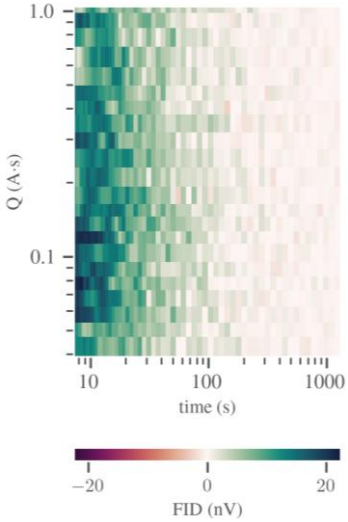

Figure 7. The sNMR data at Site 2 had an estimated noise level of 2.87 nT but lower overall NMR signal amplitude than Site 1.

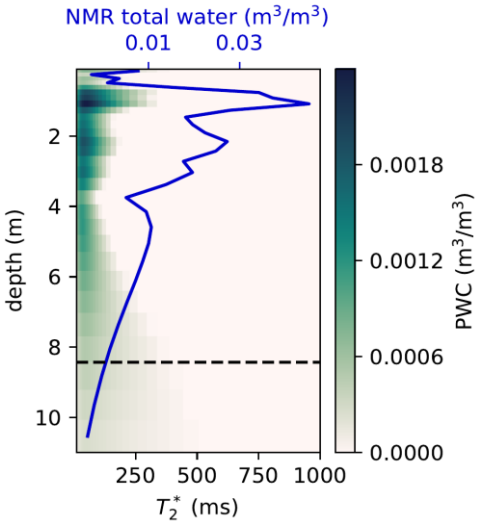

Figure 8. Surface NMR inversion at Site 2. The recovered water content model at Site 2 is much more uniform with depth and has faster decays than Site 1.

CONCLUSIONS

The current rapid retreat of Arctic glaciers is resulting in large swaths of land undergoing transformation from recently-exposed glacial sediments to tundra. Biological activity contributes to soil formation, however the biota requires resources (including water availability) in order to become established in these soils. Geophysical surveys can provide valuable information about material properties and water availability and can therefore increase the understanding of soil evolution in this setting.

Preliminary results from an ERT monitoring array installation confirm that electrical resistivity provides a useful proxy for subsurface properties. Surface NMR provides a powerful tool for calibration and interpretation of ERT data and increases the value of the ERT data. Small loop sNMR can be an effective tool in the Arctic where ambient noise levels are low and the technique is uniquely capable of detecting shallow water content.

The installation of long-term ERT monitoring equipment will be valuable in providing a picture of how conditions change temporally and spatially in this dynamic setting. Continued monitoring at Sites 1 and 2 in the Midre Lovénbreen glacier with intermittent sNMR support data will provide a glimpse at the seasonal processes which contribute to microorganism ecology in this unique environment.

ACKNOWLEDGEMENTS

Sensors UNder snow Seasonal Processes in the evolution of ARctic Soils (SUN-SPEARS) is funded by a joint award between the US National Science Foundation (NSF award numbers 2015329 & 1935689) and United Kingdom Research & Innovation (UKRI) through the National Environment Research Council (NERC), award numbers NE/T010967/1 and NE/T010568/1. Additional support was provided by the British Antarctic Survey (BAS) including use of Arctic Research Station facilities in Ny-Ålesund as well as COVID-19 contingency funding, and the Alexander von Humboldt Foundation (to JAB). We are grateful to the Sverdrup Research Station (Norwegian Polar Institute), Michael Jarzin, Justin Byington, and Juan Carlos Trejos Espeleta for field assistance. The authors thank the Department of Geophysics at the Colorado School of Mines for the lease of the MRS-MIDI II.

REFERENCES

Botnen, S. S., S. Mundra, H. Kauserud, and P. B. Eidesen, 2020, Glacier retreat in the High Arctic: opportunity or threat for ectomycorrhizal diversity? FEMS Microbiology Ecology, 96.

Bradley, J. A., A. M. Anesio, and S. Arndt, 2017, Microbial and Biogeochemical Dynamics in Glacier Forefields Are Sensitive to Century-Scale Climate and Anthropogenic Change: Frontiers of Earth Science in China, 5, 26.

Bradley, J. A., A. M. Anesio, J. S. Singarayer, M. R. Heath, and S. Arndt, 2015, SHIMMER (1.0): a novel mathematical model for microbial and biogeochemical dynamics in glacier forefield ecosystems: Geoscientific Model Development, 8, 3441–3470.

Holmes, J., J. Chambers, P. Meldrum, P. Wilkinson, J. Boyd, P. Williamson, D. Huntley, K. Sattler, D. Elwood, V. Sivakumar, H. Reeves, and S. Donohue, 2020, Four- dimensional electrical resistivity tomography for continuous, near- real- time monitoring of a landslide affecting transport infrastructure in British Columbia, Canada: Near Surface Geophysics, 18, 337–351.

Kass, M. A., T. P. Irons, B. J. Minsley, N. J. Pastick, D. Brown, and B. K. Wylie, 2017, In situ nuclear magnetic resonance response of permafrost and active layer soil in boreal and tundra ecosystems: The Cryosphere, 11, 2943–2955.

Keating, K., A. Binley, V. Bense, R. L. Van Dam, and H. H. Christiansen, 2018, Combined geophysical measurements provide evidence for unfrozen water in permafrost in the Adventdalen valley in Svalbard: Geophysical Research Letters, 45, 7606–761

Characterization of the groundwater resource of the Sandricourt domain (Oise, France) using Magnetic Resonance Sounding (MRS) and Electrical Resistivity Tomography (ERT)

[1*]Pascale LUTZ [2]Michaël GOUJON [2]Pierre-Evan MEURANT [1]Lahcen ZOUHRI
[2]Alexandre LE BOUCH [2]Ulric NAGNONHOUM [2]Hugo RAIN

[1] AGHYLE, Institut Polytechnique UniLaSalle Beauvais, SFR Condorcet FR CNRS 3417, 19 rue Pierre Waguet, BP 30313, F-60026 Beauvais Cedex, France
[2] Institut Polytechnique UniLaSalle Beauvais, Département Géosciences, 19 rue Pierre Waguet, BP 30313, F-60026 Beauvais Cedex, France, France
**Correspondence:* pascale.lutz@unilasalle.fr

SUMMARY

The domain of Sandricourt (castle, crops, hunting reserve) is supplied with water thanks to pumping into the Cretaceous chalk watertable. However, the latter has been impacted in nitrates. One solution is the realization of a catchment in the Cuisian-Lutetian aquifer located in the cuesta overlooking the estate.

The objective of this study, carried out by the UniLaSalle Institute, was to identify and quantify the water resources of these formations, with a view to future exploitation.

Two geophysical methods were used in addition to bibliographic and field studies on the geology and hydrogeology: Electrical Resistivity Tomography (ERT) and Magnetic Resonance Sounding (MRS). The heterogeneity of the hydrogeological system is characterized by permeability values which vary with depth and range from 2.10^{-7}m/s to $1.8.10^{-3}$ m/s. The cuisian's investigations lead to significant transmissivity values about $1.1.10^{-2}m^2/s$.

Key words: MRS, ERT, groundwater resource, Sandricourt, chalk, water content, permeability

INTRODUCTION

The domain of Sandricourt, located in the department of Oise (60, France) (Figure 1), consists of a castle, farms and wooded area. It is located south of the anticline of the "Pays de Bray". The estate has a borehole located in the Cretaceous chalk groundwater to feed the agricultural activities and residences of the estate. However, this resource is impacted by high concentrations of nitrates (> 50 mg/L: potability threshold).

Hence the need to seek new groundwater resources, especially the implementation of a new borehole in the Cuisian-Lutetian in order to replace the currently one. However, is the Cuisian aquifer a sufficient resource?

To try to answer this problem, geological and hydrogeophysical investigations were conducted on the field by the Institut Polytechnique UniLaSalle Beauvais in 2018-2019. This multidisciplinary approach consists in: (i) geology field observations, (ii) hydrogeological measurements, (iii) Electrical Resistivity Tomography (ERT) and (iv) Magnetic Resonance Sounding (MRS).

Figure 1. Location of Sandricourt (Oise, France).

HYDROGEOLOGICAL SETTINGS

Thanks to the geological knowledge and the presence of boreholes nearby, a lithostratigraphic column was realized in order to give more information about principal aquifers in the region (Figure 2). The lithological formation of interest for a new borehole is the Cuisian sands.

With the aim to qualify the Cuisian aquifer, manual flow measurements were performed from October 2018 to March 2019 at a source located on the domain (Le Bouch et al. 2019). The values, between 0.9 and 1.7 m3/h, show a relatively low flow rate. This can be explained by a southerly flow direction within the Cuisian aquifer (Figure 3).

ELECTRICAL RESISTIVITY TOMOGRAPHY

Electrical Resistivity Tomography (ERT) measurements were acquired on the domain of Sandricourt to precise the lithological boundaries. A pre-feasibility study was held in June 2018, followed by complementary measurements from

September 2018 till March 2019. A total of 13 ERT were realized (Figure 4). These were undertaken with a multi-electrode 2D device (ABEM TERRAMETER SAS 4000) using two type of array: (i) gradient to obtain both high resolution and medium depth (45m depth for a 5m electrode spacing) and (ii) pole-dipole to increase the investigation depth (maximum of 90m depth).

The apparent resistivity data were inverted using the standart code RES2DINV (Loke and Barker, 1996; Loke, 2003). The resistivity sections have been interpreted taking account to the lithostratigraphic column (Figure 2), and the usual geological resistivity values (Astier, 1971). These results allow to precise the boundaries of the different geological formations.

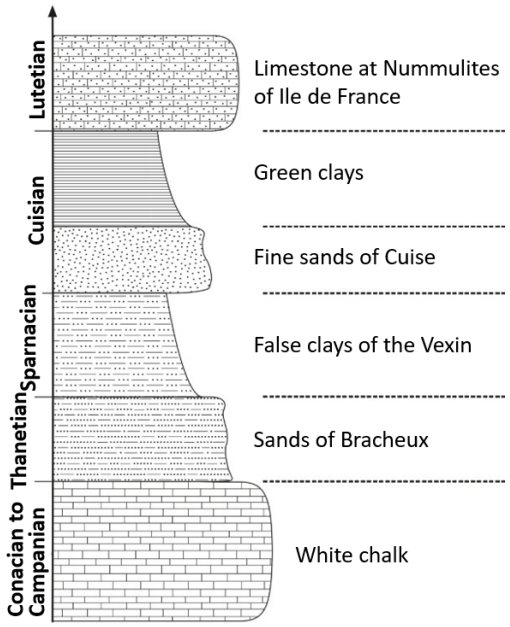

Figure 2. Simplified lithostratigraphic column of the Sandricourt domain (Le Bouch et al. 2019).

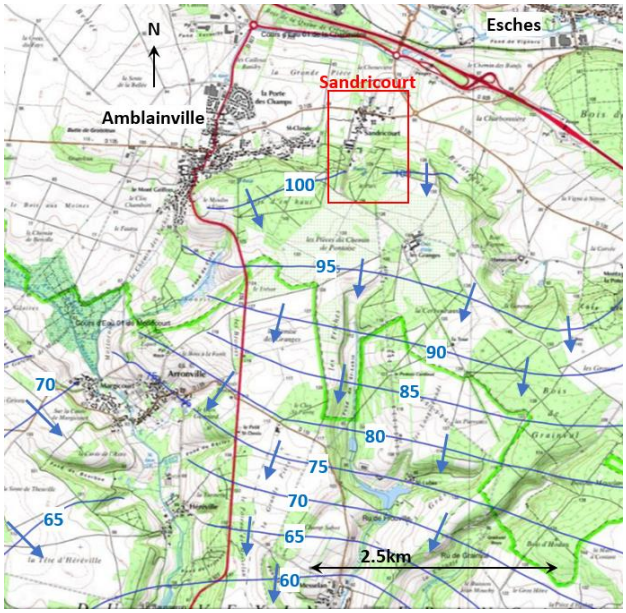

Figure 3. Groundwater flow of the Cuisian aquifer (Sandricourt, 2014) (BRGM-SIGES Seine Normandie, 2019).

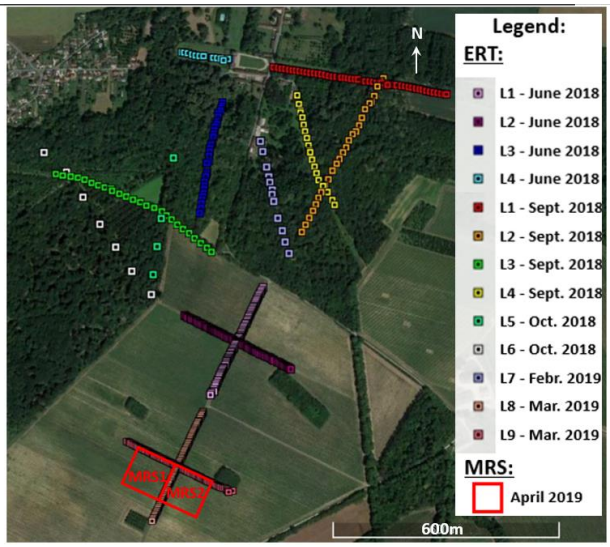

Figure 4. Location of the 13 ERT and the 2 MRS on the domain of Sandricourt.

An example of result is presented Figure 5, concerning the L7 ERT, located near the currently borehole. According to this resistivity model, the thickness of the Cuisian sands is estimated at about 20-30m.

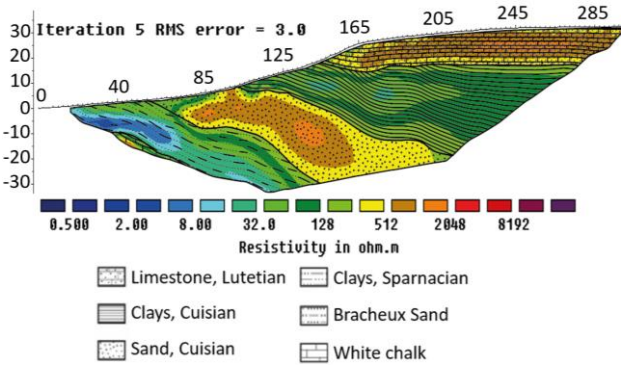

Figure 5. Line 7 resistivity model and its geological interpretation (February 2019).

MAGNETIC RESONANCE SOUNDING

A MRS campaign was conducted in April 2019 to precise the hydrogeological parameters on the domain of Sandricourt. In order to undertake the MRS measurements in suitable conditions in terms of electromagnetic noise and magnetic field variations, preliminary measurements were realized as advised (IRIS Instruments, 2010). The devices used for are respectively the 6m diameter "noise loop" of Iris Instruments, and the G856AX magnetometer of Geometricx.

The resulting electromagnetic noise level (Figure 5) allowed us to choose suitable locations for two soundings using a 100m diameter squared loop (noise level less than 0.1µV). Just before setting up the MRS survey, the magnetic field was measured on the surface loop to verify that its variations are less than ± 20nT and estimate the Larmor frequency from its mean value (2055Hz, corresponding to a magnetic field of 48267nT).

The NumisPoly device from Iris Instruments was used (Prodiviner software), with the double pulse option, 16 pulses, a pulse duration of 40ms and a recording time of 240ms, a

stack under noise level of 80 and a noise cutoff of about 3000-5000nV. As the noise level is under 0.1µV (Figure 6) and no power line is nearby the MRS site, no filter during the measurements was applied.

Measurements were interpreted with Samovar V6.6 (Legchenko et al., 2008) with a matrix considering the resistivity values from L9 ERT located next to the MRS (Figure 7, Table 1).

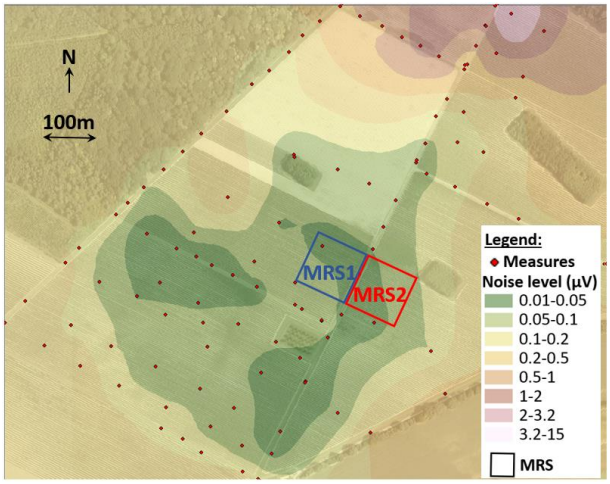

Figure 6. Map of the noise level and location of the two MRS (square, side=100m) on the domain of Sandricourt (blackcurrant crops) in April 2019.

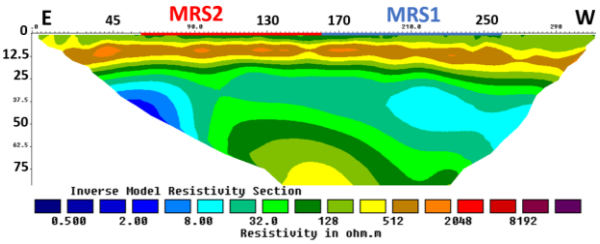

Figure 7. Line 9 resistivity model (PDP and gradient) allowing to determine the resistivity models for MRS1 and MRS2 (Table 1).

MRS1		MRS2	
Depth (m)	Resistivity (Ohm.m)	Depth (m)	Resistivity (Ohm.m)
0-7	190	0-7	190
7-22	700	7-22	700
22-30	100	22-35	100
30-50	10	35-60	160
>50	150	>60	150

Table 1. Resistivity models for MRS1' and MRS2' matrix.

This processing consists in applying:

(i) a running average filter;

(ii) the following regularization parameters: 500 for E and T_2*, 10 for T_1*;

(iii) a model of 30 layers;

(iv) an empirical coefficient of calibration coefficient C_p=3.5.10^{-8} (corresponding to the mean value deduced for the chalk in France from the calibration with pumping tests (Vouillamoz, 2003)).

Note that 2 tests were realized: applying or not a narrow 50Hz notch filter (notch band=3, filter correction, center fixed).

An example of results is presented in Figures 8,9 and 10 for MRS1 (without applying a narrow 50Hz notch filter).

The fitted sounding curve (Figure 8) shows an increase of the signal amplitude up to 600nV for a pulse of 2840A.ms, then a decrease. Its difference with the measures is generally correct (except for the maximum). The comparison of the measured signal with the stack noise reveals a correct quality of the data, with a stacked noise less than 100nV, except for a few points.

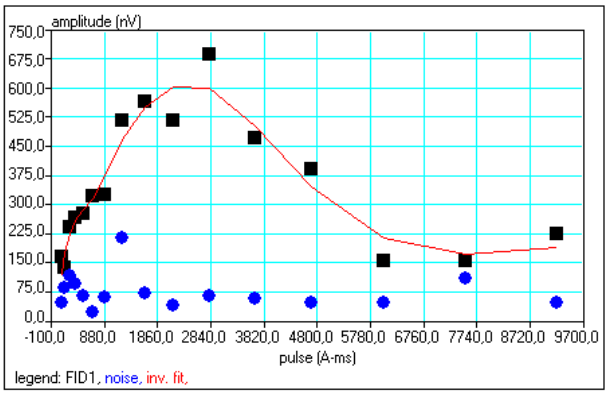

Figure 8. Results obtained for MRS1 without a narrow 50Hz notch filter. Souding curve (measured in black squares, fitted in red line) and stacked noise (blue dot).

Figure 9a shows the curve of the water content versus depth up to a 95m. It reveals two increases of significant value:

- at about 5m, with a maximum of 12.5%;
- from 18m to 38m, with a maximum of 20% at about 30m.

Moreover, it shows a significant increase of the relaxation time (T1*) between 28m and 38m, with a maximum of 2000ms at 35m, whereas this parameter is about 50ms at other depths. This was interpreted by Samovar in terms of permeability (K) as the following (figure 10a):

- from 1 to 5m: K is about 8.10^{-7}m/s;
- from 20 to 28 m: 4.10^{-7}m/s <K< 1.8.10^{-6}m/s;
- between 30 and 40 m: K> 2.10^{-4}m/s, with a maximum of 1.8.10^{-3}m/s at 35m.

It's of great interest to compare these results with the log of the drilling on the domain of Sandricourt (Figure 9b). It reveals that the first water content increase at about 5m could be explained by the Lutetian limestones, with a water content of about 11% and a permeability of about 8.10^{-7}m/s.
Moreover, the second water content increase should correspond to:

- a transition zone between clays and the Cuisian sand with a low permeability from 18 to 28m (less than 1.8.10^{-6}m/s);
- the Cuisian sand from 30 to 40m with a permeability between 2.10^{-4}m/s and 1.8.10^{-3}m/s.

Concerning the transmissivity (T) (Figure 10b), we can observe:

- weak values from the surface to 20m:
  - from 1 to 4m: T< 4.10^{-6}m^2/s;
  - from 6m to 20m: T is about 4.8.10^{-6}m^2/s.
- a significant value of 1.1.10^{-2}m^2/s for depth more than 30m.

The transmissivity of the Cuisian sands is thus estimated at about 1.1.10^{-2}m^2/s.

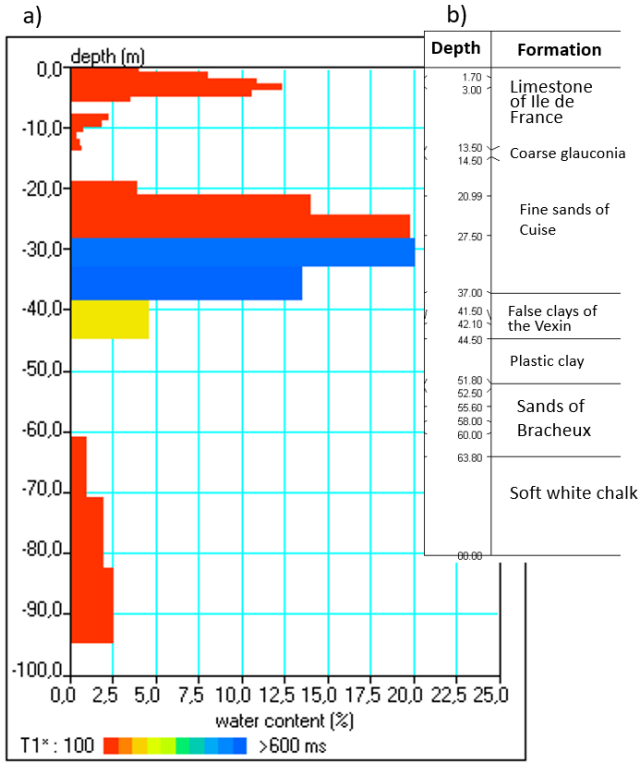

Figure 9. a) Results obtained for MRS1 without a narrow 50Hz notch filter. Water content (%) versus depth (m). b) Drilling log on the domain of Sandricourt.

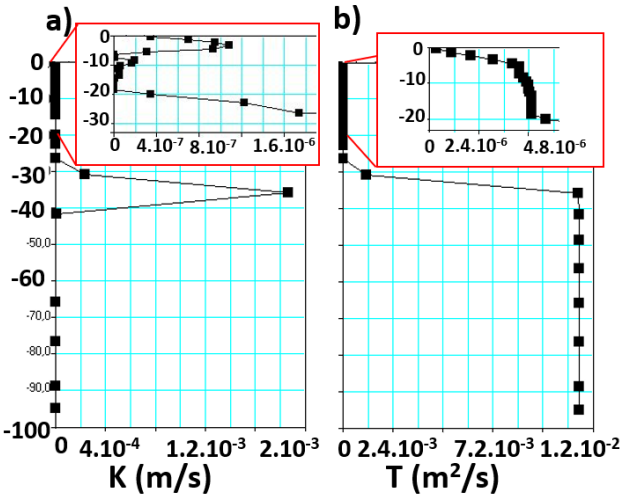

Figure 10. Results obtained for MRS1 without a narrow 50Hz notch filter. a) Permeability (K (m/s)) versus depth (m). b) Transmissivity (T (m^2/s)) versus depth (m).

CONCLUSIONS

This multidisciplinary approach shows the interest of ERT and MRS for hydrogeolocical study. The measurements allowed to estimate the water content, the permability and transmissivity of the Cuisian sand on the domain of Sandricourt. However it should be completed by addional hydrogeophysical measurements and pumping tests to better estimate the potential of the Cuisian sands to replace the currently borehole in the Cretaceous chalk watertable.

ACKNOWLEDGMENTS

The authors wish to thank the domain of Sandricourt for their agreement to carry out the measurements on the field. The authors wish to thank the FEDER organization for the financing of the Iris Instruments equipment. The authors wish to thank the region Picardie for the financing of the ABEM ERT device. The authors express their appreciation to the students of UniLaSalle for their assistance on the field during the measurements.

REFERENCES

Astier, J.L. 1971. Géophysique appliquée à l'hydro-géologie. Masson. 277 p.

BRGM – SIGES. 2019. SIGES Seine-Normandie : Espace cartographique. Accessed May 25, 2019. available at http://sigessn.brgm.fr/?page=carto.

IRIS Instruments. 2010. Numis Poly - Multi-chanel MRS system - Magnetic resonance system – User's manual.

Le Bouch, A., Nagnonhoun U., Rain U. 2019. Etude et caractérisation de la ressource en eaux souterraines au droit du domaine de Sandricourt. Mémoire d'Initiation à la Recherche, Institut Polytechnique UniLaSalle.

Legchenko, A., Ezerski, A., Girard, J.F., Baltassat, J.M., Boucher, M., Camerlynk, C., Al-Zoubi, A. 2008. Interpretation of magnetic resonance soundings in rocks with high electrical conductivity. Journal of Applied Geophysics, 66, p.118-127.

Loke, M.H. & Barker, R.D. 1996. Rapid least-squares inversion of apparent resistivity pseudosections by a Quasi-Newton method. Geophys. Prospect, 44: 131–152.

Loke, M.H. 2003. RES2DINV Rapid 2-D Resistivity and IP inversion using the least squares method. Manual, Geotomo Software, Penang, Malaysia.

Vouillamoz, J.M. 2003. La caractérisation des aquifères par une méthode non invasive: les sondages par Résonance Magnétique Protonique. PhD Thesis, University of Paris XI, Orsay, France

Mitigation of powerline noise in surface NMR data: Estimation of the fundamental frequency using convolutional neural networks

[1,3]Jakob Juul Larsen, [1]Matthew P. Griffiths, [2,3]Denys Grombacher and [2]Muhammad Rizwan Asif

[1]Department of Electrical and Computer Engineering
Aarhus University
8200 Aarhus N
Denmark
Email: jjl@ece.au.dk

[2]Hydrogeophysics Group
Department of Geoscience
Aarhus University
8000 Aarhus C
Denmark

[3]Aarhus University Centre for Water Technology
Aarhus University
8000 Aarhus C
Denmark

SUMMARY

Model-based subtraction of powerline harmonic noise is often applied in processing of surface NMR data, as it is an efficient method for removing this particular component of noise. One drawback of model-based subtraction is its computational cost, as the determination of the model parameters requires solving a least-square problem multiple times for each segment of data. Here we demonstrate that a convolutional neural network can directly estimate the powerline frequency from noisy data. We train the convolutional neural network using supervised learning on a data set composed of white noise and synthetic powerline noise. Numerical experiments shows that the performance is on par with state-of-the-art methods in terms of accuracy and can be significantly faster. We demonstrate the generalization capabilities of the network using real-world surface NMR data sets.

Key words: Surface NMR, signal processing, powerline noise, convolutional neural network, Fourier analysis, scientific machine learning.

INTRODUCTION

Powerlines and other electrical installations are common sources of noise in surface NMR measurements. This noise appears as sinusoidal signals at the fundamental frequency of the power grid (50 Hz or 60 Hz) and at integer multiples of the fundamental frequency. The noise can be orders of magnitude larger than the surface NMR signal and it is normally required to suppress this noise to achieve adequate signal-to-noise ratios.

State-of-the-art powerline noise mitigation methods include figure 8 coils, where a specialized coil layout is used to cancel the electromagnetic field from a powerline running parallel to the coil (Girard et al., 2020), remote reference noise cancellation, where data from one or multiple reference coils are used to estimate and subtract noise from the surface NMR data (Müller-Petke et al., 2016), and subtraction-based methods, where a model of the powerline noise is estimated and subtracted from the recorded data (Larsen et al., 2014, Liu et al. 2018, Kremer et al. 2019).

The subtraction-based approach has been highly successful as it deals with one specific noise source and has no requirements for carefully tailored coil layout or additional receiver coils. However, one drawback of the subtraction-based method is it computational cost as the determination of the model parameters is inherently a nonlinear problem.

In this paper, we demonstrate how scientific machine learning methods can improve upon the state-of-the-art methods for model-based subtraction of powerline noise. We demonstrate that a convolution neural network can predict the fundamental powerline frequency from a segment of data and we show that this new method can be faster than standard methods.

METHODS

The sampled signal, x(n), recorded by a surface NMR instrument can be decomposed as

$$x(n) = s(n) + h(n) + v(n) \quad (1)$$

where s(n) is the surface NMR signal, h(n) is the powerline noise, and v(n) accounts for other noise contributions. Assuming stationarity, the powerline noise is modelled as

$$h(n) = \sum_m A_m cos\big(m\omega_p n + \phi_m\big) \quad (2)$$

where $\omega_p = 2\pi f_p / f_s$ is the normalized angular powerline frequency, A_m is the amplitude and ϕ_m is the phase of the m'th harmonic component. The powerline model can be partially linearized by a trigonometric rewrite i.e.

$$h(n) = \sum_m (\alpha_m cos\big(m\omega_p n\big) + \beta_m\, cos\big(m\omega_p n\big)) \quad (3)$$

which is a linear equation if ω_p is fixed. A common approach is therefore to repeatedly minimize the least-squares problem $\|x(n) - \hat{h}(n)\|^2$ over a range of assumed powerline frequencies and determine the frequency, which leads to the smallest residual. The search for the optimum frequency can be done with brute force or take advantage of more advanced algorithms (Larsen et al. 2014, Wang et al., 2018, Kjær-Rasmussen et al. 2021).

A different approach to determine the powerline frequency is to use a convolutional neural network to directly predict the frequency from a segment of data. For this purpose, we use the convolutional neural network architecture shown in Fig. 1.

#	Operation layer	Activations	Learnables	
1	Image input layer 6250×1×1 image	6250×1×1	-	
2	Convolution layer 64 3125×1×1 convolutions with stride 1 and no padding	3126×1×1	Weights	3125×1×1×64
			Bias	1×1×64
3	Batch normalization layer Batch normalization with 64 channels	3126×1×1	Offset	1×1×64
			Scale	1×1×64
4	ReLU layer	3126×1×1	-	
5	Fully connected layer 64 fully connected layer	1×1×64	Weights	64×200064
			Bias	64 × 1
6	Batch normalization layer Batch normalization with 64 channels	1×1×64	Offset	1×1×64
			Scale	1×1×64
7	ReLU layer	1×1×64	-	
8	Dropout layer 25% dropout	1×1×64	-	
9	Fully connected layer 32 fully connected layer	1×1×32	Weights	32×64
			Bias	32×1
10	Batch normalization layer Batch normalization with 32 channels	1×1×32	Offset	1×1×32
			Scale	1×1×32
11	ReLU layer	1×1×32	-	
12	Dropout layer 25% dropout	1×1×32	-	
13	Fully connected layer 1 fully connected layer	1×1×1	Weights	1×32
			Bias	1×1

Figure 1: Overview of the architecture of the convolutional neural network.

The input to the network is a 6250 samples long time series. This length corresponds to 200 ms of data at a sampling rate of 31250 Hz. The training of the network is done with supervised learning using a set containing 1 million time series of synthetic data on two NVIDIA GeForce RTX2080TI GPUs. The synthetic data are comprised of powerline noise embedded in white noise. The white noise and the powerline noise is randomly generated for each realization. For each realization, the powerline frequency is a random number selected uniformly between 49.9 and 50.1 Hz. Each powerline component has a random phase between 0 and 2π and a random amplitude.

RESULTS

In Fig. 2, we show a comparison of the CNN-based and the standard least-squares method ability to estimate the powerline frequency on 1 s test segments. For the least-squares method, we use a brute-force grid search with a 1 mHz resolution, which leads to a non-biased uniform error distribution with a maximum error of 0.5 mHz with the exception of a few outliers. With the CNN-based method, the 1 s segment is divided into five 200 ms segments. A powerline frequency is predicted for each segment and we take the mean of the five predictions as the estimate of powerline frequency. The error distribution of the CNN-based method is also unbiased. The vast majority of frequency errors are well within 1 mHz and just a few outliers exceeding 1 mHz is obtained. As a rule of thumb, the frequency should be determined to within approximately 1 mHz to ensure good powerline noise modelling.

Figure 3 provides an example of the performance on a 1 s synthetic time series similar to the training data. Figure 3(a,e) shows the noisy time series and the corresponding power spectrum. The next row shows the result when the powerline noise is modelled and subtracted at the true frequency. The two bottom rows shows the result after grid search and a subsequent parabolic fit around the minimum to determine the optimum frequency and a CNN based prediction computed as the mean of five predictions using five subsequent 200 ms segments. In both cases, the prediction is well within 1 mHz of the true value and high-performance noise cancellation is obtained.

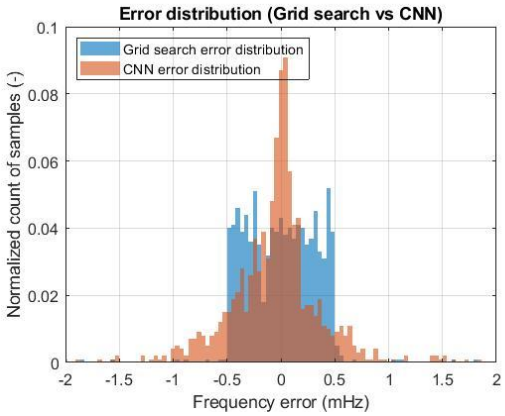

Figure 2: Frequency error distributions using either the least-squares approach with a 1 mHz resolution or the CNN-based approach.

In Fig. 4, we present an example using noise-only data recorded with the Apsu instrument (Larsen et al., 2020). The two methods give the same estimate for the powerline frequency within 0.5 mHz and we observe that both methods looks to near identical powerline noise subtraction results.

Our speed measurements show that it takes about 0.17 s on a Intel Xeon Gold 6132 CPU with a 2.6 GHz clock speed to predict the powerline frequency in a single 200 ms segment. On the same setup, it takes about 0.14 s to solve the least-squares problem for a 1 s segment on the same hardware. As multiple solves of the least-squares problem are necessary to determine the optimum frequency, the CNN-based approach will in many cases be the faster option.

Initial numerical experiments with the CNN-based method, where the data used for prediction of the powerline frequency also contains an NMR signal, has not revealed any noticeable shortcomings of the method or sensitivity to the NMR signal. However, further investigations are necessary before we can draw firm conclusions.

CONCLUSIONS

A precise determination of the fundamental powerline frequency in surface NMR data is necessary for efficient model-based subtraction. Well-established methods are available for this purpose, but they suffer from high numerical cost as a least-squares problem must be solved many times over. We have demonstrated that a convolutional neural network can be trained with synthetic data and used to directly give high accuracy predictions of the powerline frequency from short segments of data.

ACKNOWLEDGMENTS

This work is supported by Independent Research Fund Denmark and the Villum Foundation.

REFERENCES

Girard, J. F., Jodry, C. & Matthey, P.D. 2020. On-site characterization of the spatio-temporal structure of the noise for MRS measurements using a pair of eight-shape loops. Journal of Applied Geophysics, 178, p.104075.

Kjær-Rasmussen, A. Griffiths, M. P., Grombacher, D. & Larsen, J. J. 2021. Fast removal of powerline harmonic noise from surface NMR data sets using a projection-based approach on graphical processing units. IEEE Geoscience and Remote Sensing Letters, in revision.

Kremer, T., Larsen, J. J. & Nguyen, F. 2019. Processing harmonic EM noise with multiple or unstable frequency content in surface NMR surveys. Geophysical Journal International, 219, p.753-775.

Liu, L., Grombacher, D., Auken, E. & Larsen, J. J. 2018. Removal of co-frequency powerline harmonics from multichannel surface NMR data. IEEE Geoscience and Remote Sensing Letters, 15(1), p.53-57.

Larsen, J. J., Liu, L., Grombacher, D. Osterman, G. & Auken, E. 2020. Apsu – A new compact surface NMR instrument for groundwater measurements GEOPHYSICS 85(2), p. JM1-JM11.

Larsen, J. J., Dalgaard, E. & Auken, E. 2014. Noise cancelling of MRS signals combining model-based removal of powerline harmonics and multichannel Wiener filtering. Geophysical Journal International, 196(2), p.828-836.

Müller-Petke, M., Braun, M., Hertrich, M., Costabel, S., & Walbreck, J. 2016. MRSmatlab – A software tool for processing, modeling, and inversion of magnetic resonance sounding data. GEOPHYSICS, 81(4), p.WB9-WB21.

Wang, Q., Jiang, C. & Müller-Petke, M. 2018. An alternative approach to handling co-frequency harmonics in surface nuclear magnetic resonance data. Geophysical Journal International, 215(1), p.1962-1973.

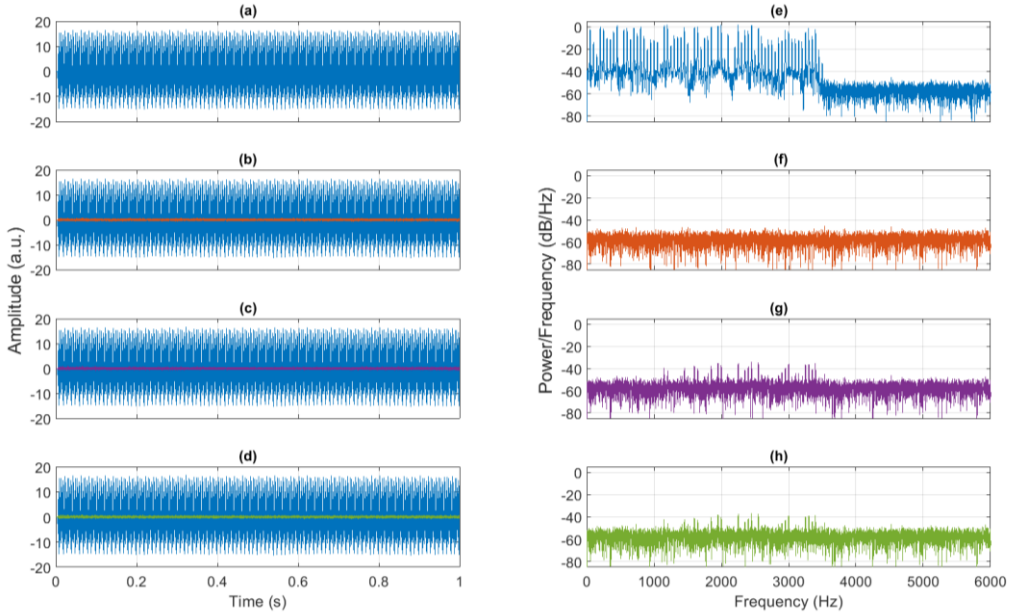

Figure 3. Examples of powerline noise subtraction. (a, e) Time series and power spectrum of synthetic data composed of white noise and powerline noise. (b, f). Time series and power spectrum after model-based subtraction at the exact powerline frequency. (c,g) Time series and power spectrum after model-based subtraction at the powerline frequency estimated with the least-squares method. (d,h) Time series and power spectrum after model-based subtraction at the powerline frequency estimated with the CNN method.

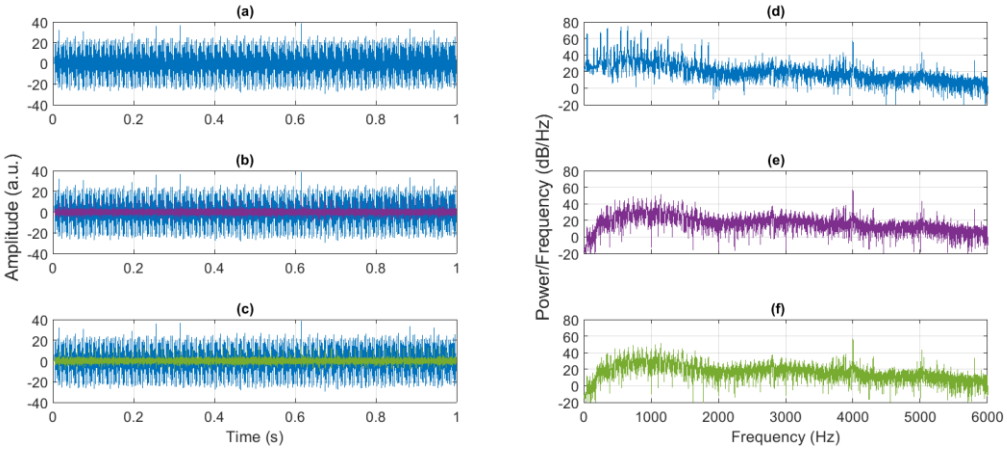

Figure 4. Examples of powerline noise subtraction on a noise-only data set. (a, d) Time series and power spectrum of raw data. (b, e) Time series and power spectrum after model-based subtraction at the powerline frequency estimated with the least-squares method. (c, f) Time series and power spectrum after model-based subtraction at the powerline frequency estimated with the CNN method.

Investigation on unsaturated water flow in karst limestone of the Beauce aquifer (France) using time-lapse MRS measurements

[1]Legchenko Anatoly, [2]Baltassat Jean-Michel, [3]Amroui Nadia, [4]Isch Arnaud, [5]Abbas Mohamad, [6]Ryckebush Clemence, [7]Deparis Jacques, [8]Azaroual Mohamed

[1] Univ. Grenoble Alps, IRD, IGE, Grenoble, France, E-mail: anatoli.legtchenko@ird

[2] BRGM, Orléans, France, E-mail: jm.baltassat@brgm.fr

[3] BRGM, Orléans, France, E-mail: n.amraoui@brgm.fr

[4] CNRS, ISTO, Orléans, France, E-mail: arnaud.isch@cnrs-orleans.fr

[5] CNRS, ISTO, Orléans, France, E-mail: mohamad.abbas@cnrs-orleans.fr

[6] BRGM, ISTO, Orléans, France, E-mail: c.ryckebusch@brgm.fr

[7] BRGM, Orléans, France, E-mail: j.deparis@brgm.fr

[8] BRGM, ISTO, CNRS, France, E-mail : mohamed.azaroual@cnrs-orleans.fr

SUMMARY

We show that time-lapse Magnetic Resonance Sounding (MRS) measurements allow recording seasonal variations of the water content in the unsaturated non-magnetic geological materials like chalk or limestone. Between 1999 and 2000, we carried out a one-year MRS monitoring of the water content in Villamblain test-pilot site. These data show seasonal variations of the water content in the unsaturated zone. Another one-year monitoring carried out in the same site between 2020 and 2021 allows comparison of two data sets separated by 21 years. We observe a remarkable correspondence between MRS data sets and the hydro-meteorological data.

Key words: MRS, time-lapse, unsaturated water flow, limestone, karst.

INTRODUCTION

Understanding of an unsaturated water flow is important for a sustainable management of water resources, estimation of aquifer recharge and elaboration of water protection measures. The geological heterogeneity of the subsurface is a major difficulty for accurate numerical modelling. The scale effect on the water flow is one of the problems to consider. For hydrogeology, measurements of the soil hydraulic properties can be carried out at the centimetric scale (soil samples or a narrow area around borehole body). For a large-scale mapping, non-invasively geophysical methods are often used (Rubin and Hubbard, 2006). Among them, the Ground Penetrating Radar (GPR) and the Electrical Resistivity Tomography (ERT) are the most popular. These methods allow delineation of different geological patterns and exploit correlations between the electrical and the hydraulic properties of the subsurface. However, the water content is only one of the soil physical properties having an effect on the parameters measured with these methods and interpretation in term of water content is not straightforward. MRS is a surface geophysical method selectively sensitive to groundwater that allows measurement of the water content in soil samples considering different scales (Legchenko, 2013). On a large scale (tens of meters), MRS is usually used for investigating aquifers. On a local scale, MRS can be used in borehole or for investigating rock samples. Under ideal theoretical conditions, MRS signal is linearly proportional to the quantity of groundwater. In practice, the complexity of soils structure and instrumental errors may degrade the accuracy of MRS measurements.

In this paper, we report results of the feasibility study of the water content monitoring using time-lapse MRS measurements. The results show that in non-magnetic rocks like chalk and limestone (Beauce aquifer), MRS is able measuring seasonal water content variations in the unsaturated zone.

METHOD

The initial amplitude of the MRS signal versus pulse moment is described by the integral equation

$$e(q) = \frac{\omega_0}{I_0}\int_V B_1 M_0 sin\left(\frac{\gamma B_1 q}{2I_0}\right) w dv. \qquad \text{eq. 1}$$

We consider the 1-D case and approximate the (eq.1) by a matrix equation

$$\mathbf{A}\mathbf{w} = \mathbf{e}. \qquad \text{eq. 2}$$

When processing one individual sounding, solution of the equation (eq.2) is a vertical distribution of the water content *w(z)*. The monitoring data set is composed of *K* individual soundings separated by time intervals Δt_k. and the water content is a two-dimensional function *w(z,t)*. In equation (eq.2), $\mathbf{A} = [a_{i,j}]$ is a rectangular matrix, $\mathbf{e} = [e_i]$ and $\mathbf{w} = [w_j]$ are a set of experimental data and a solution vector respectively (*i=1,2,..,I;* and *j=1,2,..,J*). If *K* is a number of

time-lapse soundings, with l_k pulse moments per sounding ($L = \sum_{k=1}^{K} l_k$), and m_k is a number of model layers per sounding ($M = \sum_{k=1}^{K} m_k$), then I=L×K and J=M×K.

We carry out the time-lapse inversion using the Tikhonov regularization method (Legchenko et al., 2020). For solving (eq.3), we prescribe a smoothness of the water content versus both the depth (z) and the time (t). The smoothed inverse model (**w**) must fit measured amplitudes (**e**) within experimental an error (ε).

$$\begin{cases} \|\mathbf{Aw}-\mathbf{e}\| + \alpha_z \left\|\frac{\mathbf{dw}}{\mathbf{dz}}\right\| + \alpha_t \left\|\frac{\mathbf{dw}}{\mathbf{dt}}\right\| = min. \\ \|\mathbf{Aw}-\mathbf{e}\| \le \varepsilon \end{cases} \quad \text{eq. 3}$$

The water content w_i and the thickness Δz_i of each layer in the MRS inverse model allow estimating the equivalent water column below MRS loop

$$H_{MRS} = \sum_j w_j \Delta z_j. \quad \text{eq. 4}$$

The water column is a more stable parameter than w_i and Δz_i computed separately. H_{MRS} allows easy comparison with the effective rainfall (ERF) corresponding to the quantity of infiltrated water. In the absence of the run-off, the ERF is the difference between the rainfall (RF) and the actual evapotranspiration (AET). We have no data for calculating the AET and we make a simplified estimate using the Penman potential evapotranspiration (PET) provided by Meteo France

$$\begin{cases} ERF = RF - PET, \ if \ RF > PET \\ ERF = 0, \ if \ RF \le PET \end{cases}. \quad \text{eq. 5}$$

RESULTS

We apply the time-lapse inversion to the data set acquired during the MRS monitoring carried out at the Villamblain test site in 1999-2000 and in 2020-2021. This site with the surface area of about 7 km^2 is located approximately 45 km west/north west of Orleans city, which is a part of the Beauce aquifer covering about 9,000 km². Location of the monitoring site is shown in Figure 1.

Figure 1. Location map of the Villamblain experimental site in France (position of the borehole 03622X0119/FP3-25, WGS 84: Lat : 48,00683 m; Lon: 1,59130 m).

The Beauce aquifer has a small regional hydraulic gradient (about 0.1%) and the mean annual recharge was estimated at 110 mm. The area is characterized by developed agriculture with an irrigation in summer time. Calcareous soils and cryoturbated materials cover about 48% of this area, previous studies report an absence of the run-off in Villamblain (Schnebelen et al., 1999). Limestone underlying the soil layer is heterogeneous with variable fracturing and irregular karst development. The specific yield of the limestone matrix estimated by different authors varies between 3 and 13%. The annual rainfall and the GWL variations recorded between 1965 and 2021 are shown in Figures 2a and 2b.

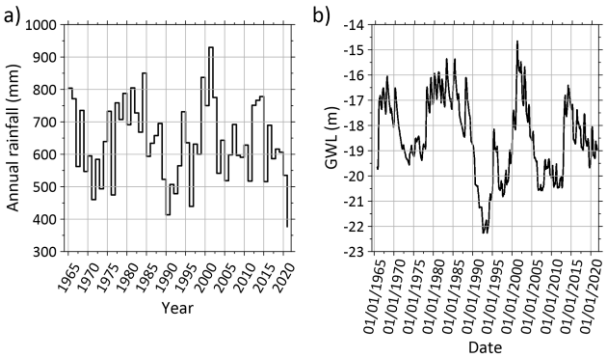

Figure 2. Hydro-meteorological data in Villamblain: a) annual rainfall; b) groundwater level.

BRGM (Bureau de Recherches Géologiques et Minières) carried out the MRS monitoring of the water content in the unsaturated zone using MRS instruments developed by IRIS Instruments (France). The data set comprises results of two one-year long time-lapse MRS measurements performed with a coincident 75×75 m² square loop always set at the same position. The Larmor frequency varied around 2011 Hz in 1999 and around 2039 Hz in 2020. Between the 26 April 1999 and 15 Match 2000 we used the NUMIS instrument and between the 23 July 2020 and 30 June 2021 the NUMIS^{poly} system. MRS measurements provide the water content in the subsurface with the time step of two weeks to one-month.

For monitoring, accuracy of MRS measurements is an important issue. One of the possibilities for verifying our instruments could be comparison of different measurements performed in similar conditions. Meteorological conditions in spring 1999 and in spring 2020 were comparable and we expect that the MRS should show similar signals in summer time of 1999 and 2020. Figure 3 shows the amplitude plotted versus pulse moment of two consecutive soundings performed with the NUMIS instrument (19 July, 1999) and one sounding performed using the NUMIS^{poly} instrument (23 July, 2020). This example confirms that the results obtained with two systems are consistent. However, the water content in the subsurface was not necessary the same and this can explain the small difference in the amplitudes measured in 1999 and in 2020.

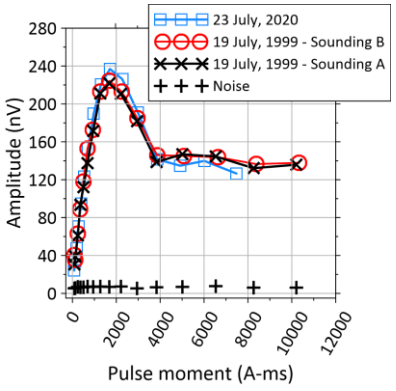

Figure 3. Amplitude of the MRS signal versus pulse moment measured the 19 July 1999 and the 23 July 2020.

Figure 4 shows the water content corresponding to one MRS sounding carried out in 1999 compared with a borehole log.

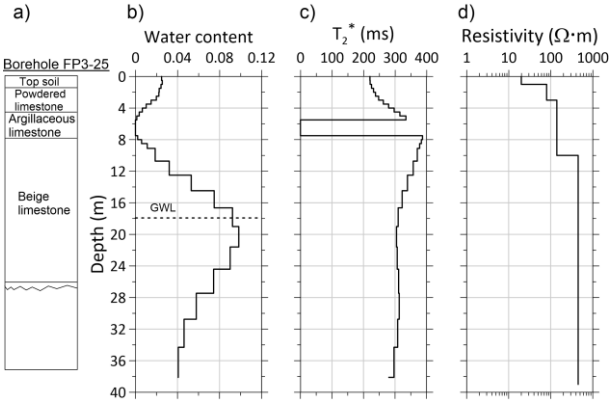

Figure 4. a) The lithological log of borehole 03622X0119/FP3-25 located near MRS station; b) the water content profile provided by the MRS inverse model; c) the relaxation time T_2^*; d) the resistivity log.

One can see that MRS does not show the GWL depth. Capillary rise in the capillary fringe of unsaturated zone (Figure 4b) can explain a smooth increase of the MRS water content toward the GWL. Some clay observed in the borehole corresponds to the waterless interval between 4 and 8 m suggested by MRS. Below 25 m, MRS shows a lower water content corresponding to a smaller specific yield of limestone at larger depth.

The time-lapse inversion provides the water content observed in 1999 (Figure 5a) and 2020 (Figure 5b).

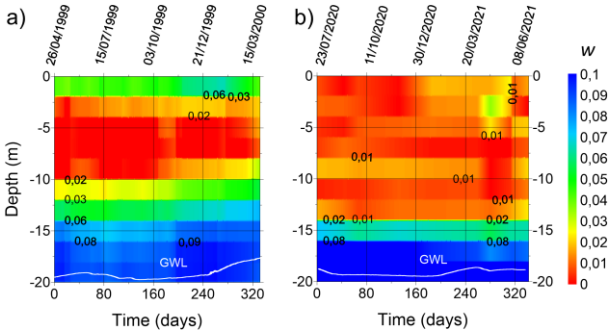

Figure 5. MRS inverse models of the water content (color scale) versus depth and time computed down to 20 m: a) 1999 -2000 data set; b) 2020-2021 data set.

Figure 6 shows measured MRS amplitudes plotted versus normalized pulse moment for each sounding and the inversion fits.

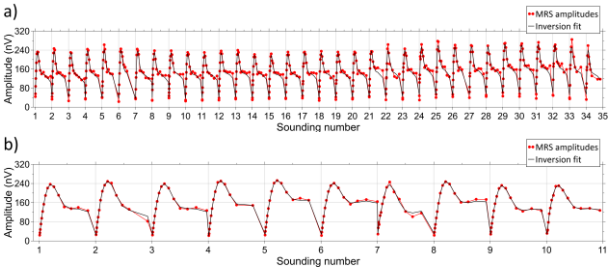

Figure 6. MRS amplitudes versus pulse moment of the corresponding sounding and the inversion fit: a) 1999 -2000 data set; b) 2020-2021 data set.

Figure 7 shows the water column computed after the MRS inverse model (1999-2000). An estimate of the effective rainfall and the GWL show that the increase of the H_{MRS} follows the effective rainfall. The GWL rises with about three months delay after the rainfall. It confirms that MRS measures water in the unsaturated zone.

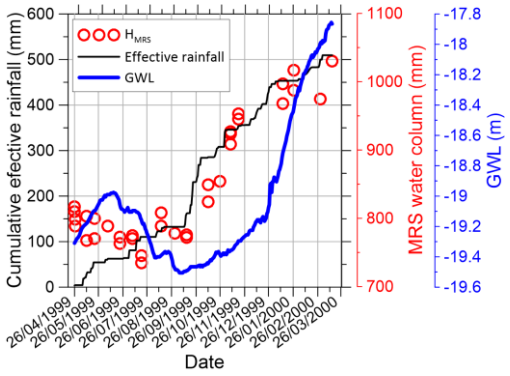

Figure 7. The water column estimated with MRS (red), the cumulative effective rainfall (black) and the depth of the GWL observed in Villamblain in 1999-2000 (blue).

Figure 8 shows the cumulative ERF and the H_{MRS} recorded in 1999-2000 and in 2020-2021. These data cover the one-year seasonal variations with the 21-year separation. In 1999, MRS measurements started the 26 April and in 2020 in the 23 July. In 2020-2021, the cumulative ERF was about 40% less in comparison with the same period of 1999-2020. However, between the 1 January and 11 April the ERF was about the same. In summer, MRS H_{MRS} is about the same in 1999 and in 2020. In fall, more water was stored in 1999, which is consistent with the larger rainfall.

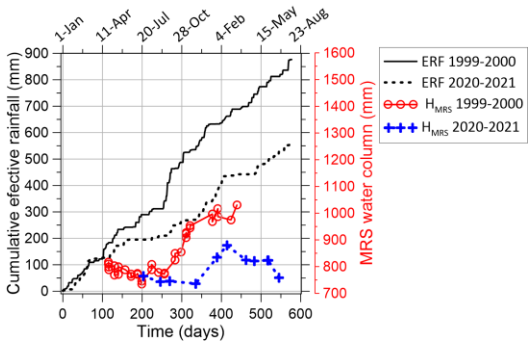

Figure 8. The cumulative effective rainfall (black lines, black axis) and the water column estimated with MRS (red and blue lines, red axis) in 1999-2000 and 2020-2021 plotted versus time since the 1 January of 1999 and 2020 respectively.

DISCUSSION

The water content plots (Figure 5) suggest four layers with different hydraulic properties located at the depths of 0-2 m, 2-10 m, 10-16 m and 16-20 m. During the winter 1999-2000, water was accumulated below 10 m and between 2020 and 2021, the accumulation was less pronounced. Only little water was observed in the layer 2-10 m. MRS cannot see water in clay and MRS results can be interpreted as a low permeable clay material. However, this formation may also correspond to a highly permeable karst with a low storage capacity that allows a rapid water transition. Indeed, Mazzilli et al. (2020) report results of the MRS monitoring of a heavy rain event in karst environment. Large MRS signal was observed only during a few days after the rain. Then, the amplitude of the

signal was stabilized at the same level as before the rain. Thus, an insufficient sampling may explain why we do not see water in the Villamblain karst. If the subsurface was composed of a low permeable material, then we would expect a run-off. But, the run-off was not observed in Villamblain. Thus, we interpret the layer between 2 and 10 m as a karst formation.

CONCLUSIONS

We show that under favourable conditions, MRS can be used as an observation tool for providing an estimate of the water quantity stored in the unsaturated zone. Time-lapse MRS monitoring provides the water content seasonal variations recorded at the scale that is unavailable with other hydrological and geophysical measurements. Our study shows a good correlation of MRS results with the hydrological and meteorological observations.

ACKNOWLEDGMENTS

This work was carried out in the framework of the collaborative research program of BRGM (https://www.brgm.fr/) and IRD-IGE (https://www.ige-grenoble.fr/). The authors acknowledge the support of the Institut des Sciences de la Terre d'Orléans, UMR 7327 Univ. d'Orléans (ISTO, https://www.isto-orleans.fr/) in the framework of the O-ZNS project, which is also a part of the PIVOTS project. We are thankful to the Région Centre-Val de Loire (ARD 2020 program and CPER 2015 -2020) and the French Ministry of Higher Education and Research (CPER 2015 -2020 and the BRGM public service) for their financial support. The fieldwork was co-funded by the European Union with the European Regional Development Fund and by the national research program Labex VOLTAIRE (ANR-10-LABX-100-01).

REFERENCES

Legchenko, A. 2013. Magnetic resonance imaging for groundwater, Wiley-ISTE, 158 pp., Online ISBN:9781118649459, doi:10.1002/9781118649459.

Legchenko, A., Baltassat, J-M., Duwig, C., Boucher, M., Girard, J-F., Soruco, A., Beauce, A., Mathieu, F., Legout, C., Descloitres, M., and Flores Avilés, G.B. 2020. Time-lapse magnetic resonance sounding measurements for numerical modeling of water flow in variably saturated media, Journal of Applied Geophysics, 175, Article 103984, doi:10.1016/j.jappgeo.2020.103984.

Mazzilli, N., Chalikakis, K., Simon D. Carrière, S.D., and Legchenko, A. 2020. Surface Nuclear Magnetic Resonance Monitoring Reveals Karst Unsaturated Zone Recharge Dynamics during a Rain Event, Water 2020, 12, 3183; doi:10.3390/w12113183.

Rubin, Y., and Hubbard, S. 2006. Hydrogeophysics, Springer, 523 pp.

Schnebelen, N, E. Ledoux, A. Bruand, G. Creuzot (1999), Stratification hydrogéochimique et écoulements verticaux dans l'aquifère des calcaires de Beauce (France) : un système anthropisé à forte variabilit spatiale et temporelle, Comptes rendus hebd. séances acad. sci. Paris, 329, 42l-428, doi:10.1016/S1251-8050(00)80066-X.

Surface-Borehole NMR Sensor

[1]Anatoly Legchenko [2]Benoît Texier [3]Jean-François Girard [1]Jean-Michel Vouillamoz
[4]Fabrice Lawson [4]Christian Alle [5]Jean-Michel Baltassat [2]Ghislain Pierrat

[1] Univ. Grenoble Alps, Institute of Research for Development (IRD), IGE, France ; Email: anatoli.legtchenko@ird.fr
[2] IRIS Instruments, Orléans, France ; Email : b.texier@iris-instruments.com
[3] IPGS/EOST, Strasbourg University, France ; Email : jf.girard@unistra.fr
[4] IRD, University of Abomey-Calavi, Bénin ; Email : messan.lawson@ird.fr
[5] BRGM, Orléans, France ; Email : jm.baltassat@brgm.fr

SUMMARY

We present results of an experimental study of the prototype of a borehole NMR sensor that confirm the feasibility of the surface-borehole NMR method (SBNMR). The sensor is build using a 177-cm-long magnetic core with a measuring coil connected to a standard Surface NMR (SNMR) instrument. The use of a sensor in borehole allows increasing the depth of investigation and the resolution of the MRS method. Experimental results show a 5-m-resolution at the depth of 40 m, which is better than that available with SNMR. A blind zone of 0.5 to 1 m around borehole is due to the perturbation of the earth's magnetic field by the magnetic core of the sensor. The relatively large volume investigated with SBNMR and the blind zone around borehole may represent an advantage of the SBNMR relative to the borehole NMR operating in a strong artificial static magnetic field. However, the use of the earth's magnetic field renders performance of the SBNMR method site-dependent with inherently low signal to noise ratio.

Key words: MRS, SNMR, surface-borehole, water content, SBNMR.

INTRODUCTION

Surface NMR method (SNMR) is usually used without drilling boreholes, but the resolution of the method is limited. NMR tools adapted to small boreholes are suitable to groundwater investigations (Walsh et al., 2013) and allow getting a good resolution. Stoeffl (2001) proposed the way for improving resolution by combining the surface and the borehole NMR methods. Using a transmitting loop on the surface and a magnetic field sensor in borehole, we obtain the surface-borehole NMR (SBNMR) method. This concept was tested in the framework of joint research project carried out by IRIS-Instruments, IGE and BRGM. In this paper, we report the first experimental results with a prototype of the sensor.

METHODS

Figure 1 shows the measuring setup consisting of a transmitting loop (*Tx*) on the ground surface and the NMR sensor in borehole (*Rx*).

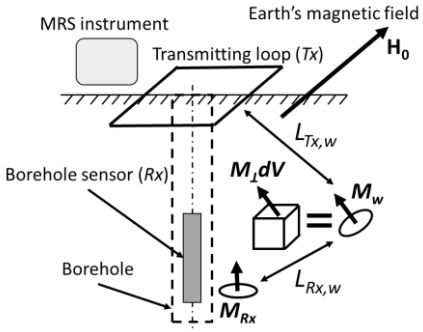

Figure 1. Transmitting loop on the surface and NMR sensor in borehole.

A prototype of the surface-borehole NMR sensor was made in France and tested in France and in Benin. For measuring, we used commercially available NUMIS^{poly} MRS instrument without any modification.

RESULTS

The sensor is composed of a magnetic core and an open-core measuring coil (Figure 2a). The coil is connected to the MRS instrument and tuned in resonance with the Larmor frequency. The length of the sensor is 177 cm. It is mechanically protected by a plastic tube.

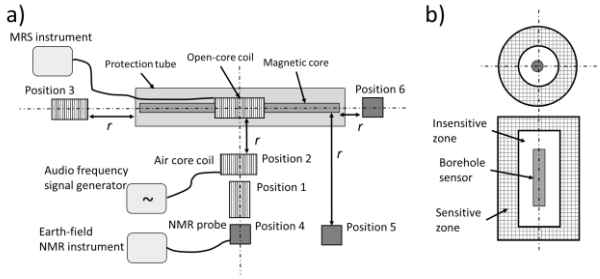

Figure 2. a) A sketch of the design of borehole NMR sensor and the experimental setup for measuring parameters of the sensor. b) The volume around borehole sensor producing measurable NMR signal.

A coaxial cylinder (Figure 2b) can approximate the sensitive zone of the NMR sensor. Around the sensor, the earth's magnetic field is perturbed by the magnetic core of the sensor, which causes the insensitive zone. A cylinder, but smaller one also can approximate the insensitive zone. For investigating the area where the earth's magnetic field is perturbed by the sensor, we use an earth-field NMR instrument and a water sample in a 10-cm-long tube of 4 cm in diameter. The water sample is set

at different positions shown in Figure 2a and we measure the relaxation time T_2^* and the Larmor frequency. At the distance less than 50 cm, the free induction decay signal (FID) cannot be measured because of short values of T_2^*. Only spin-echo (SE) measurements allow observing NMR signal. At larger distances, the FID signal was well observed.

For studying extensions of the sensitive zone, we use an audio frequency signal generator connected to an air core coil. For measuring voltage induced in the sensor, we use an MRS instrument (Figure 2a). Both the generator and the MRS instrument are tuned at the same frequency of 1985 Hz. We set the coil at different positions around the sensor and measure voltage versus distance between the coil and the sensor. Normalized amplitude of the signal versus distance is shown in Figure 3.

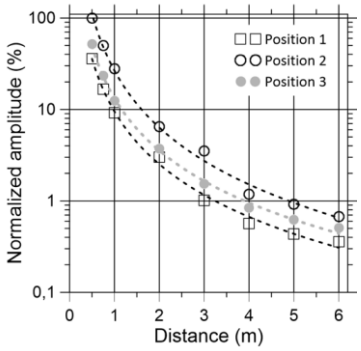

Figure 3. Normalized amplitude of the test signal measured at different positions of the signal generator versus distance between the sensor and the generator. Dashed lines show the power fit of experimental data.

The signal is rapidly decreasing and at the distance of 6 m from the sensor the amplitude is about 0.6% of the initial value measured at the distance of 0.5 m. For each position, measured amplitudes can be fitted by a function a/r^2 (dashed lines). The fitting coefficient a has an individual values for each position. These measurements show that near the real sensor, the sensitivity decreases with the rate of approximately ~ $1/r^2$.

We show results of SBNMR measurements carried out in Benin near existing borehole (inclination of the earth's magnetic field of 5°, the Larmor frequency of 1393 Hz). At the test site in Benin, the aquifer is located between 14 and 50 m. It is composed of mainly sand but also contains a clay layer (Figure 4).

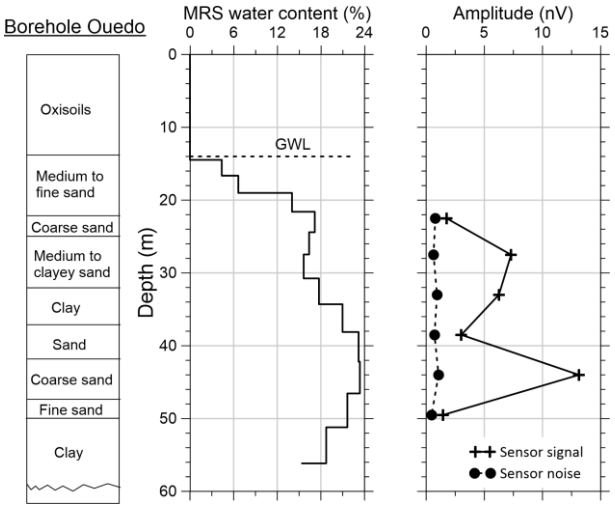

Figure 4. Experimental verification of the surface-borehole NMR tool in Benin (from left to right): lithological log of the borehole Quedo; water content distribution provided by a standard MRS sounding performed with a 62.5-m-side figure eight *Tx/Rx* loop; amplitude of the sensor response versus depth (after the pulse – crosses; before the pulse – circles).

A standard MRS sounding carried out with a 62.5-m-side figure eight loop provides the water content distribution that shows the aquifer, but does not show the clay a 5-m-thick clay layer located at the depth of 32 m. The bottom of the aquifer is also not resolved.

Measurements of the amplitude versus pulse moment carried out with the 25-m-side *Tx* loop (3 turns) show pronounced difference between signals measured with the sensor located at different depths (Figure 4) thus demonstrating a good vertical resolution of the method.

Figure 5 shows examples of time records. Each graph corresponds to one of the sensor positions. Solid lines show the envelope of the signal amplitude versus time and the dashed lines show the noise amplitude recorded before the pulse. At all sensor positions, the SBNMR signal clearly dominates noise, thus confirming the feasibility of our SBNMR measurements. These examples also demonstrate pronounced differences between SBNMR signals recorded at different depths corresponding to different geological patterns. The mean noise was 1.14 nV with the maximum signal amplitude of 16 nV.

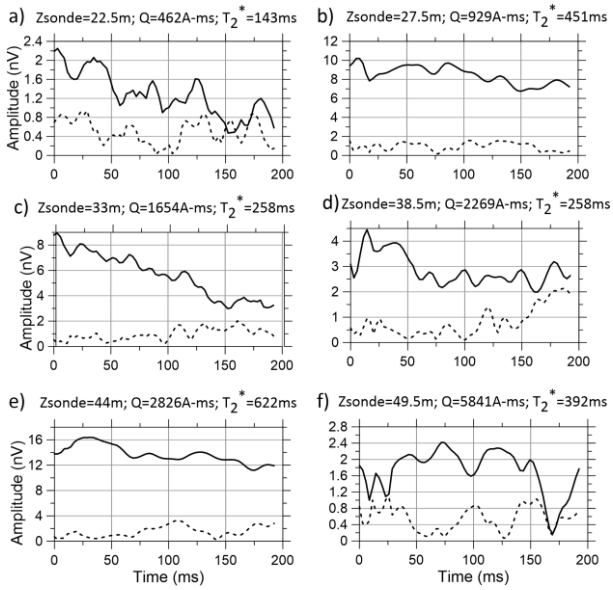

Figure 5. SBNMR records measured with the sensor located at different depths. Solid lines show the SBNMR signal recorded after the dead time following the pulse and short-dashed lines show noise records before the pulse.

DISCUSSION

The SBNMR has the similarities and the differences in comparison with both the SNMR and the borehole NMR, but provides information about groundwater unavailable with these two methods thus filling the gap in-between.

The borehole NMR uses an artificial static magnetic field that allows a very high sensitivity and a very good signal to noise ratio. The depth resolution of the borehole NMR and the maximum depth of investigation are also much better in comparison with the SBNMR and the SNMR. However, the area investigated with the borehole NMR represents a hollow

cylinder coaxial with the NMR tool. The sensitive area is located within the walls of the cylinder. The diameter (<40 cm) and the thickness of the walls (<2 mm) of this cylinder are determined by the gradient of the static magnetic field. Consequently, hydraulic parameters of the aquifer formation investigated with the borehole NMR are representative only around borehole.

Operating in the geomagnetic field, the SNMR and the SBNMR have both low sensitivity and consequently poor signal to noise ratio. The investigated area depends on the size of the transmitting loop and may be larger than 150×150 m^2 for the SNMR and 30×30 m^2 for the SBNMR. The SBNMR has better vertical resolution and potentially larger depth of investigation in comparison with the SNMR. It allows better characterization of investigated aquifer formation in terms of geometry, porosity and hydraulic conductivity.

Despite of much better metrological performance in comparison with the SNMR and SBNMR, the borehole NMR has a big disadvantage. Indeed, the investigated area around borehole is narrow and the aquifer formation around borehole may be perturbed by drilling, which can bias results of the study. In the contrary, the SNMR and SBNMR provide data averaged over large volume not perturbed by borehole thus smoothing heterogeneities in the aquifer parameters.

CONCLUSIONS

We developed and successfully tested a borehole sensor for the surface-borehole NMR method. Experimental verification of the method shows that the sensitive area of the sensor is located within a coaxial with borehole cylinder. Groundwater at the distance of 0.5 to 1 m around borehole does not produce measurable NMR signal because of strong perturbation of the earth's magnetic field by the magnetic core of the sensor.

Performance of the SBNMR method is site dependent and the position of the transmitting loop relative to borehole should be adapted to measuring conditions. SBNMR measurements are carried out in the earth's magnetic field and consequently, the signal to noise ratio is comparable with the SNMR method being inherently poor.

ACKNOWLEDGMENTS

This work was carried out in the framework of collaboration agreement between IRD, IRIS Instruments and BRGM. The authors acknowledge financial support provided by the grants from the French national programs Labex OSUG@2020 (Investissements d'avenir – ANR10 LABX56) and "Investment for Future - Excellency Equipment" project EQUIPEX CRITEX (grant # ANR-11-EQPX-0011). Field data in Benin were obtained in the framework of the GRIBA project funded by the African Union, the European Union, and IRD (grant AURG/098/2012).
The content of this paper is the responsibility of the authors and cannot be regarded as reflecting the position of the European Union or the African Union.

REFERENCES

Legchenko, A., 2013. Magnetic Resonance Imaging for Groundwater. Wiley-ISTE 978-1-84821-568-9.

Stoeffl, W., 2001. Use of earth field spin echo NMR to search for liquid minerals. Patent N° US 6,177,794 Bl.

Walsh, D., Turner, P., Grunewald, E., Zhang, H., Butler, J.J. Jr., Reboulet, E., Knobbe, S., Christy, T., Lane, J.W. Jr., Johnson, C.D., Munday, T., Fitzpatrick, A., 2013. A small-diameter NMR logging tool for groundwater investigations, Groundwater, 51(6), 914–926, doi:10.1111/gwat.12024.

Global sensitivity analysis of Magnetic Resonance Sounding simulated responses to the hydraulic parameters of a catchment hydrogeological model

[1]N Lesparre

[1] University of Strasbourg, ITES
5 rue Descartes, 67000 Strasbourg, France
lesparre@unistra.fr

[2]P Ackerer

[2] University of Strasbourg, ITES
5 rue Descartes, 67000 Strasbourg, France
ackerer@unistra.fr

[3]JF Girard

[3] University of Strasbourg, ITES
5 rue Descartes, 67000 Strasbourg, France
jf.girard@unistra.fr

[4]A Younes

[4] University of Strasbourg, ITES
5 rue Descartes, 67000 Strasbourg, France
younes@unistra.fr

[5,6]T Mara

[5] PIMENT, Université de La Réunion, FST,
15 Avenue René Cassin, 97715 Saint-Denis, France
thierry.mara@univ-reunion.fr

[6] European Commission, Joint Research Centre
Directorate for Foresight, Modelling, Behavioural Insights and Design for Policy, 21027 Ispra (VA)

SUMMARY

We apply a global sensitivity analysis of magnetic resonance sounding (MRS) data to the hydraulic parameters of a hydrological model at a catchment scale. The methodology used provides a quantitative estimate of the proportion to which the explored parameters influence the simulated MRS response. The sensitivity analysis is performed through a variance-based approach that provides indicators to infer how the MRS sensitivity to the different parameters might vary in space and time. We also apply the sensitivity analysis to water table depth estimates. We show that MRS measurements complement fruitfully classical water table depth acquisitions. Indeed, MRS is sensitive to the model water content at saturation while this parameter does not influence significantly the water table depth estimates.

Key words: MRS, hydrological model, sensitivity analysis, catchment scale

INTRODUCTION

Magnetic resonance sounding (MRS) is a geophysical method directly sensitive to the underground water content. Beyond the estimate of the water content state at a given time, the method has been successfully applied to constrain the parameters of hydrological models. At the scale of one MRS acquisition setup (a few tens of meters), Costabel & Günther (2014) explored how MRS data can help estimating the water retention parameters. At a similar scale, Herckenrath et al. (2012) studied the relevance of coupled MRS and gravity measurements repeated over time to retrieve the aquifer characteristics during a pumping test. Boucher et al. (2012) used MRS measurements to constrain the hydraulic conductivity at saturation of a hydrological model applied at a catchment scale. Similarly, the fitting of MRS data covering a catchment with estimates from a hydrological model highlighted the necessity to divide the aquifer in two vertical layers with a deeper less porous medium (Lesparre et al., 2020). More recently, the acquisition of time-lapse MRS measurements helped modelling the water flow in an unsaturated medium (Legchenko et al., 2020).

Applications of time-lapse MRS acquisitions are progressing and a recent study showed its interest to monitor water infiltration during a rainy event (Mazzilli et al., 2020). In this paper, we explore how such time-lapse MRS simulated measurements are sensitive to the parameters of a hydrological model in order to discriminate which parameters MRS could help constraining in practice. For this purpose, we perform a global sensitivity analysis (GSA) of MRS data to the hydraulic parameters of a hydrogeological model applied on the Strengbach catchment (Fig. 1). We applied the measured meteorological forcing during a six-month period and analyse the variability of the MRS estimate at two stations presenting contrasting hydrological behaviours. We perform the same analysis with water table depth estimates to illustrate the complementarity between MRS and piezometric head data.

METHODS

The hydrological model applied covers the whole Strengbach catchment of 0.8 km², located in the Vosges mountains (North-East of France). The catchment climate is temperate of oceanic mountainous type with a mean temperature of 6°C. 90% of the catchment is covered by forest with 80% of spruces and 20% of beeches. The underlying bedrock is of granitic type and the soils are coarsely grained, sandy and rich in gravels and pebbles.

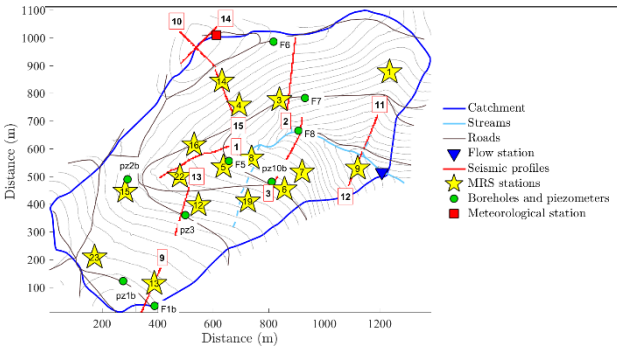

Figure 1. Distribution of MRS measurement stations and seismic profiles acquired on the Strengbach catchment.

We use the Normally Integrated Hydrological Model (NIHM) to simulate the water flow in the underground and at the surface through a coupling between the two compartments (Pan et al., 2017, Weill et al., 2017, Jeannot et al., 2018). We run 2500 synthetic models with randomly selected hydrological model parameter values. We focus the analysis on, the water content at saturation θ_s, the hydraulic conductivity at saturation K_s and the α parameter of the Van Genuchten equation. The aquifer is divided in two vertical layers corresponding to the soil and the saprolite, the last one being less porous. The soil and the saprolite thicknesses are defined through a statistical analysis of seismic profiles covering the catchment (Fig. 1). Geostatistical models are generated to reproduce the measured seismic velocity at the profile location and their statistical variability at the catchment scale. The soil and saprolite bottom interfaces are then determined by fixing a seismic velocity threshold of 700 m/s and 2000 m/s, respectively. The soil and saprolite thicknesses vary then normally in each element of NIHM. θ_s and α vary uniformly, while K_s follows a uniform distribution in the logarithmic domain. The variation ranges of those three parameters are summarized in Table 1.

Table 1: Range of variations of the explored parameters.

	Soil	Saprolite
K_s (m/s)	10^{-5} - 10^{-3}	10^{-6} - 10^{-4}
θ_s (%)	5 - 60	2 - 10
α (m^{-1})	0.1 - 2	0.1 - 2

The models run from the 1st of June 2012 to the 31st of May 2013, the first 6 months are used to "warm-up" the simulations and the GSA is applied from the 1st of December 2012. The studied period shows several distinct rainy events (Fig. 2), so we can examine the influence of different water content states on the MRS and water level depth variability. The measured precipitation and the estimated evapotranspiration are provided as a model input, such data come from the OHGE meteorological station (Fig. 1). The temperature is also given to determine the nature of the precipitation (rain or snow) and in case of snow, the infiltration is delayed depending on the temperature and on the previous height of snow accumulated.

NIHM provides as outputs the flow at the outlet, the water head at each MRS and piezometric stations and daily maps of the underground water content used to estimate the MRS signal as described in Lesparre et al (2020). The global sensitivity of each data type to the parameters explored is then analysed through variance-based sensitivity indices (Mara and Tarantola, 2008). Such indices distinguish the contribution of each parameter to the signal total variance (Sobol' 2001). Let's consider a model defined with P independent random parameters $X = \{x_1, \ldots, x_P\}$ and a resulting signal estimate $y(X)$, the first order sensitivity Sobol' index S_i corresponding to x_i writes:

$$S_i = \frac{V[E[y(X) \mid x_i]]}{V[y(X)]} . \quad (1)$$

$E[\ |\ ]$ is the conditional expectation operator and $V[]$ represents the variance. S_i represents the amount of the total signal variance that is related to the x_i parameter only.

We compute the Sobol' indices through Polynomial Chaos Expansion (PCE; Wiener, 1938). Such representations are indeed particularly suited to perform variance-based GSA (Younes et al., 2018). The Sobol indices are directly computed from the PCE coefficients, without running the surrogate models, at a daily rate at each measurement point and for each data type.

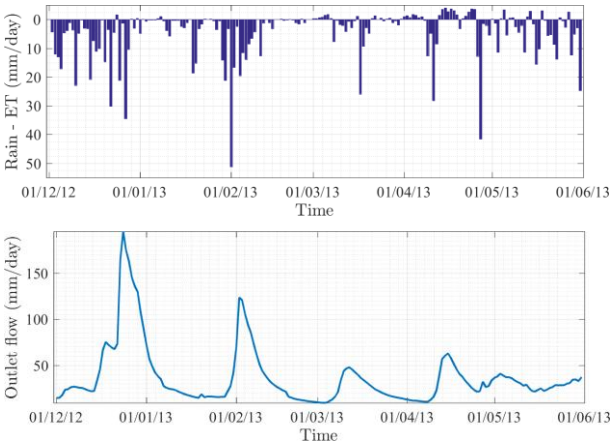

Figure 2. Rain minus the evapotranspiration measured on the Strengbach catchment used as the meteorological forcing inserted in NIHM (top). Flowrate measured at the catchment outlet (below).

RESULTS

The contribution of the explored parameters to MRS signal variance as function of time is represented for station 7 and 22 Fig. 3. For sake of concision we limit here the analysis to those stations since they present a distinct hydrogeological behaviour. Station 7 is situated in a steep region that favours water drainage. Conversely, station 22 is located on a relatively flat region more suitable for water storage. We note that the variance of the MRS signal is much stronger at station 22 than at the 7th. We observe that at both stations the MRS signal is mainly sensitive to the soil θ_s and the saprolite K_s.

However, we note that this sensitivity varies with time, notably concerning the K_s parameter. At station 7, the contribution of K_s is higher in winter during the drainage periods that follow high flow events. At station 22, K_s shows also a higher contribution in a period of drainage, but in spring when precipitations are less intense and more scattered across time. Both stations are also sensitive to the saprolite θ_s, station 7 is more significantly sensitive to the soil α value, while station 22 is sensitive, at times, to the saprolite α. Station 22 is also much more sensitive to the soil thickness than station 7. We also observe that a large part of the signal variance is related to contributions concerning several parameters in interaction since the total variance (blue lines) is well above the respective contributions of each explored parameter.

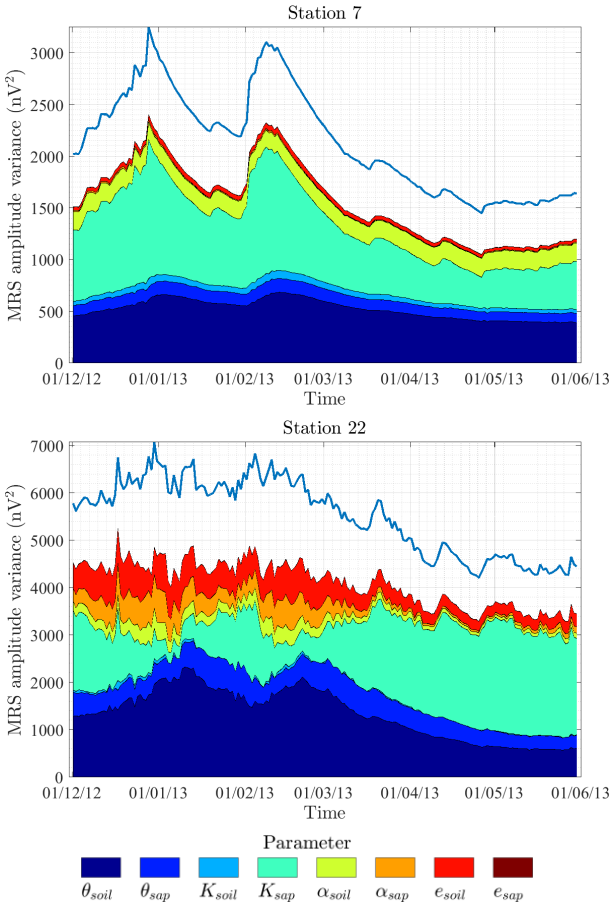

Figure 3. Variance of the MRS signal as function of time estimated at station 7 (top) and 22 (bottom). The blue line represents the total signal variance while the coloured areas indicate the respective contribution of the explored parameters.

The application of the same GSA to water table depth underlines the complementarity between MRS and piezometric data. In particular, the water table depth variance is not significantly impacted by the θ_s parameter (Fig. 4). Under both stations, the water table depth variance is mostly sensitive to the saprolite K_s, and to the α parameter of both the soil and saprolite. We note that the variance at station 7 is very smooth. At station 22, the variance of the water table depth presents much more irregulrities corresponding to the different precipitation events. We note that the impact of saprolite K_s on the water table depth signal increases with the spring arrival. As for the MRS signal, a part of the water table depth total variance is related to interactions between several parameters.

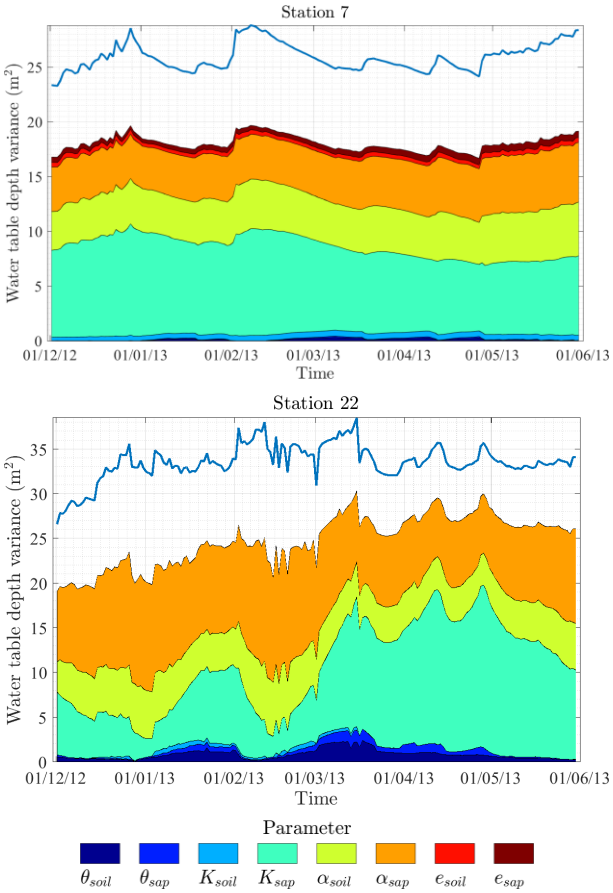

Figure 4. Variance of the water table depth as function of time estimated at station 7 (top) and 22 (bottom). The blue line represents the total signal variance while the coloured areas indicate the respective contribution of the explored parameters.

CONCLUSIONS

We applied a GSA of MRS data to hydraulic parameter of a hydrological model applied on a headwater catchment. The meteorological forcing input to the model corresponds to a measured chronicle. From that analysis, we show that MRS data are mostly sensitive to the soil θ_s and the saprolite K_s parameters. We observe a distinct behaviour from a measurement station to another. In particular a region favouring drainage is strongly sensitive to the saprolite K_s parameter in winter during the snow melt period. However, below an area suitable for storage, the sensitivity to that same parameter is more pronounced in spring.

Our study emphasizes the complementarity of MRS acquisitions to piezometric measurements as only the MRS data show a strong influence to the θ_s parameter. The preliminary

analysis of these results invites to deepen the study to distinguish which coupled parameters impact both the MRS and piezometric signal. A study of the whole measurement stations variance would also help understanding the respective role of the different parameters to the MRS and water table depth signals. The GSA performed here encourages time-lapse MRS measurements at different places of a catchment to confirm our findings by including aspects such as the measurements noise that could vary in space and time.

ACKNOWLEDGMENTS

Meteorological and flow rate data collection was funded by the Observatoire Hydro-Géochimique de l'Environnement (OHGE), which is financially supported by CNRS/INSU France and the University of Strasbourg. OHGE is part of the OZCAR research infrastructure (http://www.ozcar-ri.org). The authors would like to acknowledge the ANR HYDROCRIZSTO-15-CE01-0010-02 project. Computing time was provided by the HPC-UdS.

REFERENCES

Boucher, M., Favreau, G., Nazoumou, Y., Cappelaere, B., Massuel, S., & Legchenko, A. 2012. Constraining groundwater modeling with magnetic resonance soundings. Groundwater, 50(5), 775-784.

Costabel, S., & Günther, T. (2014). Noninvasive estimation of water retention parameters by observing the capillary fringe with magnetic resonance sounding. Vadose Zone Journal, 13(6).

Herckenrath, D., Auken, E., Christiansen, L., Behroozmand, A.A., & Bauer-Gottwein, P. 2012. Coupled hydrogeophysical inversion using time‐lapse magnetic resonance sounding and time‐lapse gravity data for hydraulic aquifer testing: Will it work in practice?. Water Resources Research, 48(1).

Jeannot, B., Weill, S., Eschbach, D., Schmitt, L., & Delay, F., 2018. A low-dimensional integrated subsurface hydrological model coupled with 2-D overland flow: application to a restored fluvial hydrosystem (Upper Rhine River–France). Journal of Hydrology, 563, 495–509.

Legchenko, A., Baltassat, J. M., Duwig, C., Boucher, M., Girard, J. F., Soruco, A., Beauce, A., Mathieu, F., Legoute, C., Descloitres, M., & Flores Avilés, G.P. 2020. Time-lapse magnetic resonance sounding measurements for numerical modeling of water flow in variably saturated media. Journal of Applied Geophysics, 175, 103984.

Lesparre, N., Girard, J. F., Jeannot, B., Weill, S., Dumont, M., Boucher, M., Viville, D., Pierret, M.C., Legchenko, A., & Delay, F. 2020. Magnetic resonance sounding measurements as posterior information to condition hydrological model parameters: Application to a hard-rock headwater catchment. Journal of Hydrology, 587, 124941.

Mara, T.A., & Tarantola, S. 2008. Application of global sensitivity analysis of model output to building thermal simulations. In Building Simulation (Vol. 1, No. 4, pp. 290-302). Springer Berlin Heidelberg.

Mazzilli, N., Chalikakis, K., Carrière, S. D., & Legchenko, A. (2020). Surface Nuclear Magnetic Resonance Monitoring Reveals Karst Unsaturated Zone Recharge Dynamics during a Rain Event. Water, 12(11), 3183

Pan, Y., Weill, S., Ackerer, P., & Delay, F. 2015. A coupled stream flow and depth-integrated subsurface flow model for catchment hydrology. Journal of Hydrology, 530, 66–78.

Sobol', I.M. 2001. Global sensitivity indices for nonlinear mathematical models and their Monte Carlo estimates. Mathematics and computers in simulation, 55(1-3), 271-280.

Weill, S., Delay, F., Pan, Y., & Ackerer, P. 2017. A low-dimensional subsurface model for saturated and unsaturated flow processes: ability to address heterogeneity. Computation Geosciences, 21 (2), 301–314.

Wiener, N. 1938. The homogeneous chaos. American Journal of Mathematics, 60(4), 897-936.

Younes, A., Zaouali, J., Lehmann, F., & Fahs, M. 2018. Sensitivity and identifiability of hydraulic and geophysical parameters from streaming potential signals in unsaturated porous media. Hydrology and Earth System Sciences, 22, 3561-3574.

Application of Magnetic Resonance Soundind and Electrical Resistivity Tomography to investigate the lateral seepage of the Yellow River in Liaocheng area, China

[1]Li Yulin [1]Li Zhenyu* [1]Li Fan [1]LU Kai

1 Institute of Geophysics and Geomatics,China University of Geosciences (Wuhan)

388 Rumo Rd., Wuhan (430074), Hubei, China
Lizhenyu626@126.com

SUMMARY

Magnetic Resonance Sounding (MRS) Technology is a new electromagnetic exploration method. This method is mainly used for the detection of groundwater. Compared with the traditional geophysical exploration method to detect the underground water, MRS technology has many advantages that other methods do not have, such as the rich information, sensitive and convenient, and quantitative inversion. So far, MRS is only a direct search for groundwater geophysical exploration that can explore the groundwater directly.

Lateral seepage of the Yellow River has always been an important recharge source of groundwater in the area along the Yellow River, which plays a significant role in alleviating the water resource shortage in the cities and irrigation areas along the lower reaches of the Yellow River. Studying and grasping the process of lateral seepage of the Yellow River will provide a basis for the evaluation of groundwater resources along the Yellow River. It has a positive and realistic significance for the rational utilization of water resources, the management of the lower Yellow River and the protection of the ecological environment of the lower Yellow River.

In order to study and master the Yellow River lateral seepage process, using Magnetic Resonance Sounding and Electrical Resistivity Tomography (ERT) to detect in the studied area, combining with the characteristics and advantages between different technical methods, complement each other and validation, finally it is concluded that the underground strata distribution, water table depth, aquifer, geotechnical information.

Key words: MRS, ERT, The Yellow River lateral seepage.

INTRODUCTION

The Yellow River is the main birthplace of Chinese civilization. It flows through nine provinces and finally flows into the Bohai Sea. The middle and upper reaches of the Yellow River are dominated by plateaus, and the middle and lower reaches are dominated by plains and hills. As the middle part of the river is mainly in the Loess Plateau area, which has serious soil and water loss, it carries a large amount of sediment. The sediment has been silted over the years and the riverbed has been rising, making the lower reaches of the Yellow River a world-famous "suspended river on the ground", forming a large number of lateral seepage of the Yellow River.

The lateral seepage of the Yellow River has always been an important recharge source of groundwater along the river, which plays a significant role in alleviating the shortage of water resources in cities and irrigation areas along the river in the lower reaches of the Yellow River. Studying and mastering the lateral infiltration process of the Yellow River will provide a basis for the evaluation of groundwater resources along the Yellow River, and have positive and practical significance for the rational utilization of water resources, the treatment of the lower reaches of the Yellow River and the protection of ecological environment in the lower reaches of the Yellow River.

In this paper, the North Bank of the Yellow River from Aishan hydrological station to zhoumenqian village, Liaocheng City, Shandong Province is selected as the study area(Figure 1). ERT and MRS are used for joint detection. The detection results give the information of underground stratum distribution, water table depth, rock and soil permeability and aquifer distribution in the study area. Compared with the traditional borehole in-situ observation method, the information of underground stratum distribution, permeability and water table depth measured by ERT and MRS has more efficient and economic advantages, and can make up for the limitations of borehole one hole view.

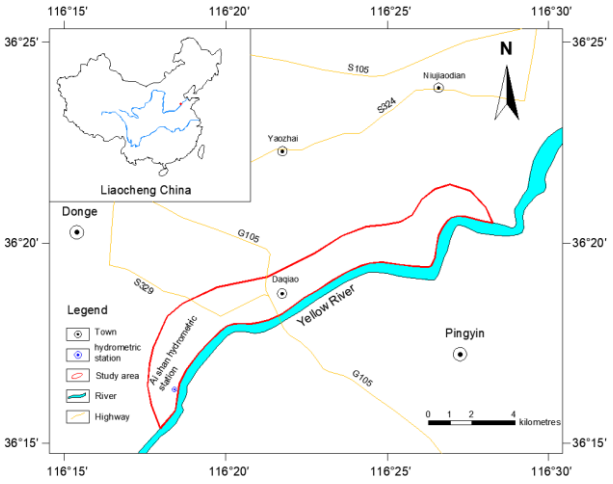

Figure 1. Study area

METHODS

An MRS and ERT investigation of the lateral seepage was carried out in 2018. We established 17 MRS measuring points and 4 ERT measuring lines across the zhoumenqian village (Figure 2).

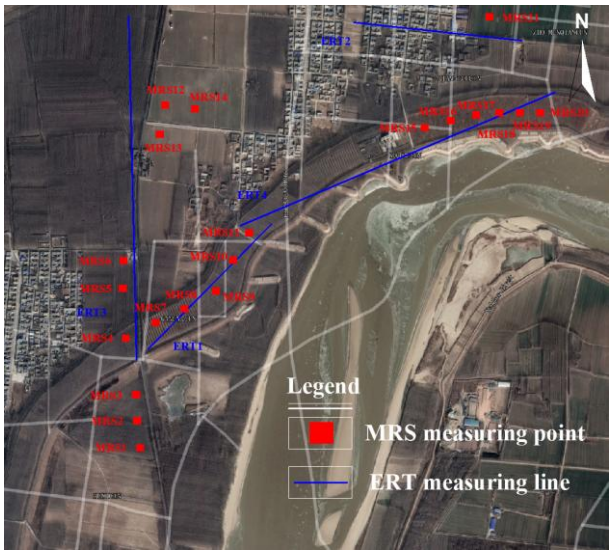

Figure 2. Layout of survey lines and points

The deployed MRS instrument was the NUMIS^{POLY}, the most advanced ground-based NMR instrument manufactured by IRIS. This instrument is powerful and highly sensitive and emits alternating electromagnetic fields of a certain frequency into the ground via large coils on the surface. These coils can be arranged as square, round or figure 8-shaped patterns according to the field conditions and magnitude of electromagnetic interference. The frequency of the electromagnetic field can be determined according to the intensity of the regional geomagnetic field.

$$f_L = \gamma B_0 / 2\pi \qquad \text{eq.1}$$

Where f_L is the frequency of the excitation electromagnetic field (the Larmor frequency) and γ is the proton gyromagnetic ratio. After a Larmor-frequency electromagnetic pulse is emitted by the coil into the ground during a certain period, the hydrogen nuclei in groundwater absorb electromagnetic wave energy and attain the excited state. At this point, the excitation current in the coil is cut off. After a certain period (the dead time), we employ the same coil to receive the relaxation signal of the hydrogen nuclei in water, which decay from a high-energy state to a low-energy state. The signal strength is generally related to the groundwater content, and the signal attenuation rate depends on the extent of the water-rich pore structure.

Before the exploration survey, we first measured the geomagnetic field intensity with a GSM-19T system at 30 locations distributed across the seepage area. The measurement results indicated that the geomagnetic field in the landslide area remained relatively stable, fluctuating less than 48 nT, and the average geomagnetic field intensity was 52999.99 nT, while the Larmor frequency was set to 2256.6 Hz according to Equation (eq.1). A square figure coil pattern was employed. The length of the coil side was 100 meters, with 1 turn, and the length of the coil was 400 meters. The number of excitation pulses was set to 16, the duration of the excitation pulses was set to 40 ms, the dead time was set to 40 ms, and the number of stacking pulses was set to 64 to 128.

The deployed ERT instrument was the WDJD-4. The instrument applies current through the power supply electrode to form an artificial current field in the formation. The electric field distribution satisfies the following partial differential equation.

$$\nabla^2 U = \frac{-I}{\sigma}\delta(x-x_0)\delta(y-y_0)\delta(z-z_0) \qquad \text{eq.2}$$

Where x_0、y_0、z_0 are the origin coordinates and x、y、z are the field point coordinates. When space is passive, $\nabla^2 U = 0$.

In the actual measurement, after supplying power to electrodes A and B, the potential difference between electrodes M and N can be received, and the resistivity can be obtained after calculation.

$$\rho = \frac{2\pi}{\frac{1}{AM} - \frac{1}{AN} - \frac{1}{BM} + \frac{1}{BN}} * \frac{\Delta U_{MN}}{I} \qquad \text{ep.3}$$

Where ρ is the resistivity. Specific collection parameters are listed in Table 1.

Table 1 Acquisition parameters of the SNMR method

Measuring lines	Length(m)	Number of electrode	Electrode distance(m)	Isolation coefficient
ERT1	595	120	5	39
ERT2	55	120	5	39
ERT3	1460	150	10	19
ERT4	1460	150	10	19

RESULTS

SNMR results

A histogram of the water content distribution can be obtained through the inversion of the data of the seventeen measuring points. Figure 3 and 4 show the distribution of groundwater and permeability coefficient at measuring points MRS1 ~ 6, MRS7 ~ 11 and MRS12 ~ 17 from top to bottom.

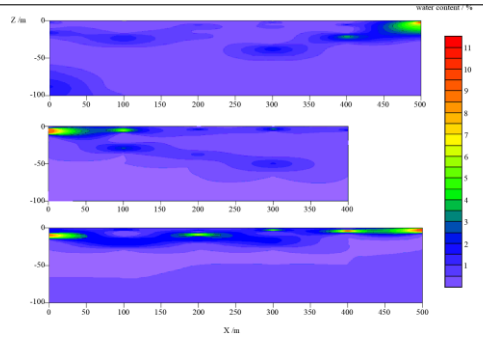

Fifure 3. Water content

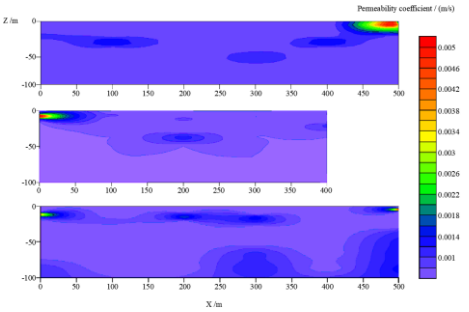

Figure 4. permeability coefficient

The results indicate that the groundwater distribution is not uniform with the depth, and the water content per unit volume in the local water-rich area is approximately 5% ~ 7%. The water-cut distribution at each measuring point can generally be divided into two water-cut areas from shallow to deep. The water-cut area in the shallow part is generally located within the range from 0 ~ 5 m to 0 ~ 10 m. The water-cut area in the upper part is much larger than that in the lower part. The water-bearing area of the second layer ranges from 10 m to 40 m. Moreover, it can be seen from the aquifer distribution of measuring point mrs1-6 in Figure 3 that the aquifer depth perpendicular to the river bank tends to increase. After correction, the permeability coefficients of aquifers in the three regions are 6×10^{-7}m/s, 1×10^{-6}m/s and 3×10^{-3}m/s.

ERT results

A histogram of the inversion resistivity cross-section diagram can be obtained through the inversion of the data of the four measuring lines. Figure 5 shows the underground resistivity distribution of ert1 ~ 4 survey line from top to bottom.

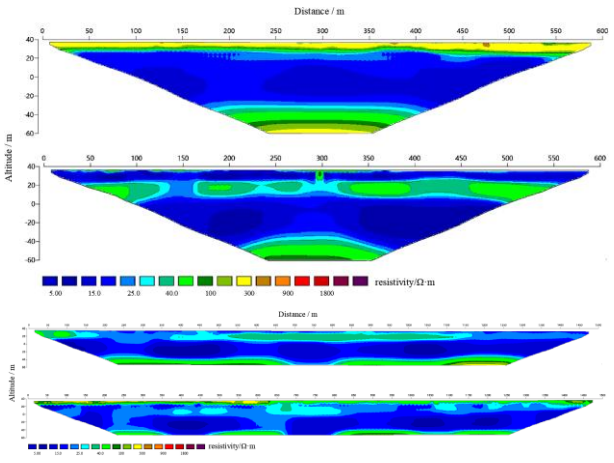

Figure 5. Inversion resistivity cross-section diagram

The results show that according to the resistivity distribution, it can be divided into four electrical layers from the surface to the depth of 100m. The depths are 3 ~ 5m, 5 ~ 50m, 20 ~ 30m and below. The third layer is contained in the second layer with high resistivity, which is a saturated aquifer, the first layer is an unsaturated layer, the second layer is a saturated clay layer, and the fourth layer is bedrock. It can be inferred that the depth of the water table is about 3 ~ 5m.

The results of ERT and MRS in zhoumenqian village show that the overall thickness of the Quaternary System in the area is about 80 ~ 100m, mainly composed of cohesive soil and sandy soil, with poor permeability. After comparison and correction with the existing regional borehole geological data and the empirical value of rock and soil permeability coefficient, it is about 2 ~ 4×10^{-7}m/s and 1.4×10^{-6} m/s respectively. Saturated sand aquifer exists locally in the overburden, with water content per unit volume of about 5% ~ 7% and permeability coefficient of about 3×10^{-3}m/s。 The depth of water table in the area is shallow, about 3 ~ 5m, slightly lower than the water level of the Yellow River.

Therefore, the recharge relationship between the Yellow River and groundwater in the area is that the Yellow River recharges groundwater, and the recharge rate is slow.

CONCLUSIONS

To locate the origin of the lateral seepage of the Yellow River, we used non-destructive geophysical detection methods (MRS and ERT). Geological data show that the Yellow River lateral seepage exists in the study area, which is the result of sediment accumulation for many years. At the same time, the Yellow River lateral seepage is also an important recharge source of groundwater in the middle and lower reaches.

We set up MRS measuring points and ERT measuring lines on the North Bank of the Yellow River where the population is concentrated. MRS method identified the location and permeability coefficient of the water bearing area, ERT method determined the distribution of the stratum, and the combination of the two methods determined the depth of the water table in the area. From the differences in topographic elevation associated with the riverbed of the Yellow River, the recharge relationship and recharge rate between them are obtained. The two methods combine and complement each other to obtain important information such as distribution of underground strata, depth of water table, aquifer and permeability of rock and soil layer. The results of the two methods were in broad agreement, and were complementary, thus enabling satisfactory detection.

Moreover, the detection results show that the bottom of the overburden in the study area is the clay layer with poor permeability, and the thickness is generally more than 20m, which leads to very weak hydraulic connection between quaternary water system and bedrock fissure water. Therefore, the research scope of lateral seepage of the Yellow River is limited to the overburden. Finally, according to the obtained permeability coefficient and phreatic surface depth, it can be concluded that the Yellow River recharge groundwater, but the recharge rate is slow.

ACKNOWLEDGMENTS

Professor Pan Yuling is gratefully acknowledged for her valuable advice on the revision of the article.

REFERENCES

Davis, S. N., & De Wiest, R. J. 1966. Hydrogeology (Vol. 463). New York: Wiley.

Legchenko, A. V., & Shushakov, O. A. 1998. Inversion of surface NMR data. Geophysics, 63(1), p.75-84.

Lubczynski, M., & Roy, J. 2003. Hydrogeological interpretation and potential of the new magnetic resonance sounding (MRS) method. Journal of Hydrology, 283(1-4), p.19-40.

Roy, J., & Lubczynski, M. 2003. The magnetic resonance sounding technique and its use for groundwater investigations. Hydrogeology Journal, 11(4), p.455-465.

Bernard, J., & Legchenko, A. 2003. Groundwater exploration with the magnetic resonance sounding method. ASEG Extended Abstracts, 2003(2), p.1-5.

Hertrich, M., & Yaramanci, U. 2002. Joint inversion of surface nuclear magnetic resonance and vertical electrical sounding. Journal of Applied Geophysics, 50(1-2), p.179-191.

Legchenko, A., Baltassat, J. M., &Beauce, A. 2002. Nuclear magnetic resonance as a geophysical tool for hydrogeologists. Journal of Applied Geophysics, 50(1-2), p.21-46.

Lachassagne, P., Baltassat, J. M., Legchenko, A., & de Gramont, H. M. 2005. The links between MRS parameters and the hydrogeological parameters. Near Surface Geophysics, 3(4), p.259-265.

Lu, K., Li, Z., Niu, R., Li, F., Pan, J., Li, K., & Chen, L. 2020. Using surface nuclear magnetic resonance and spontaneous potential to investigate the source of water seepage in the JinDeng Temple grottoes, China. Journal of Cultural Heritage, 45, p.142-151.

Fetter, C. W. 2018. Applied hydrogeology. Waveland Press.

Lubczynski, M., & Roy, J. 2005. MRS contribution to hydrogeological system parametrization. Near surface geophysics, 3(3), p.131-139.

Daily, W., Ramirez, A., Binley, A., & LeBrecque, D. 2004. Electrical resistance tomography. The Leading Edge, 23(5), p.438-442.

Tso, C. H. M., Kuras, O., Wilkinson, P. B., Uhlemann, S., Chambers, J. E., Meldrum, P. I., ... & Binley, A. 2017. Improved characterisation and modelling of measurement errors in electrical resistivity tomography (ERT) surveys. Journal of Applied Geophysics, 146, p.103-119.

Legchenko, A., Clément, R., Garambois, S., Maury, E., Mic, L. M., Laurent, J. P., ... & Guyard, H. 2011. Investigating water distribution in the Luitel Lake peat bog using MRS, ERT and GPR. Near Surface Geophysics, 9(2), p.201-209.

Chrétien, M., Lataste, J. F., & Fabre, R. 2014. Electrical resistivity tomography to understand clay behavior during seasonal water content variations. Engineering geology, 169, p.112-123.

Descloitres, M., Ruiz, L., Sekhar, M., Legchenko, A., Braun, J. J., Mohan Kumar, M. S., & Subramanian, S. 2008. Characterization of seasonal local recharge using electrical resistivity tomography and magnetic resonance sounding. Hydrological Processes: An International Journal, 22(3), p.384-394.

Vouillamoz, J. M., Descloitres, M., Toe, G., & Legchenko, A. 2005. Characterization of crystalline basement aquifers with MRS: comparison with boreholes and pumping tests data in Burkina Faso. Near Surface Geophysics, 3(3), p.205-213.

Loke, M. H. 1999. Electrical imaging surveys for environmental and engineering studies. A practical guide to, 2, p.70.

Daily, W., Ramirez, A., LaBrecque, D., & Nitao, J. 1992. Electrical resistivity tomography of vadose water movement. Water Resources Research, 28(5), p.1429-1442.

The use of Surface Nuclear Magnetic Resonance to characterize the alluvium of the Er Mine in Kuche, China

[1]Kaitian Li [1]Fan Li [1]Kai Lu [1]Zhenyu Li

[1] China university of geosciences(Wuhan)
Wuhan, China
Email zhenyuli626@126.com

SUMMARY

Piedmont alluvium is poor in sorting and usually consists of sand and gravel of different sizes, sand and clay soil. The survey area is located in Er Mine, Kuche County, Xinjiang, China. The surface of the area is completely covered by quaternary sediments, mainly composed of alluvial and diluvial layers. The Surface Nuclear Magnetic Resonance (SNMR) method can investigate the water content in a certain depth and reveal the pore characteristics of the stratum. It is of great significance to investigate the hydrologic characteristics within 150m underground in this area for the safety construction of coal mine. The pore water in the vadose zone makes the Nuclear Magnetic Resonance (NMR) signal amplitude smaller. Coupled with the existence of environmental noise, one of the difficulties in detecting pore water is that NMR signals with a high Signal-to-noise ratio cannot be obtained. There is basically no human interference in the survey area, and the reference coil is used to obtain reliable NMR signals with a signal-to-noise ratio. Four Magnetic Resonance Sounding points are used to reveal the water-bearing characteristics of the strata and the differences in relaxation characteristics between weathered bedrock fissures and quaternary diluvial layers, providing important evidence for further hydrogeological research .

Key words: SNMR, Alluvium, Vadose zone.

INTRODUCTION

SNMR method is a geophysical technique that can directly reflect the occurrence of groundwater and reveal the hydrogeological parameters of the stratum. In various applications, SNMR method provides important evidence for researchers to comprehensively understand the formation. It is difficult to use MRS method to investigate low-porosity aquifers, which is mainly reflected in i) the small water volume of low-porosity aquifers (the average porosity of unweathered crystalline rocks is less than 5%), resulting in small NMR signal amplitude and low signal-to-noise ratio of the overall signal. ii) Magnetic inhomogeneity in igneous rock will produce a magnetic gradient that will result in a weakening of the effective NMR signal, the phreatic surface deep in the study area (beyond the detection range of MRS), The aquifer in the vadose zone was mainly detected, which is the upper stagnant water formed by the infiltration of atmospheric rainfall into the pore of the formation, uneven distribution, with the characteristics of the transverse discontinuity and uneven distribution. The attenuation process of NMR signal can be characterized by transverse relaxation time T_2, and its attenuation rate is related to the porosity of aquifer.

The study area(Figure 1b) is located about 2km southwest of Er Mine, Kuche County, Xinjiang, China, which belongs to the low and middle mountainous area. The terrain is fluctuated to some extent due to the cutting of valleys. The surface elevation is 1910±10m, but the slope is gentle enough to place the coil loop of MRS method. The surface of the study area is basically covered by quaternary sediments, which are mainly composed of alluvial and diluvial layers with poor sorting, interbedded with sand, gravel and clay, and the aquifer is dominated by pore water. The underlying bedrock is Jurassic sandstone and mudstone, and the structural fractures and weathered fractures are not evenly developed horizontally.

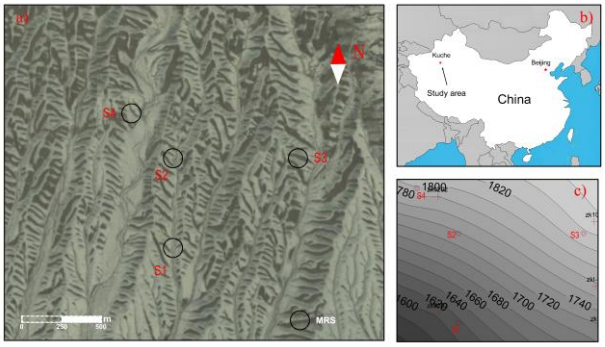

Figure 1. Satellite map and geographic location of the study area a) Satellite map of survey area and position of survey points. b) Geographical location of the study area. c) Contour map of quaternary floor in the study area

METHODS

The MRS uses the spin characteristics of hydrogen nucleus to detect groundwater. In the absence of an external magnetic field, the hydrogen nucleus precesses around the geomagnetic field B_0 at the Larmor frequency. The Larmor frequency is expressed as formula (1),

$$\omega_L = -\gamma_P |B_0| \qquad \text{eq. 1}$$

where γ_P is the magnetic rotation ratio, ω_L is the Larmor frequency, B_0 is the geomagnetic field.

A magnetic field B_1 will be generated in the underground when an alternating current is input to the surface coil at the Larmor frequency. Where the B_1 component perpendicular to the geomagnetic field, called B_2, that causes the hydrogen proton to deviate from B_0. When the current is cut off, the hydrogen protons will return to their original state, a process called relaxation. The macroscopic alternating magnetic field generated by the relaxation process will be received by the surface coil, and the received induced voltage is the Nuclear Magnetic Resonance (NMR) signal. It's represented by formula (2)

$$Signal(q,t)=\int_v \omega(r)\cdot K(q,r)\exp\left(-\frac{t}{T_2^*(r)}\right)\cdot dr^3 \qquad \text{eq. 2}$$

where $\omega(r)$ is the underground water content, r is the coordinate vector, $T_2^*(r)$ is the decaying time, $K(q,r)$ is the kernel function, which is the contribution of underground water per unit volume to the NMR signal, The kernel function is represented by formula (3)

$$K(q,r)=\frac{\omega_L}{I_0}B_2(r)e^{i\varphi_0(r)}M_\perp(q,r) \qquad \text{eq. 3}$$

where $B_2(r)$ is the excitation field component perpendicular to the geomagnetic field, $M_\perp(q,r)$ is the transverse component of spin magnetization, $\varphi_0(r)$ is the phase shift caused by the resistivity of the ground.

A total of four Magnetic Resonance Sounding points were arranged in this investigation. A coil with a single turn side length of 150m was used for self-excitation and self-collection, and a reference channel of 10m7 turns was used to improve the Signal-to-noise ratio of NMR signals. Each measuring point excited 16 pulse moments in a logarithmic distribution. Commercial software Samovar was used for data inversion

RESULTS

From the inversion results of the four points, both water content and T2 show certain changes. As can be seen from the water content histogram, the maximum water content of the four points is lower than 1%, and there are mainly two aquifers. The T2 distribution mainly ranges from 30ms to 240ms, and the relaxation time of 10-20m underground of the four sounding points is relatively short. The effective detection depth of S1 and S2 measuring points is located in the quaternary overburden layer. There is no regularity between T2 and pore water content, which may be caused by uneven distribution of gravity water. The T2 in the bedrock at S3 and S4 measurement points is 180ms and 35ms, respectively. The weathering degree of the bedrock and the lateral heterogeneity can lead to the difference.

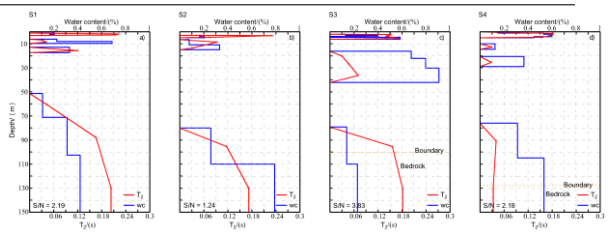

Fig. 2 Histogram of water content and T_2 distribution (the red line is water content changing with depth, the blue line is T_2 distribution, and the yellow dotted line is the boundary between quaternary and bedrock)

CONCLUSIONS

The low water content of pore water and bedrock fissure water in the Quaternary produced small NMR signals. Reasonable use of reference channel and small environmental noise in the study area also made it possible to collect useful signals. The study area is located to the north and the geomagnetic total field intensity is strong, which makes the NMR signal enhanced to a certain extent.

We found that the overall water content in the vadose zone was small, and the rainfall infiltration resulted in uneven distribution of gravity water, with T_2 ranging from 30ms to 240ms.The water content per unit volume in bedrock fissure is less than 0.2%-0.5%. T_2 is distributed between 30ms and 180ms and is mainly affected by weathering degree and weathering products filled by cracks.

ACKNOWLEDGMENTS

Thanks to Professor Yulin Pan for her valuable comments on this study. Thanks to CCTEG XI'AN RESEARCH INSTITUTE for providing the test site.

REFERENCES

Flinchum, B. A., W. S. Holbrook, A. D. Parsekian, and B. J. Carr. 2019. Characterizing the Critical Zone Using Borehole and Surface Nuclear Magnetic Resonance. *Vadose Zone Journal* 18 (1).DOI:10.2136/vzj2018.12.0209

Grunewald, E., and R. Knight. 2011. The effect of pore size and magnetic susceptibility on the surface NMR relaxation parameter T-2*. *Near Surface Geophysics* 9 (2):169-178.DOI:10.3997/1873-0604.2010062

Lange, G., O. Mohnke, and C. Grissemann. 2005. SNMR measurements in Thailand to investigate low-porosity aquifers. *Near Surface Geophysics* 3 (3):197-203.DOI:10.3997/1873-0604.2005014

Legchenko, A., and P. Valla. 1998. Processing of surface proton magnetic resonance signals using non-linear fitting. *Journal of Applied Geophysics* 39 (2):77-83.DOI:10.1016/s0926-9851(98)00011-1

Signal extraction of surface NMR steady-state free precession sequence data

[1]Lichao Liu [1]Denys Grombacher [2]Matthew P. Griffiths [1]Mathias Ø. Vang [2]Jakob Juul Larsen

[1] Department of Geoscience, Aarhus University
Høegh-Guldbergs Gade 2, 8000 Aarhus C, Denmark
Email lichao@geo.au.dk

[2] Department of Electrical and Computer Engineering, Aarhus University
Finlandsgade 22, 8200 Aarhus N, Denmark

SUMMARY

An efficient approach to mitigate the inherently low signal-to-noise ratio in surface NMR is applying steady-state free precession sequences, which consist of a train of same duration and phase-coherence pulses with a relatively short repetition time. However, a modified processing scheme is necessary to extract the signal from these long pulse trains. Here we outline an adaptation of spectral analysis to accomplish this task. The proposed method is efficient and obtains reliable signal from field data collected at different noise environments.

Key words: Surface NMR, steady state, spectral analysis.

INTRODUCTION

Surface NMR is a unique technique to study groundwater that provides meaningful insights into water content and pore-scale distribution [Legchenko et al., 2002]. However, surface NMR suffers from an extremely weak signal. Often a large number of stacks is required to obtain data with an adequate signal-to-noise ratio (SNR), which limits the number of sites that can be acquired in a day. By applying a steady-state free precession (SSFP) sequence in surface NMR, SNR can be improved over the same measurement time [Grombacher et al., 2021].

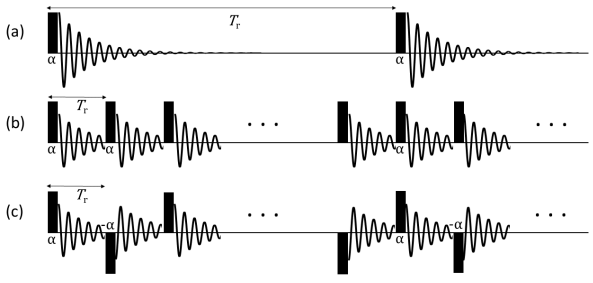

Figure 1. Steady-state free precession sequence measurement compared with FID sequence measurement. (a) FID measurement, (b) SSFP with constant flip angle and repetition time T_r, (c) SSFP sequence with alternating180◦phase and constant repetition time T_r.

In traditional free induction decay (FID) measurements, a waiting period of 3~5× the longitudinal relaxation time T_1 is typically allocated to allow for the perturbed magnetization to full re-establish its equilibrium before repeating the measurement. SSFP sequences, in contrast, have a repetition time T_r shorter than T_1 between fixed duration pulses (τ_p) (Fig. 1). Excitation pulses can be phase-coherent or of alternating polarity. When the former excitation pulse is terminated, NMR signal starts to relax for a short time ($T_r - \tau_p$) and will be perturbed by the next pulse again. After a few pulse sequences have been applied, both the longitudinal and transverse magnetization will be in dynamic equilibrium, which is referred to as steady-state.

In order to maintain phase coherency of the NMR signal after each pulse, repetition time is designed as,

$$T_r = \frac{k_1}{f_L} \text{ and } k_1 \in \mathbb{Z}, \qquad \text{eq.1}$$

where f_L is the Larmor frequency. The minimum T_r has the following constraints: 1) Required pulse length for aimed investigation depth. 2) Sufficient signal relaxation time to characterize pore size. 3) Recharge time for power bank and heat dissipation efficiency of transmitter.

In order to perform SSFP measurements, the HydroGeophysics Group at Aarhus University has continued to develop their surface NMR system APSU [Liu et al., 2019a; Larsen et al., 2020]. These improvements to APSU are: 1) Transmitting repetition time can be configured as low as 10 ms with a resolution of 1 µs. 2) Receiver channels record continuous data beginning with the first pulse. A protection circuit clips the receiver channel during excitation pulses to prevent damage to the hardware. Typical repetition time of SSFP sequence for APSU system is about 50 to 200 ms. Hence, approximately 20 ~ 100 times of SSFP signal can be recorded in one FID sequence time.

METHODS

The repetitive and continuous nature of SSFP measurements means that zeroing out the pulses is an essential step prior to applying spectral analysis. This is because even the clipped pulses still dominate the energy of recordings and make it impossible to estimate NMR spectrum. In practice, windowing is applied on concatenated data. In addition to zeroing pulses, the signal part is multiplied by ±1 , where the sign is determined by pulse phase α or -α.

Signal recorded with constant-phase SSFP sequence is the combination of signals after each pulse,

$$ss(t) = \sum_0^{N-1} s(t - nT_r), \qquad \text{eq.2}$$

and $s(t)$ is the NMR signal in the first window. In homogeneous background fields, it can be viewed as an FID signal multiplied by a rectangular window function

$$s(t) = s_0 e^{-\frac{t}{T_2}} \cos(2\pi f_L t + \varphi) \cdot \mathrm{rect}(\frac{t}{T_r - \tau_p}), \quad \text{eq.3}$$

where s_0, T_2, φ are the initial amplitude, transverse relaxation time, and initial phase respectively. The spectrum of $s(t)$ is equivalent to the convolution of two Fourier transforms,

$$S(f) = S_{\mathrm{NMR}}(f) * S_w, \text{ and}$$

$$S_{\mathrm{NMR}}(f) = e^{j\varphi} \frac{\frac{1}{T_2} + j2\pi(f - f_L)}{(\frac{1}{T_2})^2 + 4\pi^2(f - f_L)^2},$$

$$S_w = 2(T_r - \tau_p) \cdot \mathrm{sinc}\{2(T_r - \tau_p) \cdot f\}. \quad \text{eq.4}$$

After Fourier transformation of eq. 2, constant-phase SSFP signal spectrum is

$$SS(f) = \begin{cases} S(f) \cdot N, \text{when } f = \frac{k_2}{T_r} \text{and } k_2 \in \mathbb{Z}, \\ S(f) \cdot \frac{1 - e^{-j2N\pi f T_r}}{1 - e^{-j2\pi f T_r}}, \text{otherwise.} \end{cases} \quad \text{eq.5}$$

This equation highlights that $SS(f)$ is simply the single window Fourier transform multiplied by a factor that can be recognized as a periodic sinc function. This function resembles a comb function with peaks occurring at integer multiples of $1/T_r$, and other frequencies have relatively low spectra which is close to zero. The peak width is controlled by NT_r, with larger NT_r leading to a narrower peak. Spectra at f_L is magnified by a factor of N compared to that in a single window. Figure 2 shows the spectra of a single-window signal $s(t)$ and the concatenated data $ss(t)$. They are computed from synthetic signal using FFT and verifies eq. 5.

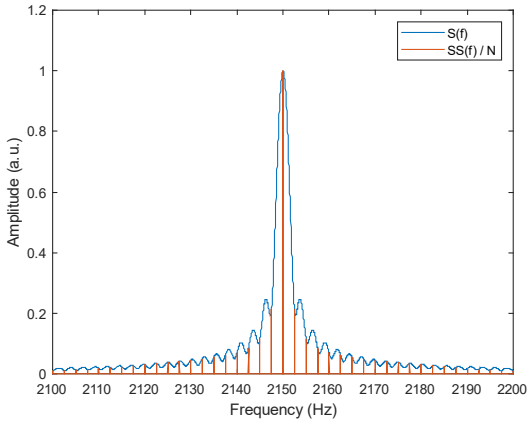

Figure 2. Spectra of single-windowed signal $s(t)$ (blue) and the concatenated data $ss(t)$ (red). In the synthetic model, f_L = 2150 Hz, T_r = 0.4 s, T_2 = 0.3 s, and τ_p = 0.02 s.

After being normalized by N, the peak value of $SS(f)$ coincides with the value of $S(f)$. This comb function is responsible for the narrowing of the spectra. Note that this collapsing behaviour does not mean that the full-bandwidth of the NMR signal cannot be measured – instead the full-bandwidth of the signal is projected into the narrow peak.

The spectra at f_L can be obtained with DFT after windowing the data. As in the spectral analysis method applied to FID data [Liu et al., 2019b], a decay curve can be extracted by sliding the start of non-zero window from the early part of the signal to the later part while the end of non-zero window keeps unchanged, as in Fig. 3.

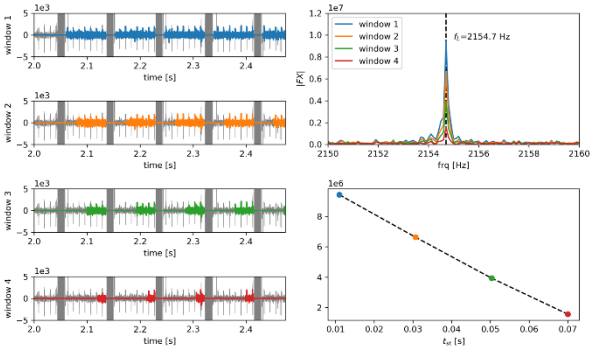

Figure 3. Illustration of spectral analysis method extracts SSFP signal by using Fourier transform and sliding window. The left panel shows the waveforms before and after windowing using 4 different start time. Right-top panel shows the corresponding spectrograms, the dash line indicates the Larmor frequency. Right-bottom shown the extracted decay curve of SSFP signal.

SSFP sounding curves are formed by taking the DFT at the transmit frequency of the concatenated windowed time series for each pulse moment. The FID sounding curves are formed from the DFT of the stacked 1 s timeseries at the estimated Larmor frequency.

CONCLUSIONS

Spectral analysis is used to the extract signal from SSFP data. SSFP signal spectra has a comb shape with peaks located at integer times of repetition frequency and its value is the spectra of a single-windowed NMR signal multiples with repetition number.

ACKNOWLEDGMENTS

The research is funded by Independent Research Fund Denmark and Velux Foundations.

REFERENCES

Legchenko A., J.-M. Baltassat, A. Beauce, & J. Bernard. 2002. Nuclear magnetic resonance as a geophysical tool for hydrogeologists: Journal of Applied Geophysics, 50, 21–46.

Grombacher D., Liu, L., Griffiths M.P., Vang M.Ø. & Larsen J.J. 2021. Steady-state surface NMR for mapping of groundwater, submitted to Geophysical Research Letters.

Liu L., D. Grombacher, E. Auken & J. J. Larsen, 2019a, Apsu: a wireless multichannel receiver systemfor surface-NMR groundwater investigations: Geoscientific Instrumentation, Methods and Data Systems, 8, 1–11.

Larsen J. J., L. Liu, D. Grombacher, G. Osterman & E. Auken. 2020. Apsu—a new compact surface nuclearmagnetic resonance system for groundwater investigation: Geophysics, 85, JM1–JM11.

Liu L., D. Grombacher, E. Auken & J. J. Larsen, 2019b, Complex envelope retrieval for surface nu-clear magnetic resonance data using spectral analysis:Geophysical Journal International,217, 894–905.

Application of BEL1D for sNMR data interpretation

[1]H. Michel
[1] ULiège, UGent, F.R.S-FNRS
Liège, Belgium
hadrien.michel@uliege.be

[2]T. Hermans
[2] UGent
Gent, Belgium
thomas.hermans@ugent.be

[3]T. Kremer
[3] ULiège, UNantes
Nantes, France
thomas.kremer@unantes.fr

[4]F. Nguyen
[4] ULiège
Liège, Belgium
f.nguyen@uliege.be

SUMMARY

The interpretation of sNMR data is still mainly performed using deterministic or stochastic inversion schemes. sNMR signal to noise ratio is often low regarding electromagnetic noise pollution which coupled to non-uniqueness makes uncertainty quantification challenging. Here, we propose a new Bayesian scheme relying on a learning step and a prediction step to perform the interpretation of sNMR data including uncertainty quantification: BEL1D. With it, it is possible to estimate the uncertainty of models parameters from a given dataset in a rapid manner compared to stochastic inversion and reach an equivalent posterior estimation after iterative prior resampling. The learning step can even be used to multiple datasets to improve performances with only the prediction required. Additionally, BEL1D could be used with any geophysical methods.

Key words: Inversion, Machine Learning, MCMc, Uncertainty, BEL.

INTRODUCTION

Inversion in sNMR is often performed using a deterministic scheme (e.g.: Legchenko & Shushakov, 1998; Legchenko & Valla, 2002; Mueller-Petke & Yaramanci, 2010). Those schemes based on linear (or linearized) inversion offer the advantage to be rapid and provide the user with a single model to interpret. However, the obtained model represents the most-likely model in the least-squared sense. Even if they are likely close to the actual geological model, uncertainty quantification is still lacking. Propagating data uncertainty through the covariance matrix is a cost-effective solution (Tarantola & Valette, 1982). However, using such approach will only represent the propagation of the data uncertainty and not encompass the modelling uncertainty.

Appraisal of uncertainty in geophysical inverse modelling is key to an efficient decision-making process (Scheidt *et al.*, 2018). In sNMR, Andersen *et al.* (2018) proved that the solution to the inverse problem showed large uncertainties, and even sometimes water-content/thicknesses correlations. They showed that only a Markov chain Monte Carlo (McMC) approach was suitable for a reasonable estimation that was able to collect all the features of the uncertainty with correlation between models parameters. However, they stated that using an MCMc approach was approximately 1000 times slower than propagating the covariance matrix in the linearized inversion.

We propose another method to solve the inverse problem and estimate the uncertainty that simplifies the Bayesian problem in a reduced space to speed-up calculations. This method, based on Bayesian Evidential Learning (BEL – Scheidt *et al.*, 2018), is well suited for the 1D imaging of the subsurface from geophysical data and called BEL1D (Michel *et al.*, 2020). In previous works (Michel *et al.*, 2020), we demonstrated that BEL1D was efficient, fast and reliable. However, the uncertainty resulting from this approach was slightly overestimated. Here, we propose the use of Iterative Prior Resampling in order to solve this issue.

METHODS

BEL1D (or Bayesian Evidential Learning 1D imaging) is an adaptation of Bayesian Evidential Learning (BEL – Scheidt *et al.*, 2018) for the direct prediction of 1D models parameters based on geophysical data. This implementation of BEL differs thus in the way the end-result is the models and not a parameter of interest that could be obtained through petrophysics (for example).

The algorithm is simplifying the Bayesian problem in a reduced space. It is described extensively in Michel *et al.* (2020) and can be summarized in 7 steps:

1) Define the prior model space ($f(\boldsymbol{m})$) and sample N models ($\boldsymbol{m}$) out of it.

2) Use the forward model (eq. 1) to obtain the response for each of the N models.

$$\boldsymbol{d} = G(\boldsymbol{m}) \quad \text{(eq. 1)}$$

3) If required, reduce the dimensionality of the models and the related data using principal component analysis (PCA) (eq. 2 and eq. 3).

$$PCA(\boldsymbol{d}) \xrightarrow{yields} \boldsymbol{d^f} \quad \text{(eq. 2)}$$

$$PCA(\boldsymbol{m}) \xrightarrow{yields} \boldsymbol{m^f} \quad \text{(eq. 3)}$$

4) Use canonical correlation analysis (CCA) to obtain a statistical relationship between $\boldsymbol{d^f}$ and $\boldsymbol{m^f}$ (eq. 4).

$$CCA(\boldsymbol{d^f}, \boldsymbol{m^f}) \xrightarrow{yields} (\boldsymbol{d^c}, \boldsymbol{m^c}) \quad \text{(eq. 4)}$$

5) In the reduced space, approximate the posterior distribution of $\boldsymbol{m^c}$ using kernel density estimation (KDE) for any $\boldsymbol{d^c}$ (eq. 5).

$$KDE(\boldsymbol{d^c}, \boldsymbol{m^c}) \xrightarrow{yields} f(\boldsymbol{m^c}|\boldsymbol{d^c}) \quad \text{(eq. 5)}$$

6) Apply the PCA and CCA transformations to the field dataset ($\boldsymbol{d_{obs}}$) (eq. 6)

$$CCA\big(PCA(\boldsymbol{d_{obs}})\big) \xrightarrow{yields} \boldsymbol{d^c_{obs}} \quad \text{(eq.6)}$$

7) Sample models from the posterior distribution $\boldsymbol{m}^c_{post} \in f(\boldsymbol{m}^c|\boldsymbol{d}^c_{obs})$. Each model can be back transformed to the original space (PCA and CCA are both linear transformations).

One of the main advantage of this method is that the field data is only necessary from step 6 onward. Therefore, one can see BEL1D as a machine learning algorithm, where the training consists of describing the Bayesian problem in the reduced space and the interference step is the process of extracting the posterior model space for a new dataset. This makes for extremely fast posterior estimation.

We introduce **Iterative Prior Resampling (IPR)** as an efficient way to converge towards the posterior similar to the one obtained by classical MCMc approaches. IPR is inspired from iterative spatial resampling (Mariethoz *et al.*, 2010). Algorithmically, we are adding the models sampled from the posterior to the prior to re-train BEL1D on a more informed prior. This approach enable to overcome issues with large prior uncertainties that result in difficulties to extract trends between data and models.

RESULTS

In this section, we will discuss some results that we obtained using this approach. We will apply BEL1D to a synthetic dataset created using MRSMatlab (Mueller-Petke *et al.*, 2016). We will use a large prior to force the demonstration that it is rather difficult to converge when very few is known in advance regarding the model.

Table 1: Description of the benchmark model and associated prior

Layer #	e_i [m]			W_i [%]			$T^*_{2,i}$ [ms]		
	Min	True	Max	Min	True	Max	Min	True	Max
1	1	25	50	1	5	50	5	100	500
2	1	25	50	1	25	50	5	200	500
H-S	/	Inf	/	1	10	50	5	50	500

The benchmark model along with the used prior is presented in Table 1. The dataset is simulated using a classical transmitter/receiver configuration with a 50 m diameter. The sampling frequency is 500Hz from 0.005 seconds to 0.5 seconds. The prior is barely informative, apart from the input knowledge that three layers can describe accurately the model. By design, the prior has zones where the dataset cannot be sensitive to the data; hence, it makes estimations of uncertainty even more complex.

Results after one iteration

Let us first analyse the results obtained at the first iteration. Since the prior uncertainty is rather large, BEL1D is facing difficulties to retrieve an efficient correlation between the models and the simulated data. However, we are still able to reduce significantly the uncertainty on most of the parameters (*Figure 1*).

From the results at the first iteration, we already see that we are mostly sensitive to the water contents. Then, the relaxation times and, finally, the layers thicknesses are the least sensitive parameters in this configuration. As is also expected, the first layer shows a higher uncertainty reduction at the first iteration for both the water content and relaxation time than the other parameters. This is due to the higher sensitivity of the experiment to this layer.

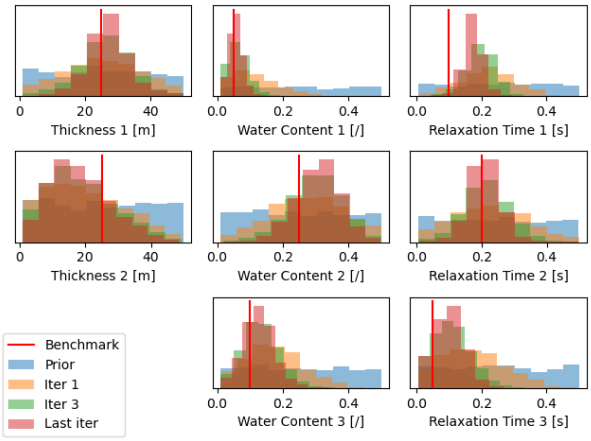

Figure 1: Results obtained from BEL1D with IPR. This graph presents the obtained distributions independently, but the parameter space is explored jointly in BEL1D.

Results after applying IPR

When applying IPR, we are using the information from the previous iterations to better constrain the prior. This leads to a more coherent reduction of uncertainty. Observing the results of the 3rd and 7th (last) iterations (*Figure 1*), we see that the obtained distributions tend towards a more accurate posterior. Nonetheless, some parameters are still lacking sensitivity. This is the case for the relaxation time of the first layer, where the low water content hides this parameter.

If we analyse the correlation between the model's parameters (*Figure 3*), we observe that there is a correlation between the water content of the second layer and its thickness. This result is corroborated by the distributions of the total water content (*Figure 2*). There, we observe that, even though the uncertainty on the water content and the thicknesses remains large, we reduce significantly the total water content.

In this figure, we also propose a comparison between (1) the results from BEL1D with correlation between parameters taken into account and (2) random sampling of the distributions obtained through BEL1D in order to lose the parameters correlations. We see that the correlation that exists inherently between the parameters is crucial to the model estimation.

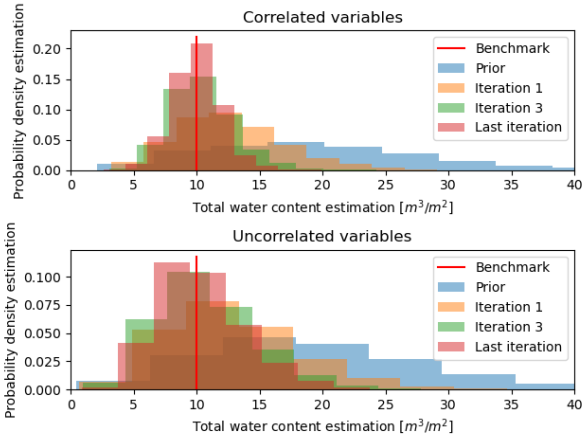

Figure 2: Total water content estimation. The estimation is performed for the correlated case (top – results from BEL1D) and simulated for the uncorrelated case (bottom).

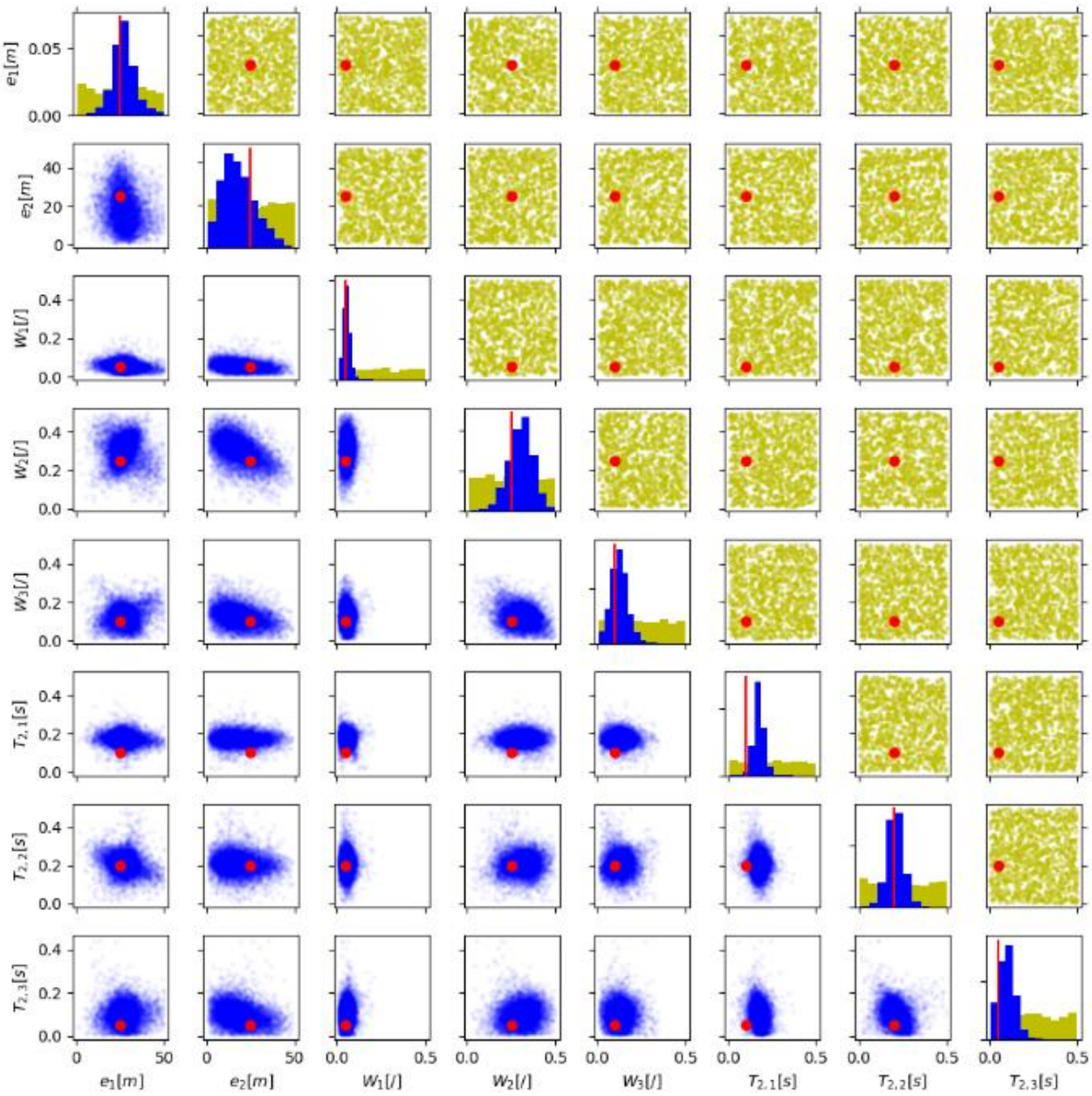

Figure 3: Illustration of the posterior model space after applying BEL1D with IPR. The yellow distributions are the prior and the blue distributions are the posterior after seven iterations of BEL1D.

Finally, we observe that the gain of the latest iterations is marginal. Knowing that the latest iterations are also the ones that are the longest to compute (more models in the informed prior), a user that is interested in a rapid but not especially precise estimation of the uncertainty could use three iterations to gain rapid insight on the uncertainty.

CONCLUSIONS

BEL1D is a new algorithm that can be used to interpret sNMR data in a Bayesian framework. We showed that BEL1D was able to recover reasonable uncertainties, even from large prior model spaces. Moreover, compared to a deterministic scheme with propagation of the uncertainty through linear(ized) inversion (Tarantola & Valette, 1982), BEL1D is able to provide insight on the full behaviour of the posterior, with correlations between the different parameters. This latter is a key aspect as it reduces the uncertainty of joint parameters as well.

Using BEL1D on its own provides a coarse estimation of the uncertainty (especially when dealing with large priors) but can already extract tendencies in the posterior. This iteration is basically free, as the training can be performed prior to any knowledge of the data characteristics. Then, using IPR enables a more precise and accurate estimation of the uncertainty, but this approaches requires CPU time. Using few iterations can already provide a reasonable uncertainty at a reasonable CPU cost. Depending on the degree of precision required, the user could use only those few iterations.

ACKNOWLEDGMENTS

Hadrien MICHEL is a Research Fellow of the *Fonds de la Recherche Scientifique – FNRS*.

REFERENCES

Legchenko, A., & Shushakov, O. 1998. Inversion of NMR data. Geophysics, 63(1), p.75-84.

Legchenko, A., & Valla, P. (2002). A review of the basic principles for proton magnetic resonance sounding measurements. Journal of Applied Geophysics, 50(1–2), p.3–19.

Mueller-Petke, M., & Yaramanci, U. (2010). QT inversion — Comprehensive use of the complete surface NMR data setQT inversion. Geophysics, 75(4), p.WA199–WA209.

Tarantola, A., & Valette, B. (1982). Generalized Nonlinear Inverse Problems Solved Using the Least Squares Criterion. Reviews of Geophysics and Space Physics, 20(2), 219–232.

Scheidt, C., Li, L., & Caers, J. (2018). Quantifying Uncertainty in Subsurface Systems.

Andersen, K. R., Wan, L., Grombacher, D., Lin, T., & Auken, E. (2018). Studies of parameter correlations in surface NMR using the Markov chain Monte Carlo method. Near Surface Geophysics, 16(2), p.206–217.

Michel, H., Nguyen, F., Kremer, T., Elen, A., & Hermans, T. (2020). 1D geological imaging of the subsurface from geophysical data with Bayesian Evidential Learning. Computers and Geosciences, 138, p.104456.

Mariethoz, G., Renard, P., & Caers, J. (2010). Bayesian inverse problem and optimization with iterative spatial resampling. *Water Resources Research*, *46*(11), p.11530.

Müller-Petke, M., Braun, M., Hertrich, M., Costabel, S., & Walbrecker, J. (2016). MRSmatlab — A software tool for processing, modeling, and inversion of magnetic resonance sounding data. Geophysics, 81(4), p.WB9–WB21.

State-of-the-art and progress using prepolarization for surface Nuclear-Magnetic-Resonance

[1]Mike Müller-Petke, [1,2]Thomas Hiller, [2]Stephan Costabel, [2]Raphael Dlugosch, [3]Ronny Stolz

[1] Leibniz Institute for Applied Geophysics, Hannover, Germany
[2] Federal Institute for Geosciences and Natural Resources, Germany
[3] Leibniz Institute for Photonic Technologies; Jena, Germany

SUMMARY

Detecting the presence and investigating the spatial variability of water in the subsurface is of increasing interest at the very shallow scale and demands a high spatial resolution. However, the application of the surface-NMR technique to this demand includes using small loops sizes and therefore is strongly limited by low signal strengths and consequently low signal-to-noise ratios. A promising approach to tackle this limiting fact is applying the prepolarization technique known from NMR laboratory equipment. It allows for significantly increasing the signal strength at depths down to about 1 m and thus, enables successful field measurements. Our recent research shows that (i) spin-dynamics needs to be carefully considered during the forward modelling, (ii) point-like B-field receiver can be applied enabling three-component registrations, (iii) prepolarization fields can be achieved either using common copper coils or recently developed superconducting coils and (iv) advanced noise cancellation techniques can further improve the data quality.

Key words: small-scale, prepolarization, spin-dynamics.

INTRODUCTION

The technique of surface nuclear magnetic resonance (SNMR) has been originally developed and is still commonly applied for the detection of water in the saturated zone, i.e. aquifers, and the hydraulic characterization of aquifers. However, the technique gained interest for investigating the unsaturated zone and corresponding water dynamics (e.g. Costabel and Günther, 2014; Walsh et al., 2014, Legchenko et al., 2020). In this context, enabling high lateral resolution for shallow soil water investigations would be of great use. Furthermore, small coils sizes are a demand when applying SNMR in underground mining conditions (Costabel 2019, Yi et al, 2018). Unfortunately, using the demanded small coils results in low signal strength and consequently a poor signal-to-noise ratio.

To overcome this limitations, de Pasquale and Mohnke (2014) adapted the concepts of prepolarization (PP) known from Earth's field laboratory scale experiments (e.g. Callaghan et al., 1997) for SNMR and presented a first theoretical study. The key idea is to include a strong artificial magnetic field (named the PP field) into the pulse sequence (Figure 1). This PP increases the spin magnetization and thus increases the detected signal strength.

Meanwhile, the idea has been picked up and promising measurements have been conducted that provide an experimental proof of the PP concept (Lin et al., 2018, Hiller et al., 2021a). With this experimental evidence, research on the fundamentals of surface Nuclear-Magnetic-Resonance using prepolarization (SNMR-PP) was triggered and an overview on this research is provided in the following.

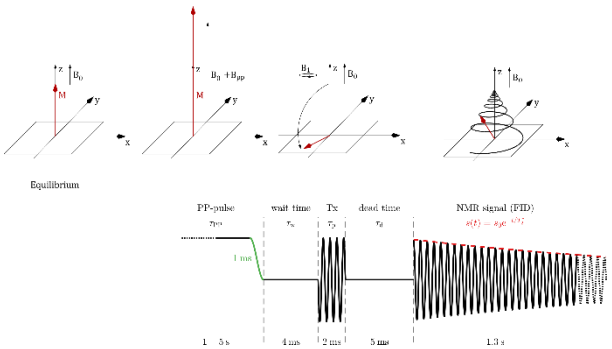

Figure 1: Sketch of a simple pulse sequence using a pre-polarization field $\mathbf{B_{PP}}$ *to increase the spin magnetization* $\mathbf{M}$.

MODELING OF THE SPIN-DYNAMICS

While de Pasquale and Mohnke (2014) started accounting for the PP field by simply increasing the spin magnetization assuming perfect adiabatic conditions, it is very unlikely that this maximum amplification throughout the entire subsurface is realistic when considering a true ramp-down of the PP fields (e.g. Conradi et al., 2017). Hiller et al. (2020) studied the impact of different PP-ramps (shapes and ramp-down times) on the magnetization achieved in the subsurface by solving the underlying Bloch Equation and provided the software BLOCHUS (Bloch Universal Simulator - https://github.com/ThoHiller/nmr-blochus) to the SNMR community. Considering ramp-downs, one should keep in mind the trade-off between a fast ramp-down to be able to measure fast relaxing signals and a slow ramp-down to achieve a maximum of adiabatic quality throughout the volume. As Hiller et al. (2020) demonstrate, different realistic and feasible ramp-downs produce significant differences regarding the response signal strength that must not be neglected. Furthermore, they concluded that a general optimum of the ramp-down shape and timing is difficult to

find and suggest including the modelling of the applied PP-ramps in any case.

Beyond modelling the PP-ramps, we recently found that modelling the pulse-shapes might also be necessary in some cases to explain the measured data (Hiller et al., 2021b).

THREE-COMPONENT COMPACT B-FIELD RECEIVER

When considering high lateral resolution, one can almost naturally think of using point-like receivers spread along a profile or distributed in the area of interest, instead of placing a number surface loops. Davis et al. (2014) published first successful measurements detecting SNMR signals using compact B-field sensors. The advantage of compact B-field sensors is twofold. On the one hand, one may place several sensors and gain spatial resolution, while on the other hand they allow for detecting all three components of the B-field and therefore likely gain additional information due to their different spatial sensitivities. In addition, they can be used as compact easy to move reference coils for noise cancelation. We have conducted the first successful measurements (Figure 2) detecting SNMR-PP signals in all three components. While using a SQUID as detection sensor, a compact B-field coil sensor was used for noise compensation and placed a few meters apart. We expect that with the ongoing development of magnetic field sensors (SQUIDs, optical pumped magnetometers or specialized copper coils) with the necessary high precision in the range of pico-Tesla, the use of these sensors for high-resolution datasets will be an interesting and innovative field.

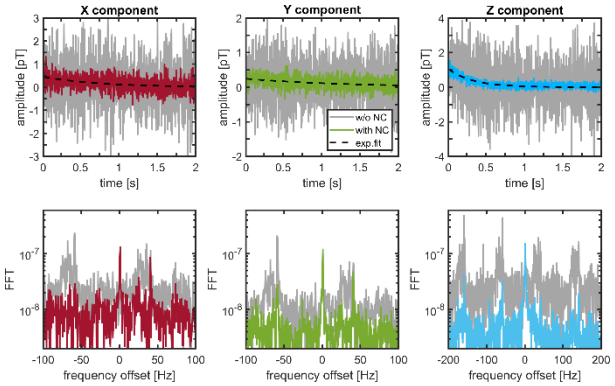

Figure 2: NMR signals detected with a three-component SQUID (top row) and corresponding frequency spectra (bottom row). We used a compact B-field coil placed a few meters apart for noise compensation.

PREPOLARIZATIONS COILS

Obviously, the key behind SNMR-PP is achieving a strong artificial B-field for several seconds by running a direct current through a loop and ramp-down the current in an appropriate time. This can be achieved by a loop laid out using a copper wire. Current systems achieve effective currents of about 1000 A using multi-turn loops. Ramp-down times realized are in the order of 1 - 4 ms using appropriate electronics (Conradi et al., 2017, Lin et al., 2018).

A different approach is constructing the PP-coil from superconducting material. This likely allows for a significant increase in current amplitude, PP-field strength and thus detected signal strength. A first prototype (Figure 3) of a superconducting loop has been constructed by the IPHT Jena allowing for currents up to 5000 A. An increase of a factor of 5 DC results in a signal amplification of about 4.5 (Figure 4). Note, with increasing PP-field strength, considering the ramp-shape becomes even more important.

Figure 3: First laboratory prototype of a superconducting PP-coil.

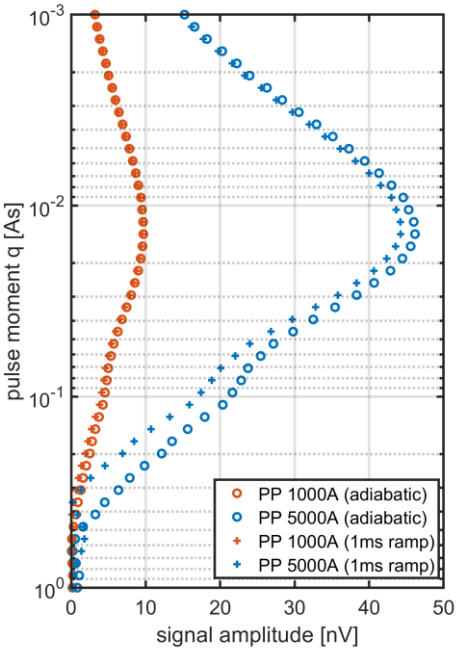

Figure 4: Sounding curve above a half-space of water. PP-coil diameter is 2 m, Tx/Rx coils are 1 m and centred in the PP-coil.

ADVANCED NOISE CANCELATION

Even though prepolarization significantly increases the signal strength, it is still necessary and of advantage to reduce the level of environmental noise. In principle, the common SNMR processing concepts (stacking, harmonic filter, remote noise cancellation or figure-of-eight) can be applied. However, in detail new possibilities and challenges that demand adaptation arise. Costabel et al. (2019) showed that the use of a multi-component antenna is beneficial if noise sources are close. However, when considering a moving sensor, an additional multi-component noise antenna is impractical. Therefore, a figure-of-eight (FOE) is interesting but again the necessary

orientation of the FOE in order to achieve good noise cancellation is difficult when the sensor changes the direction along a profile. Consequently, adapting the FOE concept for these requirements is necessary.

CONCLUSIONS

Surface nuclear-magnetic-resonance using prepolarization (SNMR-PP) shows great potential in measuring near surface water in soil, the unsaturated zone or in underground conditions. Along with the prepolarization, several fields of research must be addressed to develop the technique further. To achieve reliable results accurate modelling of the spin dynamics is most necessary while the development of high current coils, compact B-field receiver or advanced noise cancellation approaches will help to enhance spatial resolution and signal quality.

REFERENCES

Callaghan, P.T., Eccles, C.D. & Seymour, J.D., 1997. An earth's field nuclear magnetic resonance apparatus suitable for pulsed gradient spin echo measurements of self-diffusion under Antarctic conditions, Rev. Sci. Instrum., 68(11), 4263–4270.

Costabel, S. & Günther, T. 2014. Noninvasive Estimation of Water Retention Parameters by Observing the Capillary Fringe with Magnetic Resonance Sounding. Vadose Zone Journal, 13, 1–14.

Costabel, S. 2019. Noise analysis and cancellation for the underground application of magnetic resonance using a multi-component reference antenna – Case study from the rock laboratory of Mont Terri, Switzerland. Journal of Applied Geophysics, 169, 85–97.

Conradi, M.S., Altobelli, S.A., Sowko, N.J., Conradi, S.H. & Fukushima, E., 2017. Pre-polarization fields for earth's field NMR: Fast discharge for use with short T1 and large coils, J. Magnet. Reson., 281(Supplement C), 241–245.

Davis, A. C., Dlugosch, R., Queitsch, M., Macnae, J. C., Stolz, R., & Müller-Petke, M., 2014. First evidence of detecting surface nuclear magnetic resonance signals using a compact B - field sensor. Geophysical Research Letters, 41(12), 4222-4229.

De Pasquale, G., & Mohnke, O., 2014. Numerical study of prepolarized surface nuclear magnetic resonance in the vadose zone. Vadose Zone Journal 13, 1-9.

Hiller, T., Dlugosch, R., & Müller-Petke, M., 2020. Utilizing pre-polarization to enhance SNMR signals - effect of imperfect switch-off. Geophysical Journal International, 222(2), 815-826.

Hiller, T., Costabel, S., Radić, T., Dlugosch, R., & Müller-Petke, M., 2021. Feasibility study on prepolarized surface nuclear magnetic resonance for soil moisture measurements. Vadose Zone Journal, e20138.

Hiller, T., Costabel, S., Dlugosch, R., & Müller-Petke, M., 2021b. Accounting for the excitation pulse shape in modelling prepolarized surface nuclear magnetic resonance (SNMR-PP). Submitted to the 8th International Workshop on Magnetic Resonance, Strasbourg, France.

Legchenko, A., Baltassat, J.-M., Duwig, C., Boucher, M., Girard, J.-F., Soruco, A., Beauce, A., Mathieu, F., Legout, C., Descloitres, M. & Gabriela Patricia, F. A. 2020. Time-lapse magnetic resonance sounding measurements for numerical modeling of water flow in variably saturated media. Journal of Applied Geophysics, 175, 103984.

Lin, T., Zhou, K., He, C., Wang, P., Zhang, Y. & Xu, Y. 2018. Analysis and design of the transmitting mode on the pre-polarization surface nuclear magnetic resonance system. Review of Scientific Instruments, 89(12), 125102.

Walsh, D. O., Grunewald, E. D., Turner, P., Hinnell, A. & Ferre, T. P. A. 2014. Surface NMR instrumentation and methods for detecting and characterizing water in the vadose zone. Near Surface Geophysics, 12, 271–284.

Yi, X., Zhang, J., Fan, T., Tian, B. & Jiang, C. 2018. Design of meter-scale antenna and signal detection system for underground magnetic resonance sounding in mines. Sensors, 18(3), 848.

Heat exchange impact on NMR logging while drilling

[1, 2] Oleg A. Shushakov, [3] Oleg B. Bocharov, [4] Radu Coman, [4] Holger F. Thern
[1] Voevodsky Institute of Chemical Kinetics and Combustion, SB RAS, 3 Institutskaya str., 630090 Novosibirsk, Russia
[2] Novosibirsk State University, 1 Pirogova str., 630090 Novosibirsk, Russia
[3] Baker Hughes Russia, Novosibirsk Technology Center, 4a, Kutateladze St., 630090 Novosibirsk, Russia
[4] Baker Hughes,, Celle Technology Center, 1 Baker-Hughes Strasse, 29221 Celle, Germany

Email shushako@kinetics.nsc.ru

SUMMARY

The effect of temperature on nuclear magnetic resonance (NMR) logging while drilling (LWD) has been studied. Heat conduction and permeability effects in the near wellbore invasion zone have been taken into account. Analytical solutions and numerical calculations have been exemplified and verified with the use of NMR LWD field data.

Key words: NMR logging while drilling, heat transfer effect, permeability effect.

INTRODUCTION

Temperature affects nuclear magnetic resonance measurements in the well. Both nuclear spin magnetization and NMR signal are inversely proportional to absolute temperature (Curie-Langevin law). In the magnetic field $\vec{B}_0$ a macroscopic magnetization $\vec{M}_0(\vec{r})$ of a unit volume in thermal equilibrium state is described by the equation [Abragam, 1961]:

$$\vec{M}_0(\vec{r}) = n(\vec{r})\frac{\gamma^2\hbar^2}{3kT}S(S+1)\cdot\vec{B}_0,$$

where $n(\vec{r})$ is the number of magnetic nuclei per unit volume, γ is gyromagnetic ratio and S=1/2 is the nuclear spin for protons, $\hbar$ and k are Planck and Boltzmann constants, respectively, and T is an absolute formation temperature.

Modern wells are very long and have considerable temperature differences in length. In both wireline NMR logging and NMR logging while drilling (LWD) the measured mud temperature on signed level used as a proxy temperature of NMR sensitive volume situated in several centimetres deep into formation from borehole surface. In NMR LWD the temperature of mud and formation could be different in contrast to wireline NMR logging. This can reduce the accuracy of determined by NMR porosities. In MMR LWD temperature correction is not yet in standard use [Prammerr et al., 2000].

For NMR logging while drilling temperature correction, we have to estimate the temperature in the NMR sensitive volume, which is situated in several centimeters from borehole wall deep into formation [Coman, Tietjen, 2017].

RESULTS

A HEAT CONDUCTION WITH MUD FILTRATION MODEL

A heat conduction equation considering mud invasion is $\frac{\partial T}{\partial t} = div\left(D_T \cdot gradT - \vec{v}\cdot T\right)$, where $\vec{v}$ is mud filtration rate. In cylindrical coordinate frame for constant radial flux $\vec{v} = \frac{v_0 \cdot a}{r}\cdot\vec{e}_r$ (v_0 = const is the filtration flow rate at $r=a$, a is the borehole radius, $\vec{e}_r$ is the unit vector along radius r). For dimensionless $\tau_T = D_T\, t/a^2$ and $\rho = r/a$, and $\beta = v_0 a/2D_T$

$$\frac{\partial T}{\partial \tau_T} = \frac{\partial^2 T}{\partial \rho^2} + \frac{1-2\beta}{\rho}\cdot\frac{\partial T}{\partial \rho},$$

For constant initial and boundary conditions $\begin{cases} T(\tau_T,1) = T_1 \\ T(0,\rho) = T_0 \end{cases}$, the solution for $\rho > 1$ and $\tau_T > 0$ is [Carslaw, Jaeger, 1959]

$$\frac{T-T_0}{T_1-T_0} = 1 + \frac{2\rho^\beta}{\pi}\int_0^\infty exp(-\tau_T u^2)\cdot\frac{J_\beta(u\rho)\cdot Y_\beta(u) - Y_\beta(u\rho)\cdot J_\beta(u)}{J_\beta^2(u)+Y_\beta^2(u)}\cdot\frac{du}{u}$$

(where J_β and Y_β are Bessel and Neumann functions). The convection parameter β, obtained from filtration problem with the initial and boundary conditions for a pressure P of the type: $\begin{cases} P(\tau_P,1) = P_1 \\ P(0,\rho) = P_0 \end{cases}$ takes the form

$$\beta = \frac{k}{\eta}\cdot\frac{P_1 - P_0}{2D_T}\left(\frac{2}{\pi}\right)^2\int_0^\infty \frac{exp(-\tau_P u^2)\cdot du}{J_0^2(u)+Y_0^2(u)},$$

where dimensionless $\tau_P = D_P\, t/a^2$, $\rho = r/a$, and $D_P = k/(\eta\varepsilon\emptyset)$ is piezo-conductivity coefficient, k is permeability, η is viscosity, $\emptyset$ is porosity of movable fluid, and ε is formation compressibility.

NUMERICAL MODELING OF HEAT CONDUCTION AND MUD FILTRATION

Figure 1a) exemplifies an effect of temperature on NMR LWD echo train for clay-bound water formation with temperatures close to similar to real (figure 1b). Figure 1b) shows measured temperature in the borehole, formation temperature estimated using geothermal gradient, and temperature of NMR LWD sensitive volume calculated by our model at different borehole vertical depths. The results of fig 1 have been obtained with time of NMR measurement amounts value around 1 hour since drilled that is close to minimal for NMR LWD.

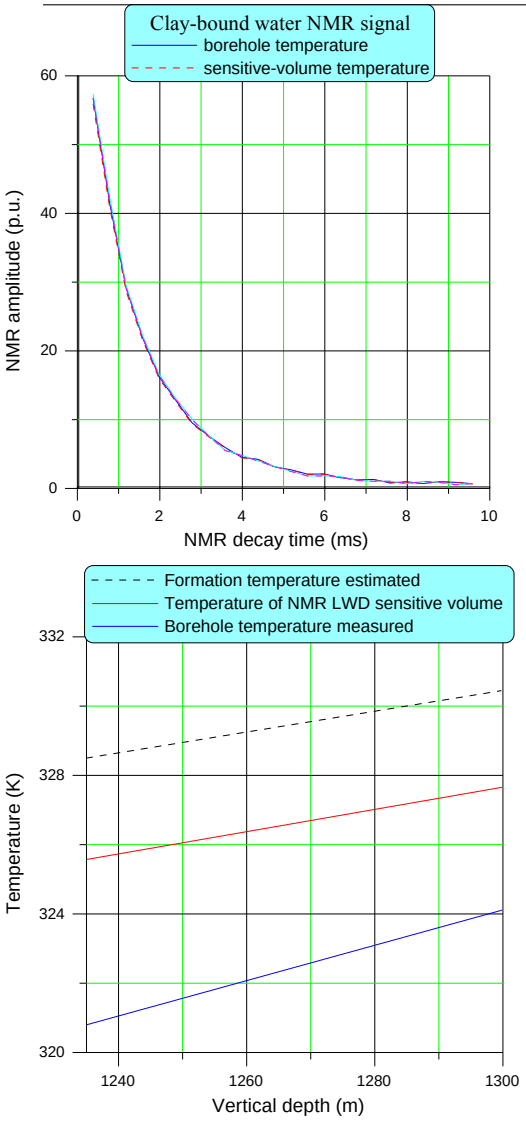

Figure 1. Figure 1. a) Temperature effect on NMR LWD signal at vertical depth 1235m to1300m, b) Temperature of borehole, formation, and sensitive volume vs vertical depth.

Figures 2 presents the same temperatures as at the figure 1b) for the same borehole, all rig statuses (drilling and reaming), and wider vertical depth interval. For permeable layers the temperature of NMR LWD sensitive volume is equal to the temperature measured in the borehole. The structure at vertical depth 1500m at figure 2 is associated with drilling technology. Nevertheless, structures at 1600 and 1690 m correlates with the permeability measured versus vertical depth.

The parameters used for the modelling are: the borehole diameter is 8.5", the sensitive-volume diameter is 13.2", the thermal diffusivity D_T is 10^{-2} cm^2/s, the viscosity η is 10^{-2} poise, the compressibility ε is $5 \cdot 10^{-2}$ Pa^{-1}, Ø=20%, the pressure difference $P_1 - P_0$ is 20 atm, and geothermal gradient is 3K/100m.

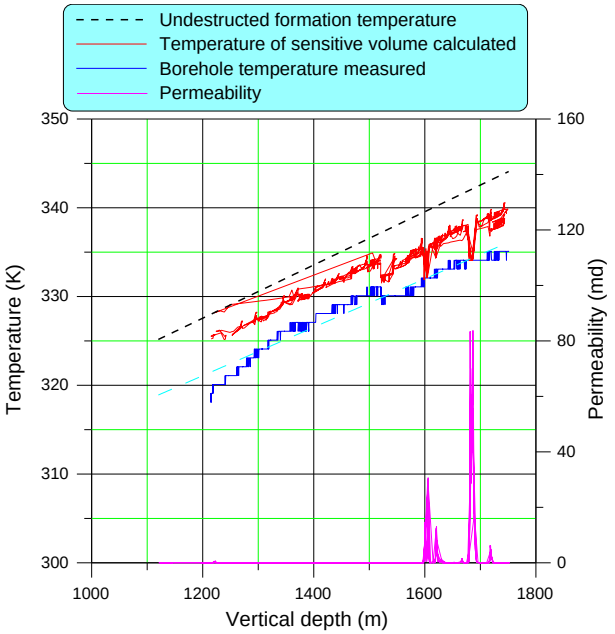

Figure 2. Temperature of borehole, formation, and sensitive volume vs vertical depth around permeable layers. Permeability measured by NMR LWD versus the borehole vertical depth.

CONCLUSION

An analytical approach for the estimation of the NMR LWD temperature effect is presented. The model applies when the temperature measured in the logging tool (i.e., in the borehole) is different from the actual formation temperature. In addition, to the heat transport through the formation, it includes the treatment of convective heat transfer for permeable layers invaded by mud filtrate. The theoretical results show that the heat transfer with convection is sensory adaptive to permeable layers. Due to the mud invasion in permeable zones, the temperature of NMR LWD sensitive volume is close to the measured temperature in the borehole, i.e., the mud temperature. Based on the results, a temperature effect correction for NMR LWD data can be implemented and conducted during standard NMR LWD data processing.

REFERENCES

Abragam, A. 1961. Principles of Nuclear Magnetism. Oxford, Clarendon Press, 599 p.

Carslaw H.S., Jaeger J.C., 1959. Conduction of heat in solids. Oxford, Clarendon Press, 386 p.

Coman R., Tietjen H. 2017.Temperature correction in NMR logging while drilling. - SPE-185334-MS, Mumbai, India.

Prammer M.G., Goodman G.D., Menger S.K. et al. 2000. Field test of NMR LWD device. SPWLA-EEE, Dallas, Texas.

Examples of the Bloch-Siegert effect in MRS

[1, 2] **Oleg A. Shushakov**
[1] Voevodsky Institute of Chemical Kinetics and Combustion, SB RAS, 3 Institutskaya str., 630090 Novosibirsk, Russia
[2] Novosibirsk State University, 1 Pirogova str., 630090 Novosibirsk, Russia
Email shushako@kinetics.nsc.ru

SUMMARY

An example of the MRS calibration on the ice of the Ob-river reservoir shows that calculations without considering the Bloch-Siegert effect differ from the experimental data at the maximum intensity of the RF pulse about 3 times.

An example of MRS studies in the Ebro-river basin (Spain) demonstrates that without taking into account the Bloch-Siegert effect the MRS calculated amplitude and phase differs from the experimental data about 2 and 12 times respectively at the maximum RF pulse intensity.

Key words: magnetic resonance, geomagnetic field, aquifers, Bloch-Siegert effect.

RESULTS

BLOCH-SIEGERT EFFECT IN MRS

If the water temperature is T = 293 K, and geomagnetic field strength is $B_0 = 6 \cdot 10^{-5}$ T, then integral equilibrium magnetization, $M_0 = 1.93 \cdot 10^{-7}$ J/(T*m³), is induced. If this magnetization is deviated from its equilibrium direction, it precesses around direction of geomagnetic field $\vec{B}_0$ with Larmor or Zeeman frequency of $\omega_0 = \gamma_H \cdot B_0$, where γ_H = 2.6753·10^8 radian//(s*T) is proton gyromagnetic ratio. Interaction of nuclei spin magnetization with external magnetic field $\vec{B} = \vec{B}_0 + 2\vec{B}_1 \cos\omega_0 t$ is in terms of energy operator of this interaction (the Hamilton operator or the Hamiltonian)

$$\hat{H}(r,t) = \hat{H}0 + \hat{H}1(r,t) = -\hat{\vec{I}} \cdot [\vec{\omega}0 + 2\vec{\omega}1(r) \cdot \cos\omega t] \quad \text{eq.1,}$$

where $\hat{I}$ is spin operator of nucleus, $\omega_1 = \gamma B_1$ is frequency of spin precession around RF field B_1 (Rabi's frequency).

The mean Hamiltonian being transformed into a coordinate system ($\tilde{x}, \tilde{y}, \tilde{z}$) rotating around the $\vec{B}_0$ field with frequency ω_0 after the Magnus expansion [Ernst et al., 1990]

$$\tilde{\bar{\bar{H}}}_1^{(0)}(t) = -\omega_1 \hat{I}_x \quad \text{eq.2,}$$

$$\tilde{\bar{\bar{H}}}_1^{(1)}(t) = -\frac{i\omega_0}{4\pi} \int_0^{\frac{2\pi}{\omega_0}} dt_2 \int_0^{t_2} dt_1 \left[\tilde{\vec{H}}_1(t_2), \tilde{\vec{H}}_1(t_1) \right] = \frac{\omega_1^2}{4\omega_0} \hat{I}_z \quad \text{eq.3,}$$

where [A,B]=AB-BA is a commutator of operators A and B [Shushakov, Maryasov, 2016].

Eq.3 shows that there is resonance frequency shift (Bloch-Siegert shift) [Bloch, Siegert, 1940]

$$\Delta\omega = -\omega_1^2 / 4\omega_0 . \quad \text{eq.4.}$$

If the half-space under the antenna is conductive, then the RF field is twice shielded by the resulting Foucault currents (skin-shielding): once - during excitation, the second time-when receiving the MRS signal. In the model of a homogeneous half-space of specific electrical conductivity σ, the radial and vertical components of the RF field for an antenna in the form of a circle of radius R_0 are expressed as follows [Shushakov, Legchenko, 1994 a]:

$$B_{1Z}(\mathbf{r}) = I_0 R_0 \int_0^\infty \frac{m^2}{m+u} e^{-uZ} J_1(R_0 m) \cdot J_0(rm)\, dm \quad \text{eq.5,}$$

$$B_{1r}(\mathbf{r}) = I_0 R_0 \int_0^\infty \frac{mu}{m+u} e^{-uZ} J_1(R_0 m) \cdot J_1(rm)\, dm \quad \text{eq.6}$$

where $u = (m^2 - \sigma\mu\omega)^{1/2}$, J_0, J_1 are Bessel functions, μ is the magnetic permeability. A more general model of the layered medium was in [Shushakov, Legchenko, 1994b, Shushakov, 1996]. Other antenna types were in [Isaev et al., 1996].

The initial amplitude of the MRS signal (after the RF pulse)

$$e_0(q) = \omega_0 / I_0 \int_V \tilde{M}_\perp(\vec{r}) B_{1\perp}^2(\vec{r}) / \left| B_{1\perp}(\vec{r}) \right| dV(\vec{r}) \quad \text{eq.7,}$$

where I_0 is the amplitude of the current, $q = I_0 \tau_p$ - intensity radio-frequency pulse current in the loop, $B_{1\perp}(\mathbf{r})$ is perpendicular to the field $\vec{B}_0$ component of the RF field, $\tilde{\vec{M}}_\perp(\vec{r})$ is perpendicular component of the magnetization in the rotating coordinate system. The Bloch-Siegert shift (eq.4) provides an additional rotation of nuclear magnetization around z axis within the rotating ($\tilde{x}, \tilde{y}, z$) frame [Trushkin et al., 1993]:

$$\tilde{\vec{M}}_x(\vec{r}) = \frac{\omega_1(\vec{r}) \cdot \Delta\omega}{\omega_{eff}^2(\vec{r})} \cdot [1 - \cos\omega_{eff}(\vec{r})\tau_p] \cdot \vec{M}_0(\vec{r}) \quad \text{eq.8,}$$

$$\tilde{\vec{M}}_y(r) = \frac{\omega_1(\vec{r})}{\omega_{eff}(\vec{r})} \cdot \sin\omega_{eff}(\vec{r})\tau_p \cdot \vec{M}_0(\vec{r}) \quad \text{eq.9.}$$

$\omega_{eff}(\vec{r}) = \sqrt{\omega_1^2(\vec{r}) + \Delta\omega^2}$ is the effective precession frequency. For the circular antenna

$$B_{1\perp}(\vec{r}) = \sqrt{[B_r(\vec{r})\cos\phi]^2 + [B_r(\vec{r})\sin\phi\sin\alpha + B_z(\vec{r})\cos\alpha]^2} ,$$

where α is the angle of inclination of the geomagnetic field with respect to the horizontal plane (inclination), φ is the axial angle with respect to the vertical (Fig. 1).

The integral equation 7 is used to solve the direct and inverse MRS problems [Legchenko, Shushakov, 1998].

AN EXAMPLE OF THE MRS CALIBRATION CONSIDERING THE BLOCH-SIEGERT EFFECT

MRS method calibration with regard to Bloch-Siegert effect was conducted via experiments on ice covered Novosibirsk Reservoir (Figure 1). Ice thickness and water depth were measured directly via drilling holes in the ice, and were 1±0.05m and 11±0.5m, respectively. Antenna of 50 m radius was used both for RF field generation and for the signal detection. The geomagnetic field inclination was 74°, proton resonance frequency was 2517 Hz ($B_0 = 5.9114 \cdot 10^{-5}$T).

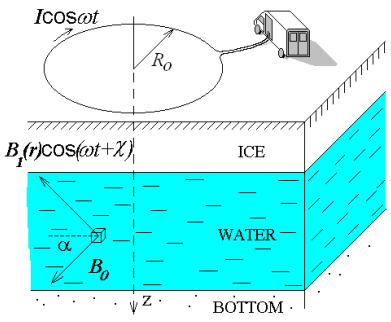

Figure 1. Detecting of the Bloch-Siegert effect on the ice of the Ob reservoir. Antenna radius 50m, 0 - 1 m ice, 1 - 11 m water. Inclination 74°, resonant frequency 2517 Hz.

Figure 2 compares the dependence of the MRS amplitude and phase (eq.7) on the RF pulse intensity with experimental data at pulse durations τ_p of 40 ms , typical for the MRS method, as well as twice the duration of 80 ms. The results of calculations coincide with each other at durations of 40 ms and 80 ms in the absence of the Bloch-Siegert effect (eq.4) and electromagnetic shielding, as well as when taking into account only electromagnetic shielding without taking into account the Bloch-Siegert effect. However, these calculation results are very different from the experimental data at an RF pulse intensity of more than 3000 A * ms. At the maximum RF pulse intensity of 15,000 A*ms for the experimental data, the results of calculations without taking into account the Bloch-Siegert effect differ from the experimental data by about 3 times. Besides. they do not explain the difference in the field experimental data at the duration of 40ms and 80ms. At the same time, taking into account the interference of electromagnetic shielding and the Bloch-Siegert effect, the results of calculating the amplitude of the MRS signal are different at the pulse durations of 40ms and 80ms, and they best approximate the field experimental data at the RF pulse durations of 40ms and 80ms, respectively. Qualitatively, this can be explained as follows: at the RF pulse duration of 40ms, at the same RF pulse intensity q (eq.7), the current amplitude and, accordingly, the RF field amplitude (eq.5, 6) are 2 times greater than at the duration of 80ms, so the Bloch-Siegert effect (eq.4) at 40ms is about 4 times greater than at 80ms. In this case, the Bloch-Siegert effect increases quadratically with increasing RF pulse intensity, which is observed both in model calculations and in experimental data. The accuracy of measuring the MRS amplitude was ±10-20 nV, the MRS phase was ±10-20°, which approximately corresponds to the size of the points indicating the experimental data in the figure 2.

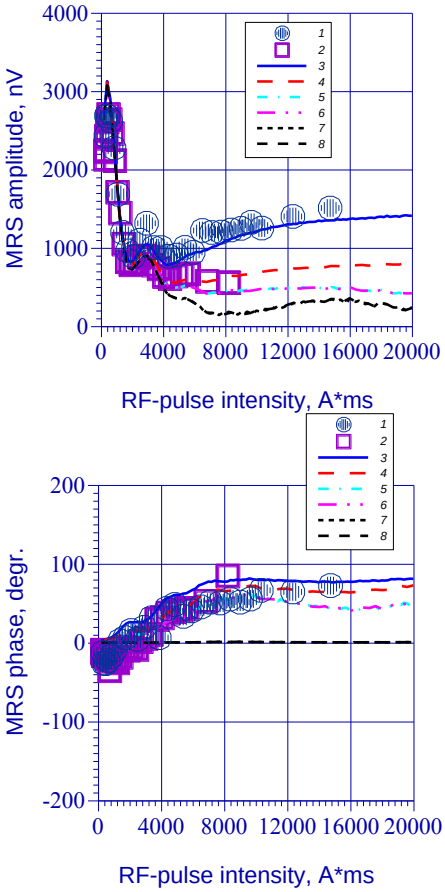

Figure 2. 1 - MRS amplitude and phase with RF duration 40 ms, experiment. 2 - 80 ms, experiment. 3 - 40 ms, calculation with the Bloch-Siegert effect and EM shielding. 4 - 80 ms, calculation with the Bloch-Siegert effect and EM shielding. 5 - 40 ms, calculation with EM shielding, without the Bloch-Siegert effect. 6 - 80 ms, calculation, with the EM shielding, without the Bloch-Siegert effect. 7 - 40 ms, calculation without the Bloch-Siegert effect and EM shielding. 8 - 80 ms, calculation without the Bloch-Siegert effect and EM shielding.

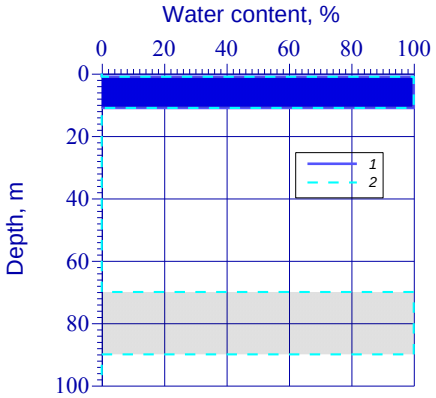

Figure 3. 1 – inversion with the EM shielding and the Bloch-Siegert effect: water 1 - 11 m, 100%. 2 - inversion with EM shielding (without the Bloch-Siegert effect), two layers: 1- 11 m and 70 - 90 m, 100%.

The results of solving the inverse problem in the form of a histogram of the dependence of water content (water content in

the rock in%) on the depth are shown in Figure 3. Taking into account the interference of electromagnetic shielding and the Bloch-Siegert effect, the solution of the inverse problem results in a single layer of water at a depth of 1 to 11 m with a water content of 100%. Without taking into account the Bloch-Siegert effect, as a result of solving the inverse problem, two layers are obtained: from 1 to 11 m with a water content of 100% and from 70 to 90 m with a content of 100%. Although the bottom was not drilled at this point, the absence of spin-spin relaxation of the MRS signal with short times (40-300 ms) [Shushakov Fomenko, 2004] clearly indicates that within the experimental error, free water in the pores or cracks of rocks is absent in a noticeable concentration (5-10%) to a depth of 80-90 m [Shushakov, Maryasov, 2016].

Figure 4 shows, as an example, the envelopes of the MRS signal decay at the RF pulse intensity of 432 A*ms and 14710 A*ms with long spin-spin relaxation times of about 900 ms. Thus, from Fig. 2, 3 it follows that there is not only a significant quantitative discrepancy between the experimental data and the magnetic resonance sounding model without taking into account the interference of electromagnetic shielding and the Bloch-Siegert effect (up to 3 times, Fig. 2), but also a qualitative one, namely, the appearance of a non-existent underground sea at a depth of 70-90 m.

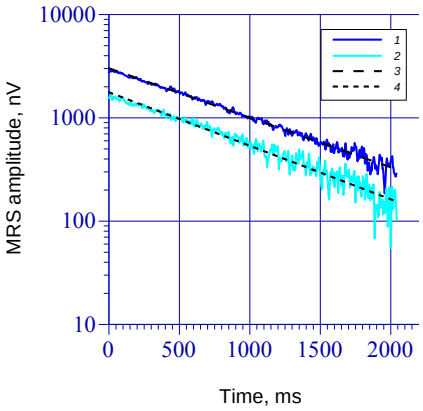

Figure 4. An example of the MRS signal envelope decay measured on the ice of the Ob reservoir at resonance frequency, the intensity of the RF pulse (duration 40 ms). 1 - 432 A*ms and 2 - 14710 A*ms, 3 - approximation 2998*exp(- t /905) nV, 4 - approximation 1739* exp (- t /850) nV.

AN EXAMPLE OF THE MRS FIELD APPLICATION CONSIDERING THE BLOCH-SIEGERT EFFECT

An example of the MRS study was conducted in the Ebro-river basin (Spain) with two instruments: the Hydroscope produced by the Institute of Chemical Kinetics and Combustion SB RAS and NUMIS PLUS, IRIS Instruments (France). The results of studies using the model without taking into account the interference of electromagnetic shielding and the Bloch-Siegert effect were published earlier [Plata, Rubio, 2005]. To generate the RF field and receive the MRS signal, eight-shaped antennas were used, first used in [Trushkin et al., 1994]. For the Hydroscope device, an antenna consisting of two circles with a diameter of 50 m was used, for the NUMIS device - in the form of two squares of 50x50 m [Plata, Rubio, 2005]. The lithological cross-section of the Te-27 point is presented in Table 1. Geoelectric cross-section: resistivity-250 ohms * m at depths from 0 to 40 m from the surface, 30 ohms*m-over 40 m. The angle of inclination of the geomagnetic field α was 55°, and the proton resonance frequency was 1906 Hz (B_0=4.473710^{-5} T).

Table 1.Lithological log of the Te-27 site, Ebro basin, Spain.

Depth (m)	Lithology	Age	Comments
0-1	Clay	Quaternary	Aquitard
1-14	Sandstone	Quaternary	Aquifer
14-50	Marl with gravel	Pliocene	Aquifer
50-105	Marl	Pliocene	Aquitard

Figures 5, show the amplitudes and phases of the MRS for the Te-27 point, depending on the pulse intensity, obtained by the Hydroscope device, and the results of their numerical approximation, taking into account the interference of electromagnetic shielding and the Bloch-Siegert effect. The best approximation of the experimental data was obtained by taking into account the interference of electromagnetic shielding and the Bloch-Siegert effect for aquifers from 1 to 14 m with a water content of 19% and from 14 to 50 m with a water content of 4%. For comparison, the calculated amplitude and phase of the MRS are given taking into account only electromagnetic shielding (without taking into account the Bloch-Siegert effect) for aquifers from 1 to 14 m with a water content of 19% and from 14 to 50 m with a water content of 4%.

Figure 6 shows an example of a histogram of the dependence of water content (water content in the rock in%) on the depth obtained from Figure 5 for the point Te-27. This histogram shows two aquifers: from 1 to 14 m with a water content of 19% and from 14 to 50 m with a water content of 4%. For comparison, a histogram of the dependence of the water content on the depth obtained by approximating the experimental data of Fig. 5 is given, taking into account only electromagnetic shielding (without taking into account the Bloch-Siegert effect) in the form of aquifers from 1 to 14 m with a water content of 19% and from 49 to 50 m with a water content of 25%.

It should be noted that both in Fig. 5. 6 and in Fig. 2. 3, the best approximation of the experimental data was achieved by taking into account the interference of electromagnetic shielding and the Bloch-Siegert effect. When taking into account only electromagnetic shielding (without taking into account the Bloch-Siegert effect), the amplitude of the MRS signal in Figure 5 differs 2 times at the maximum pulse intensity for experimental data (approximately 12,000 A * ms), the phase of the MRS signal in Figure 5 differs 12 times at the maximum pulse intensity. Therefore, to approximate the experimental data using the model without taking into account the Bloch-Siegert effect, it is necessary to add layers at depths close to the maximum for this type of antenna. For an antenna in the form of a circle with a diameter of 100 m, the maximum depth of the MRS is approximately 100 m. For an antenna in the form of an eight of two circles with a diameter of 50 m, the maximum depth of the MRS is approximately 50 m (Fig. 6). However, in reality, these layers do not exist, they appear only as an artifact of the model without taking into account the Bloch-Siegert effect. Such non-existent layers were obtained in the previously published work [Plata, Rubio, 2005] due to the erroneous interpretation of the MRS data without taking into account the Bloch-Siegert effect.

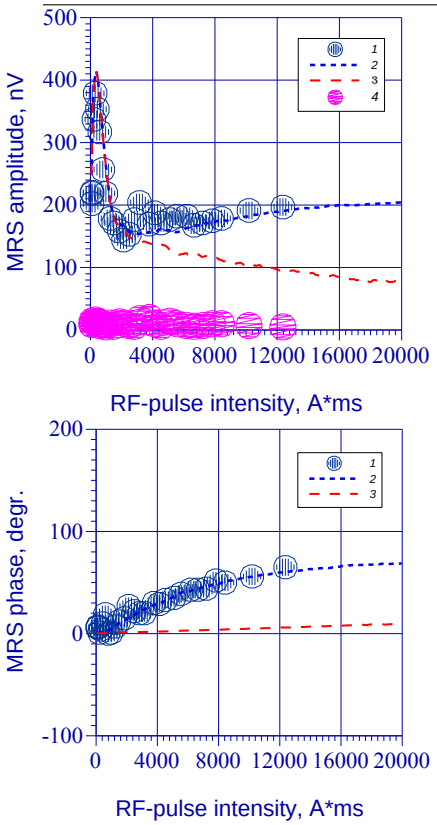

Figure 5. An example of the approximation of the MRS field-data amplitude and phase.. 1 - field datam Te-27, Ebro-River basin (Spain). 2 - approximation with EM shielding and the Bloch-Siegert effect for aquifers 1 -14 m, water content 19% and 14 - 50 m, water content 4%. 3 - calculation with only EM shielding (without the Bloch-Siegert effect) 1 - 14 m, water content 19% and 14 - 50 m, water content 4%.

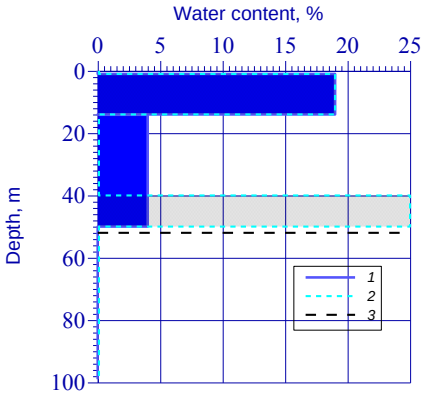

Figure 6. An example of the MRS inversion, Te-27, Ebro-River basin (Spain). 1 - solution with EM shielding and the Bloch-Siegert effect :aquifers 1 - 14 m, water content 19% and 14 - 50 m, water content 4%. 2 – solution with EM shielding only (without the Bloch-Siegert effect): aquifer 1 - 14 m, water content 19% and 40 - 50 m, water content 25%. 3 – the maximum depth of MRS with the eight-shaped antenna 2 x 50 m circles.

CONCLUSIONS

An example of the MRS calibration on the ice of the Ob reservoir shows good approximation of the experimental data by a model considering the interference of electromagnetic shielding and the Bloch-Siegert effect.

An example of MRS studies in the Ebro-river basin (Spain) demonstrates the necessity of taking into account the Bloch-Siegert effect in real field conditions.

ACKNOWLEDGMENTS

The author is grateful to V. M. Fomenko, V. D. Alexandrov for assistance in field experiments, J. L. Plata for a useful discussion of previously published results [Plata, Rubio, 2005].

REFERENCES

Bloch F. & Siegert A. 1940. Magnetic resonance for nonrotating fields. Physical Review, 57, p.522-527.

Ernst R. R., Bodenhausen G., Wokaun A.. Principles of Nuclear Magnetic Resonance in One and Two Dimensions. Clarendon: Oxford 1987, 610 p.

Isaev G. A., Filatov V. V., Pusep A. Yu., Storozhev A.V. 1996. On improving the efficiency of fresh water searches based on the use of the MPP-NMR complex. Geologiya i geofizika. 37(4). p.103-110.

Legchenko A. V. & Shushakov O. A. 1998. Inversion of surface NMR data. Geophysics, 63(1), p.75-84.

Plata J. L. & Rubio F.M. 2005. MRS experiment using Hydroscope instrument: some remarks. Presented at the EAGE 67th Conference & Exhibition - Madrid, Spain, Z 99.

Shushakov O. A. 1996. Groundwater NMR in conductive water. Geophysics, 61(4), p.998-1006.

Shushakov O.A. & Fomenko V.M. 2004. Surface-NMR relaxation and echo of aquifers in geomagnetic field. Applied magnetic resonance, 25, p.599-610.

Shushakov O. A. & Legchenko A.V. 1994. Calculation of the proton magnetic resonance signal from underground water taking into account the electrical conductivity of the medium. Geologiya i geofizika, 35(3), p.130-136.

Shushakov O. A. & Legchenko A.V. 1994. Proton magnetic resonance from underground water in horizontally layered media of different electrical conductivity. Geologiya i geofizica, 35 (10), p.161-166.

Shushakov O. A. & Maryasov A. G. 2016. Bloch-Siegert effect in magnetic-resonance sounding. Applied magnetic resonance.47, p. 1021-1032.

Trushkin D. V., Shushakov O. A., Legchenko A. V. 1993. Modulation effects in non-drilling NMR in the Earth's field. Applied magnetic resonance, 5, p.399-406.

Trushkin D. V., Shushakov O. A., Legchenko A. V. 1994. The potential of a noise-reducing antenna for surface NMR groundwater surveys in the earth's magnetic field. Geophysical Prospecting, 42, p.855-862

COMET – A toolbox for modelling and inversion of surface SNMR

[1]Nico Skibbe, [1]Mike Müller-Petke, [1]Thomas Günther

[1] Leibniz Institute for Applied Geophysics, Hannover, Germany

SUMMARY

Surface nuclear magnetic resonance (SNMR) is a suitable tool for the investigation of groundwater systems. A combined inversion of electrical resistivity tomography (ERT) and SNMR is of advantage as ambiguities encountered in coastal environments are reduced, a subsequent hydrological interpretation is simplified and the overall resolution is improved. With the software package COMET a combined inversion of these methods is possible. COMET is the first open-source software package allowing for 2D SNMR combined inversion accounting for arbitrary resistivity distributions. Under favorable conditions, the results are used to calculate the hydraulic conductivity distribution in 2D, a key parameter for hydrogeological investigations.

Key words: open-source, SNMR, modelling, inversion.

INTRODUCTION

Surface nuclear magnetic resonance (SNMR) is a method used for the characterization of aquifer systems. The sensitivity to water content and relaxation time gives access to hydraulic properties like porosity and hydraulic conductivity. If the resistivity distribution is known through an electrical resistivity tomography (ERT), a combination of the techniques ensures reliable information for the distinction between fresh-water or salt-water saturated aquifers and clay aquitards, which is especially useful when characterizing coastal aquifer systems (Costabel et al., 2017; Flinchum et al., 2019).

For the inversion of SNMR data, several software packages are available, including AarhusInv (Auken et al., 2015), Akvo (Irons et al., 2019) and MRSmatlab (Müller-Petke et al., 2016). These packages are either limited to 1D applications or are freely available only for scientific purposes. None of the above can account for arbitrary resistivity distributions which is a need for combined MRT and ERT inversion.

COUPLED MAGNETIC RESONANCE AND ELECTRICAL RESISTIVITY TOMOGRAPHY (COMET)

For the combined inversion of ERT and SNMR, we develop the Python software package COMET. Built on the open-source software packages pyGIMLi (Rücker et al. 2017) and custEM (Rochlitz et al., 2019), COMET can handle the complete SNMR physics from magnetic field calculations in 1D, 2D and 3D, to kernel calculation used in the forward calculation and the inversion process. Figure 1 shows a flowchart of the various user inputs and their interaction between the different classes as well as the numerical processes in the background. Additionally, COMET can interchange the structural information of different methods during the inversion process using pyGIMLi inversion instances and allow for a structurally coupled cooperative inversion (SCCI). This makes it easy to combine the inversion of SNMR data with other pyGIMLi-based inversions, in the presented cases ERT.

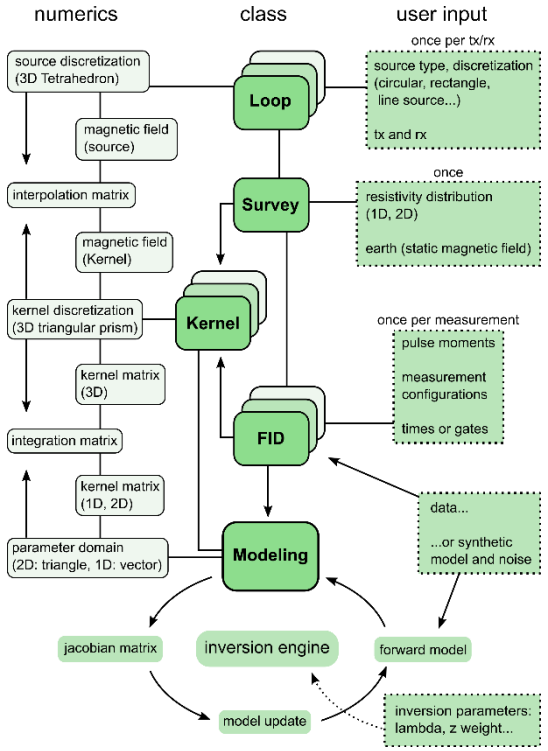

Figure 1: Flowchart of COMET source-code components and their interaction as well as interaction with the user input (Skibbe et al. 2020).

STRUCTURALLY COUPLED COOPERATIVE INVERSION (SCCI)

Structural coupling exchanges information between different single inversions. The technique is independent of the used algorithms and jointly inverts two or more different methods by ensuring a common parameter structure in a data-driven way, compared to simple clustering algorithms. Information is exchanged dependent on the parameter gradients of the single parameter distributions. The SCCI allows for a local lowering of the global smoothness constraints where other parameter distributions observe stronger parameter gradients. As a result, after a few iterations common gradients are found for all

parameter distributions, while other areas become increasingly smooth. Apart from common gradients, the local adjustment of the smoothness constraints also allows to fit larger parameter jumps than normally possible for a smoothness-constrained inversion, leading to less blurry results.

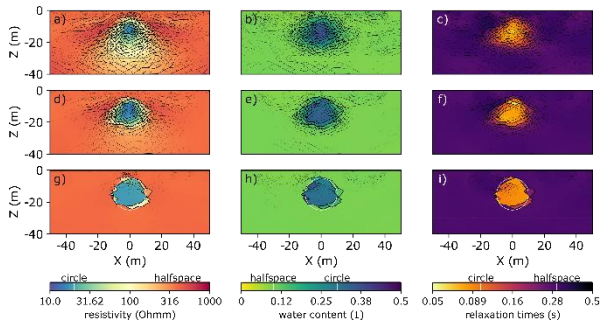

Figure 2: Models and individual weighting factors (w (res) , w (wc) , w (t2), of three steps of the SCCI: smooth inversion results of the ERT as a) resistivity and for MRT as b) water content and c) relaxation times; (d–f) first iteration; and (g–i) final iteration of the SCCI. Individual weights based on the model roughnesses are shown with black lines of increasing thickness. Thicker lines represent a stronger gradient of the two adjacent cells. The synthetic model values are marked in the color bar with white lines (Skibbe et al., 2021).

Figure 2 shows an example of a structurally coupled inversion for a synthetic 2D case. Starting point of an SCCI are the smooth inversion results, in this case for resistivity (a), water content (b) and relaxation times (c). The single inversion results (a-c) show different resolutions and an overall blurry representation of the target structure. The smoothness constraint omits a large parameter jump at the edge of the circular structure. During the SCCI, a lowering of the constraints leads to a much clearer image of the structure even after a single iteration (subfigures d-f). The final result (g-i) clearly resolves the shape of the anomaly as well as parameter values.

2D RESISTIVITY

Main task of COMET is the accurate calculation of SNMR kernel functions for the forward modeling and the Jacobian calculation based on magnetic fields. A special emphasis is set on the handling of arbitrary and smooth resistivity distributions. To correctly account for 2D resistivity during the magnetic field calculations COMET uses the open-source software custEM, a customizable Python package for the modeling of magnetic and electric fields . CustEM is implemented in a way that no further knowledge about custEM or any other underlying third-party libraries is required to perform a 2D inversion with COMET. By default, the resistivity distribution input is defined on the same discretization as the water content and relaxation times for the purpose of structural coupling. COMET handles the interpolation of the 2D input resistivity to a suited 3D tetrahedral discretization for the FE modeling using custEM and then interpolates the magnetic field values to a suited 3D triangular prism mesh for the kernel calculation. The kernel on the prism mesh is then integrated to the original 2D triangular input mesh for the inversion. This way a common discretization for water content, relaxation times and resistivity is ensured and allows for the resistivity to be used during the kernel calculation as well as the SCCI to get the full benefit of the combined inversion in all processing steps.

Figure 3 shows a visual walkthrough of the various re-meshing steps and calculations inside the COMET kernel calculation.

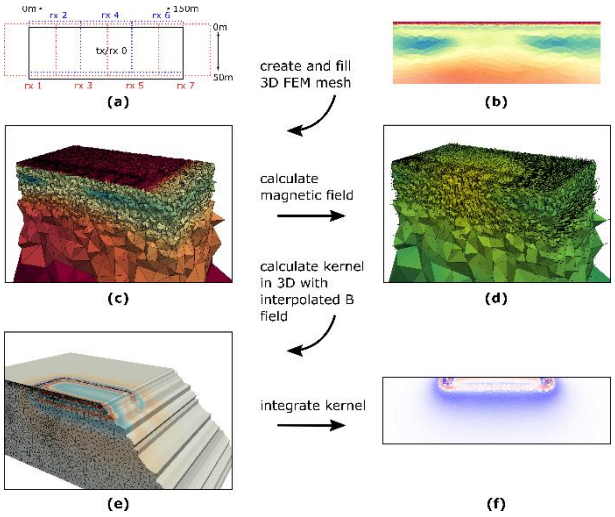

Figure 3: Walkthrough of a 2D SNMR inversion and with overview of the different meshes used in the inversion (Skibbe et al. 2020).

FIELD CASE AND HYDRAULIC CONDUCTIVITY

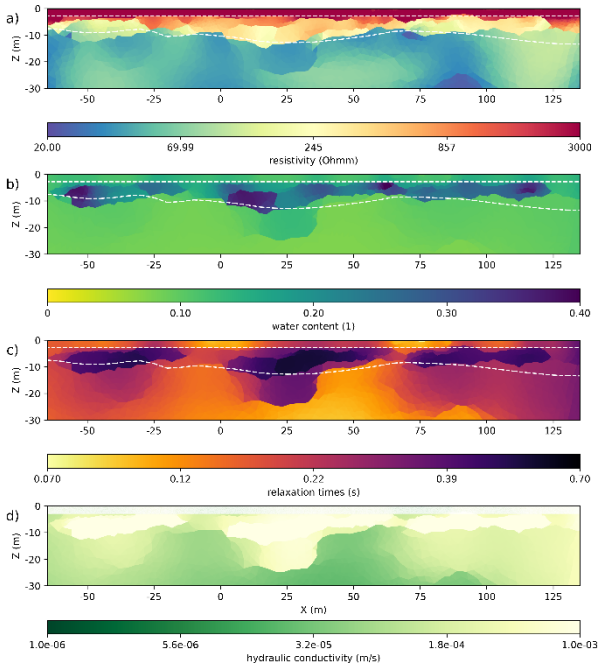

Figure 4: Coupled inversion results for the Schillerslage field case for a) resistivity (ERT), b) NMR water content and c) relaxation times. d) estimated hydraulic conductivity based on the inversion results (Skibbe et al., 2021).

We show the full extent of the SCCI, including a full incorporation of a smoothly distributed ERT image in the kernel calculation, as well as the SCCI, at the example of the well-known test-site in Schillerslage, Germany, in Figure 4. At the location, alternating layers of till and gravel are encountered. The SNMR measurement consists of three ETRA setups in a half overlapping roll-along profile, and is supported by an ERT profile and referenced by known

reflectors from previous ground penetrating radar (GPR) data (white lines, Figure 4). For the kernel calculation we use the parameter distribution of the smooth ERT inversion result directly. The SCCI results provide a purely data-driven blocky representation of the subsurface, which is further used for a subsequent hydrogeological interpretation of the gravel pockets, without the use of additional structural information. The known GPR boundaries are used purely as reference. For aquifers the relaxation times and water content can be used to calculate the hydraulic conductivity of the subsurface using the Kozeny-Godefroy model (KGM) presented by Dlugosch et al. (2013). In the presented case we use the resistivity for the SCCI to benefit from the structural information but in general the resistivity is also useful to solve ambiguities between fresh-water and salt-water aquifers and aquitards consisting of clay or till, often encountered when working in a coastal environment. Figure 4d shows the hydraulic model based on the results of the SCCI to get an idea of the extent and the composition of the water-bearing gravel pockets. Note that the hydraulic conductivity of the KGM model is not valid for the till layers and the not fully saturated part of the vadose zone. The interpretation is in general agreement with the GPR reflectors and other inversion results presented by Jiang et al. (2020). The analysis of boreholes around the target location also confirms the observed aquitard beneath the gravel and the hydraulic properties of the aquifers as shown by Jiang et al. (2020).

CONCLUSIONS

The open-source software package COMET allows for 1D and 2D inversion and modelling of SNMR data. COMET provides a structurally coupled inversion with electrical resistivity. A combination of ERT and SNMR solves various purposes. First, the resistivity can be used in the magnetic field calculation and secondly the structural information can be used for the SCCI to enhance the image of the inversion. The software package COMET can handle arbitrary resistivity distributions and loop layouts for the combined inversion of SNMR and ERT data sets for these purposes. Along with a decreased ambiguity the results of the SCCI are less blurry than common smoothness-constrained inversion results which is beneficial for subsequent hydrogeophysical interpretations. This has been demonstrated at the example of a comprehensive 2D field case. The resolved gravel pockets are validated by additional measurements and are in agreement with earlier work with the data set. A model of the hydraulic conductivity based on the SNMR water content and relaxation times is validated by borehole analysis from the target site.

AVAILABILITY

The COMET package is freely available (https://gitlab.com/Skibbe/comet) and documentation is provided at: (https://comet-project.readthedocs.io)

REFERENCES

Auken, E., A. V. Christiansen, C. Kirkegaard, G. Fiandaca, C. Schamper, A. A. Behroozmand, A. Binley, E. Nielsen, F. Effersø, N. B. Christensen, K. Sørensen, N. Foged, and G. Vignoli, 2015, An overview of a highly versatile forward and stable inverse algorithm for airborne, ground-based and borehole electromagnetic and electric data: Exploration Geophysics, 46, 223–235.

Costabel, S., B. Siemon, G. Houben, and T. Günther, 2017, Geophysical investigation of a freshwater lens on the island of Langeoog, Germany - Insights from combined HEM, TEM and MRS data: Journal of Applied Geophysics, 136, 231–245.

Dlugosch, R., T. Günther, M. Müller-Petke, and U. Yaramanci, 2013, Improved prediction of hydraulic conductivity for coarse grained unconsolidated material from nuclear magnetic resonance: Geophysics, 78, (4), EN55–EN64.

Flinchum, B. A., W. S. Holbrook, A. D. Parsekian, and B. J. Carr, 2019, Characterizing the critical zone using borehole and surface nuclear magnetic resonance: Vadose Zone Journal, 18, 1–18.

Irons, T. P., B. Bloss, T. Kremer, and M. A. Kass, 2019, Akvo: A surface NMR workbench: FastTIMES, 24, 101–115.

Jiang, C., J. Igel, R. Dlugosch, M. Müller-Petke, T. Günther, J. Helms, J. Lang, and J. Winsemann, 2020, Magnetic resonance tomography constrained by ground-penetrating radar for improved hydrogeophysical characterisation: Geophysics, 85, (6), JM13–JM26

Müller-Petke, M., M. Braun, M. Hertrich, S. Costabel, and J. Walbrecker, 2016, MRSmatlab — A software tool for processing, modeling, and inversion of magnetic resonance sounding data: Geophysics, 81, (4), WB9–WB21.

Rücker, C., T. Günther, and F. Wagner, 2017, pyGIMLi: An open-source library for modelling and inversion in geophysics: Computers & Geosciences, 109, 106–123.

Skibbe, N., R. Rochlitz, T. Günther, and M. Müller-Petke, 2020, Coupled magnetic resonance and electrical resistivity tomography: An open-source toolbox for surface nuclear-magnetic resonance: Geophysics, 85, (3), F53–F64.

Skibbe, N., Günther, T., & Müller-Petke, M. (2021). Improved hydrogeophysical imaging by structural coupling of two-dimensional magnetic resonance and electrical resistivity tomography. Geophysics, 86, (5), WB135–WB146.

Resolving regional variations in groundwater table using SNMR

[1]M. Vang [1]D. Grombacher [2]L. Liu [2]M. P. Griffiths [2]J. J. Larsen

[1]Geoscience Department
Aarhus University

[2]Department of Electrical and Computer Engineering
Aarhus University

SUMMARY

Water table depth plays an important role in many biological and geological processes and is an important input to hydrological models. Constraining water table depths is often done using boreholes, yet boreholes are sparse in many areas. Surface NMR presents a non-invasive approach to estimate the water table depth but is often limited in its ability to map large regions by its slow measurement times. Here we present a validation of a recently developed steady state approach for surface NMR through mapping of regional water table variations in three areas in Denmark. These soundings are validated against existing boreholes to show that a steady state SNMR scheme is able to accurately resolve water tables in the shallow subsurface.

Key words: Steady State, SNMR, Case Study.

INTRODUCTION

Surface NMR is a unique method for groundwater mapping due to its sensitivity to water content and relaxation times, which can be related to porosities and hydraulic properties (Hertrich, 2008). One of the limitations of the method is the slow acquisition time. Compared to other geophysical methods, e.g., TEM, the time spent at each site is far greater due to the low signal amplitude.

In this abstract, three case studies from Denmark will be presented, showing the possibility of mapping regional variations in the groundwater table using a novel steady state measurement scheme for surface NMR. The scheme increases the signal to noise ratio by rapid stacking, which enables the measurement of the NMR signal in places where Free Induction Decay (FID) previously struggled. When the noise conditions are moderate (~<100-200 nV RMS noise in a 50 by 50m loop) the steady-state scheme is able to map many sites per day. In one of the discussed areas, acquisition times of ~25 minutes per site enabled > 10 sites per day to be measured, peaking at 16 sites measured in a single day by a field crew of 2 persons (~400-500 meters between sites). Our goal in this work is to highlight feasibility of the steady-state scheme through several regional water table mapping campaigns.

METHODS

The surface NMR measurement originates from proton's spin which is perturbed via a magnetic field by a surface coil. When the excited spins return to equilibrium it creates a magnetic field which is measured by a receiver coil. This measured signal is inverted to estimate subsurface water content, relaxation times, information valuable for groundwater modelling (Mohnke & Yaramanci, 2008). The staple measurement in surface NMR is known as a Free Induction Decay (FID), which measures the signal produced by a single excitation pulse. Before a FID subsequent measurement, the NMR system has to return to equilibrium, which typically requires a wait time on the order of ~3-5 seconds in practice. This work focuses on validation of novel steady-state free precession approach for surface NMR (Carr, 1958; Ernst & Anderson, 1966). Here a train of identical pulses drives the system into an altered equilibrium, called the steady-state. These signal between neighbouring pulses is measured and fast repetition times allow large stack numbers to be collected in short time frames. This delivers significant gains in SNR. This makes the data acquisition more feasible in high-noise settings and can reduce acquisition times. In figure 1 three pulse sequences are shown: a) an FID and in b) and c) two steady-state schemes. The FID in panel a), a single pulse occurs within the 0.5s portrayed in the figure, a duration after which the magnetisation is often fully decayed in the field. The steady-state sequence termed "regular" in panel b) consists of a train of identical in-phase pulses. The NMR signal is sampled in the intervals between pulses, allowing many repeated measurements in a short interval. The steady-state sequence in panel c) termed "alternating" involves a train of identical pulses where subsequent pulses are phase-shifted by π. Other than the phase shifts the alternating and regular sequences are identical.

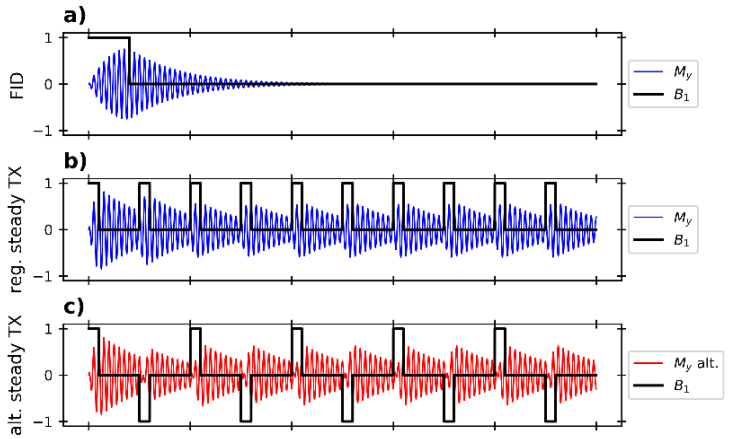

Figure 1 Pulses sequences: A) Free Induction Decay sequences with the pulse(B1) and the corresponding magnetisation(M_y), B) A termed "regular" steady-state pulse showing the high stacking ability as well as the pulses and the magnetisation, C) the termed "alternating" steady-state pulses and the magnetisation.

RESULTS

We present results from three field campaigns completed in Jutland, Denmark, near the towns of Aars, Sunds and

Silkeborg, respectively. The field sites vary greatly in noise level, yet all show similar trends in the geology of the subsurface, primarily consisting of meltwater sands or sandy tills. The scope of the campaigns was to resolve regional variations in water table. The Apsu system (Liu, 2019), was employed, along with a square 50 by 50m coincident coil.

In figure 2 an overview of the three surveys is shown. Table 1 includes information of each of the areas and indicates how production rates have increased over these first campaigns as more experience with steady-state schemes was gained. In panel a) the soundings from Aars are viewed, with 29 sites surveyed. The distances between soundings are ~100-200m for the area. Four steady-state pulse sequences were used for each of the soundings, where the different sequences correspond to different delay times and pulse durations. Only one out of twenty-nine sites, has been culled due to poor data quality. Each of the pulse sequences had 16 pulse moments which corresponds to 64 total measurements per site (16 pulse moments for 4 sequences). In panel b) the soundings collected near Sunds are shown with 38 soundings collected in a less dense grid. Here, the number of pulse moments were reduced to reduce redundancy in data set (e.g., data with overlapping spatial sensitivity). In panel c) the soundings from Silkeborg are shown with 50 sites and ~500m between sites. The evenly distributed soundings are possible here because measurements took place in a national forest without infrastructure. Here, five different steady-state pulse sequences were measured at each site, with the number of pulses moments reduced to five for each. This allowed a 2 persons crew acquire up to 16 sites in a day with 500m in between sites (with ~25 mins of measurement per site). For brevity, this abstract discussed only the Aars survey further.

To map the water table the data from each of the soundings has been inverted. The inversion used is a smooth inversion with fixed layer thicknesses, with vertical constraints. The reason for using a smooth inversion is the ability to use fast mapping to optimize inversion speeds (Griffiths et al., 2021). The resistivity model was set as prior information from a previous tTEM survey (Auken et al.,2019). All 64 measurements from each site are inverted jointly to produce a single subsurface model fitting all sequence's data simultaneously. The water table at each location is estimated heuristically by examining the water content profile and picking the depth where an increase in water content occurs. Figure 3 displays results of the Aars campaign where the results from 28 sites were used to map the water table across the region (circles). The water table measured in boreholes are also displayed (squares). The borehole data is extracted from Jupiter Database, the Danish national well database. In panel a), the depth to water table map is shown. The surface NMR soundings are consistent with the boreholes in the area. The overall trend is a shallow water table dipping towards the NW. The surface NMR soundings complement the borehole data by allowing denser data collection and the coverage in areas without boreholes. In figure 3 panel b) shows an example of an inversion result, with the corresponding location of this site is indicated by the green cross in panel a). The panel show a peak in the water content profile at ~3m where the water table is estimated 2 meters below surface. The corresponding T_2^* profile is shown along side the resistivity model from the tTEM survey. A nearby borehole has been added to correlate with the estimated water table and shows a good agreement. In panel c) another example of a subsurface model is, with the corresponding location marked by a yellow cross in panel a). Here, a gradual change towards high water content is visible. The depth to water table of this was set to 7m which fits nicely with the borehole close by which had a pressure head at 7.25m. Beneath the water table a relatively consistent water content is present – consistent with the observation of a thick sand unit over this depth interval in a nearby borehole.

CONCLUSIONS

Several field campaigns employing the novel steady-state approach are shown to accurately resolve regional water table variations. Comparison with borehole data demonstrates the reliability of the steady-state estimated water table depths. Surface NMR is well-suited to interpolate between sparse borehole data - together forming a more densely sampled model of regional water table variations. The rapid steady-state scheme shows great promise for dense spatial mapping of large regions in feasible field times.

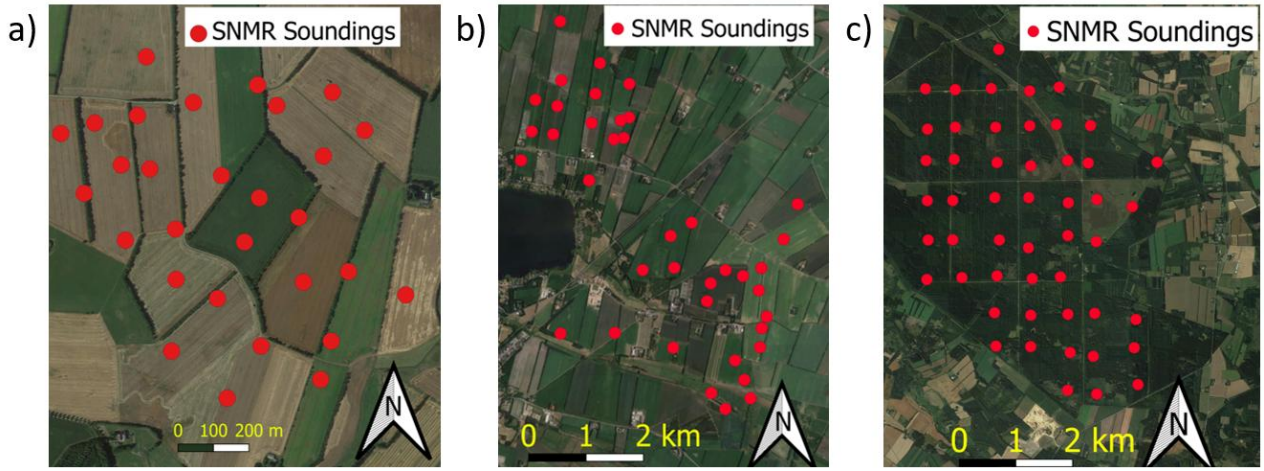

Figure 2 Showing the three areas of mapping, a) Aars, b) Sunds, and c) Silkeborg.

Area	No. Sites	No. Field days	No. sites used in mapping	No. Measurements per site
Aars	29	10	28	64
Sunds	38	12	32	48
Silkeborg	50	5	50	25

Table 1 Field acquisition information of the three areas of mapping.

REFERENCES

Auken, E., Foged, N., Larsen, J. J., Lassen, K. V. T., Maurya, P. K., Dath, S. M., & Eiskjær, T. T. (2019). tTEM—A towed transient electromagnetic system for detailed 3D imaging of the top 70 m of the subsurface. Geophysics, 84(1), E13-E22.

Carr, H. Y. (1958). Steady-state free precession in nuclear magnetic resonance. Physical Review, 112(5), 1693.

Ernst, R. R., & Anderson, W. A. (1966). Application of Fourier transform spectroscopy to magnetic resonance. Review of Scientific Instruments, 37(1), 93-102.

Liu, L., Grombacher, D., Auken, E., & Larsen, J. J. (2019). Apsu: a wireless multichannel receiver system for surface nuclear magnetic resonance groundwater investigations. *Geoscientific Instrumentation, Methods and Data Systems*, *8*(1), 1-11.

Hertrich, M. (2008). Imaging of groundwater with nuclear magnetic resonance. Progress in Nuclear Magnetic Resonance Spectroscopy, 53(4), 227.Sdfk

Mohnke, O. & Yaramanci, U. (2008). Pore size distributions and hydraulic conductivities of rocks derived from magnetic resonance sounding relaxation data using multi-exponential decay time inversion. Journal of Applied Geophysics., 66, 73-81.

Griffiths, M. P., Grombacher, D. J., & Larsen, J. J. (2021). Efficient numerical Bloch solutions for multipulse surface NMR. *Geophysical Journal International*, *227*(3), 1905-1916.

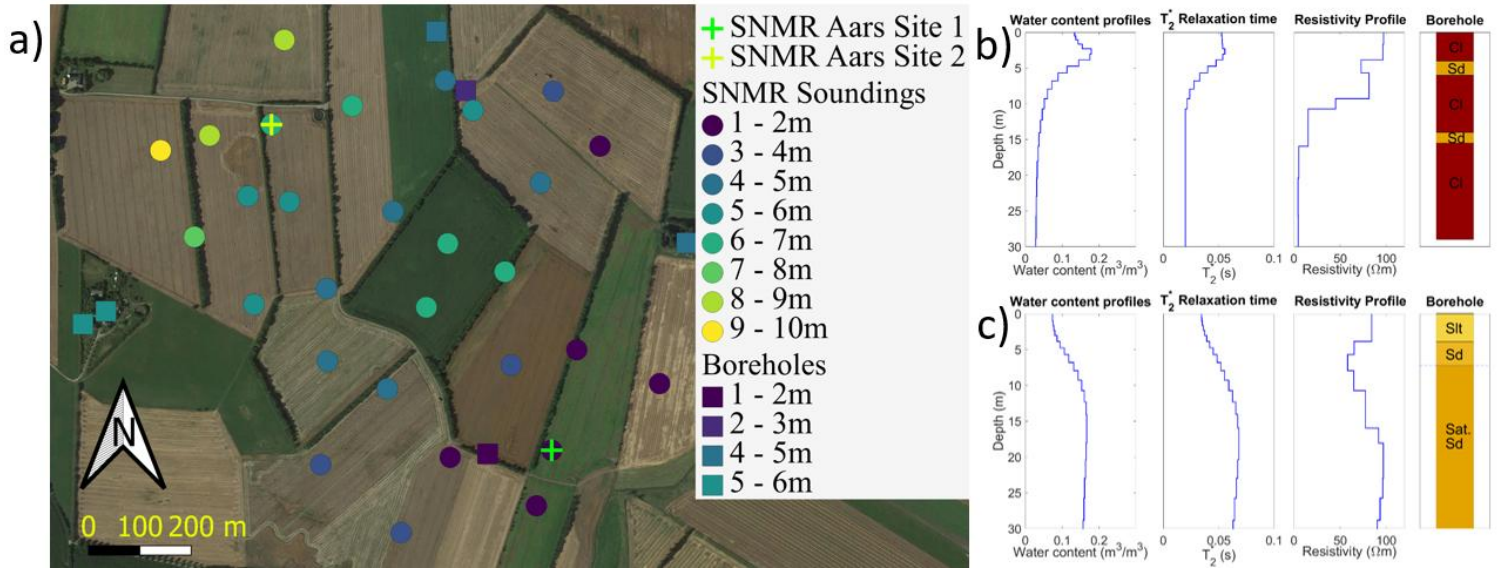

Figure 3 a) Aars depth to water table at each sounding and borehole, b) Aars Site 1 showing very shallow water table, c) Aars Site 2 showing deeper water table. (Sd=Sand, Cl=Clay/till, Slt=Silt, Sat. Sd=Saturated sand)

A Special Construction Loop for Harmonic Noise Cancellation in Situ

Pengfei Wang
College of Instrumentation and Electrical Engineering
Jilin University
Ximinzhu Street No.938, Changchun, China
Wangpf20@mails.jlu.edu.cn

Jinbao Zhu
College of Instrumentation and Electrical Engineering
Jilin University
Ximinzhu Street No.938, Changchun, China
zhujb16@mails.jlu.edu.cn

Tingting Lin
College of Instrumentation and Electrical Engineering
Jilin University
Ximinzhu Street No.938, Changchun, China
ttlin@jlu.edu.cn

SUMMARY

Figure-8 loops are often applied to reduce powerline harmonic noise in MRS measurement in situ, but the disadvantage of this method is that long time sampling is needed for calculating the optimal placement angle. In this study, we apply a special construction loop with four knots to reduce the harmonic noise. By modeling the magnetic flux produced by powerline harmonics, we calculate the induced electromotive force (emf) in the square loop, figure-8 loop, and the special construction loop. By comparing the results of simulation and field test, it can be demonstrated that the special construction loop is better than the square loop and figure-8 loop for harmonic noise cancellation in situ.

Key words: MRS, harmonic noise cancellation, special construction loop

INTRODUCTION

Magnetic resonance sounding (MRS) has been used in shallow aquifers characterization and freshwater management in the last decades (Behroozmand et al., 2015). However, signals acquired by the MRS instrument are unreliable in areas with serious noise interference, mainly for the following two reasons: 1) A large side length coil is used to work as the sensor in the acquisition system, meanwhile, the amplitude of induced noise is much larger than the signals (Larsen et al., 2014), which results in low signal-to-noise ratio (SNR), 2) High amplitude noise leads to saturation of the pre-amplifier easily, which causes nonlinear distortion of the collected data and the inability to retrieve meaningful signals (Lin et al., 2017). Therefore, the development of noise suppression technology is of great significance to improve the efficiency of MRS field detection.

Recent investigations have demonstrated that it can be divided into three types of environmental noise, namely random noise, spike noise, and harmonic noise (Larsen et al., 2016). Since the harmonic noise is closely related to human activities, it shows the complex temporal-spatial distribution. In reality, the widely used scheme is laying a pair of figure-8 loops proposed by Trushkin et al. at an early stage (Trushkin et al., 1994). Furthermore, the figure-8 loop is easy to implement and is robust to overcome harmonic noise in a high noise environment. Nevertheless, it is not straightforward to determine the optimal direction with numerous powerlines nearby (Girard et al., 2020).

In this study, we propose a special construction loop with four knots, which can be used to reduce the harmonic noise in MRS. We compared the induced electromotive force (emf) in the figure-8 loop and the special construction loop, the results of simulation and field test show that this special loop has a better effect than harmonic noise suppression.

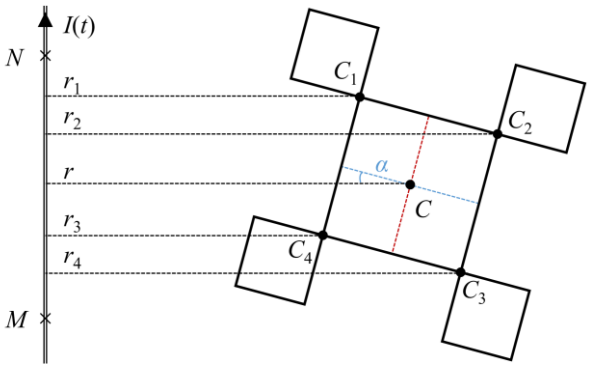

Figure 1: The schematic diagram of the special construction loop.

METHODS

According to Girard et al. (2020), for a square loop of area S on surface ground, the emf(t) generated by the harmonic current in a powerline can be expressed as

$$emf(t) = \pm \frac{\mu_0}{2\pi} \cdot \frac{S}{r} \cdot \frac{dI(t)}{dt} \quad (1)$$

where $\mu_0 = 4\pi \times 10^{-7}\ \mathrm{T \cdot m/A}$ is the magnetic permeability in a vacuum; r is the horizontal distance between the center of the loop and the power line; The symbol $\pm$ indicates the direction of the current in the

powerline and does not affect the absolute magnitude of the calculation result.

On this basis, the *emf*(t) in a figure-8 loop is

$$emf\left(t\right)=\pm\frac{\mu_0}{2\pi}\frac{dI\left(t\right)}{dt}\cdot\frac{S\sqrt{2S}}{r^2}\sin\alpha \quad (2)$$

where r_1 and r_2 are the distance between the center of each small loop in a figure-8 loop and the powerline.

Considering the principle of the mutual offset of the induced electromotive force in the two coils of figure 8, we combine four figure-8 loops to form a special construction loop, the shape of this type of loop is shown by the solid black line in Figure 1, and MN is the powerline. The large square coil in the middle can be seen as consisting of four identical small coils, and the coil at each diagonal position is the same as the equivalent small coils. Thus, the *emf*(t) in this loop is

$$emf\left(t\right)=\pm\frac{\mu_0 S}{2\pi}\frac{dI\left(t\right)}{dt}\left[\begin{array}{l}\frac{\sqrt{2S}}{r_1^2}\sin\alpha-\frac{\sqrt{2S}}{r_2^2}\sin\alpha\\+\frac{\sqrt{2S}}{r_3^2}\cos\alpha-\frac{\sqrt{2S}}{r_4^2}\cos\alpha\end{array}\right] \quad (3)$$

where r_1, r_2, r_3, and r_4 are the distance between the knot C_1, C_2, C_3, and C_4, respectively; α is the rotation angle.

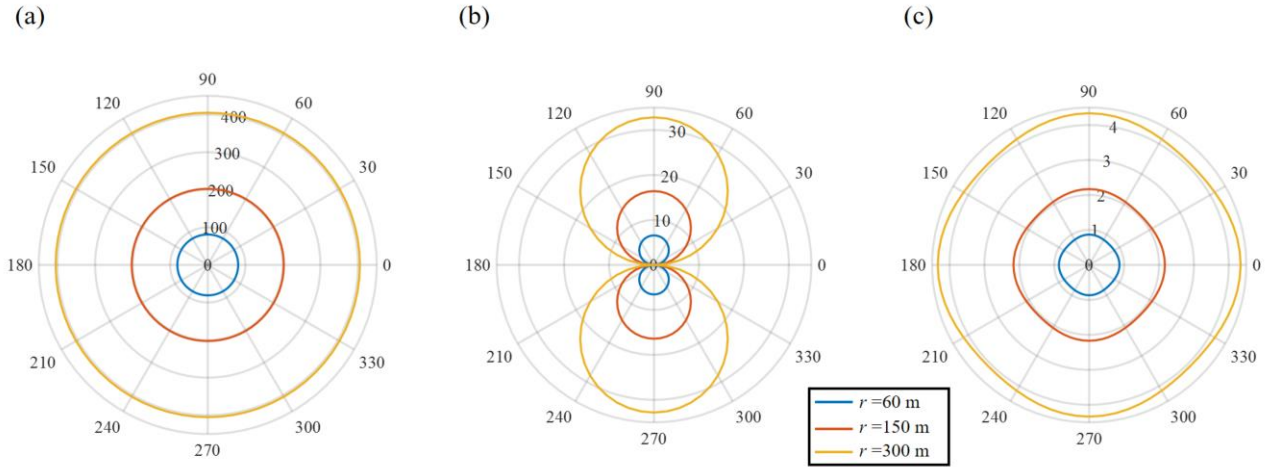

Figure 2: *emf*(*t*) in the three types of loops with different angle α. (a) The square loop; (b) The figure-8 loop; (c) The special construction loop

RESULTS

In Figure 2, we show the comparison of the simulation results, that is *emf*(*t*) in the three types of loops with different angle α. For a square loop, the amplitude of *emf*(*t*) does not change with the angle, but it is inversely proportional to the magnitude of *r*. In Figure 2 (b), the amplitude of *emf*(*t*) shows a strong correlation with the angle, it equals zero when the angles are 0° and 180°, because the figure-8 loop is parallel to the powerline. And the amplitude is maximum when the angles are 90° and 270°. The special construction loop shows the best results in Figure 2 (c), it has the smallest amplitude and almost no correlation with angle change. Figure 3 provides an example of a field test, the site is located on the campus of Jilin University, in downtown Changchun. We used three types of coils for testing, all of which have the same total area. For sample data with a duration of 0.24s, we can observe the harmonic noise with periodic amplitude variation, but the amplitude in the special construction loop and figure-8 loop is much smaller than it in the square loop. After 16 stacking, there is still harmonic noise interference in the square loop and figure-8 loop, but the amplitude of harmonic noise interference in the special construction loop is greatly reduced.

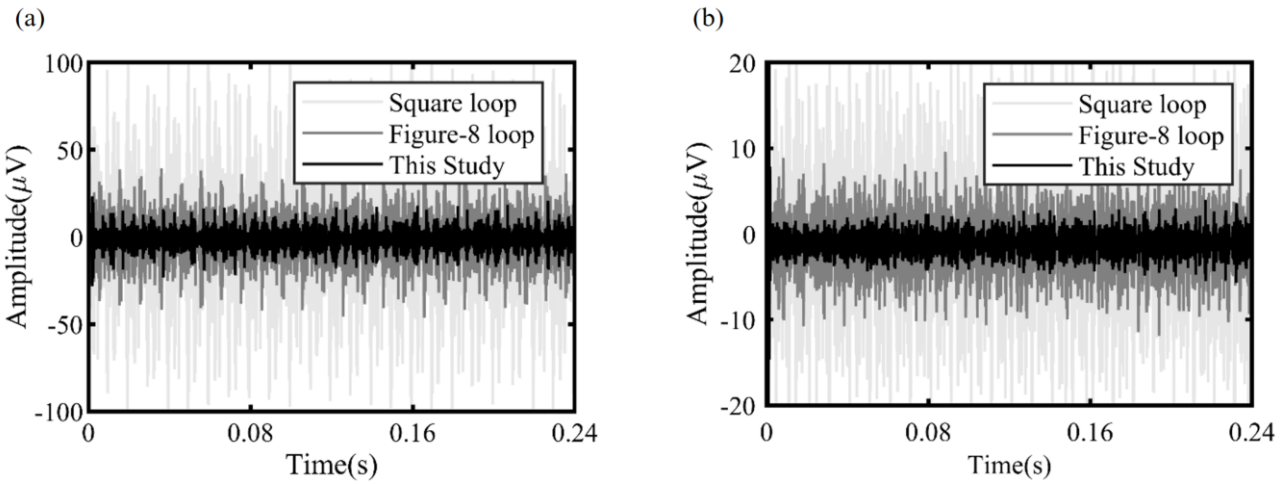

Figure 3: *emf*(*t*) in the three types of loops with different numbers of stacks. (a) No stack; (b) 16 stacks

CONCLUSIONS

It is necessary to reduce harmonic noise in MRS measurement, the effect of established methods has limited effectiveness. In this study, we demonstrate that it works better by using the special construction loop proposed above, and it can suppress the harmonic noise obviously in the time domain.

REFERENCES

A. A. Behroozmand, K. Keating, and E. Auken, "A review of the principles and applications of the NMR technique for near-surface characterization,"Surv. Geophys., vol. 36, no. 1, pp. 27–85, Jan. 2015.

J. J. Larsen, E. Dalgaard, and E. Auken, "Noise cancelling of MRS signals combining model-based removal of powerline harmonics and multichannel Wiener filtering," Geophysical Journal International, vol. 196, no. 2, pp. 828–836, 2014.

J. Lin, Y. Zhang, Y. Yang, Y. Sun, and T. Lin, "Anti-saturation system for surface nuclear magnetic resonance in efficient groundwater detection," *Rev. Sci. Instrum.*, vol. 88, no. 6, 2017, doi: 10.1063/1.4984295.

J. J. Larsen and A. A. Behroozmand, "Processing of surface-nuclear magnetic resonance data from sites with high noise levels," Geophysics, vol. 81, no. 4, pp. WB75–WB83, may 2016.

D. V Trushkin, O. A. Shushakov, and A. V Legchenko, "The potential of a noise-reducing antenna for surface NMR groundwater surveys in the earth's magnetic field1," *Geophys. Prospect.*, 1994, doi: 10.1111/j.1365-2478.1994.tb00245.x.

J. F. Girard, C. Jodry and P. D. Matthey, On-site characterization of the spatio-temporal structure of the noise for MRS measurements using a pair of eight-shape loops, *J. Appl. Geophys.*, vol. 178, 2020, doi: 10.1016/j.jappgeo.2020.104075.

Noise attenuation of magnetic resonance sounding signal using fully convolutional networks

Meng Wei **Yang Zhang** **Tiehu Fan** **Tingting Lin**

The College of Instrumentation and Electrical Engineering, Jilin University, Changchun 130021, China.
weimeng19@mails.jlu.edu.cn, yang_zhang@jlu.edu.cn, fth@jlu.edu.cn, ttlin@jlu.edu.cn

SUMMARY

Magnetic resonance sounding (MRS) measurements commonly suffer from a notably low signal-to-noise ratio (SNR). In recent years, many denoising methods have been developed which have demonstrated the useful capability to improve the SNR. However, the traditional methods that depend on signal models and the corresponding prior assumptions commonly rely on manual experience, which brings obstacles to the automation and efficiency of signal processing. To solve the above problems, we attempt to apply an intelligent denoising framework with fully convolutional networks (FCN) as the basic tool for deep learning. The network extracts the features of the MRS signal through the encoder and decoder layers of the FCN structure, in which residual learning is adopted to accelerate the training process and improve denoising performance. The experiments on field data show that the proposed denoising framework can automatically process noisy MRS signals and achieve a significant denoising performance.

Key words: MRS, signal processing, fully convolutional network, deep learning.

INTRODUCTION

Magnetic resonance sounding (MRS) is a geophysical technique for non-invasive detection of subsurface hydrological information that provides a quantitative determination of the water content distribution in the subsurface. However, the application of MRS is often limited due to the bad signal-to-noise ratio (SNR).

The noise interference in MRS measurement mainly includes spiky noise, power-line harmonic noise, and random noise. Many advanced denoising methods have been developed, which are summarized according to the noise classification as follows. The common methods used to remove spiky noise are the statistical stacking method (Jiang et al., 2011), the spike detection algorithm based on a nonlinear energy operator (Dalgaard et al., 2012), and the model-based spiky noise reduction method (Larsen, 2016). North filtering (Legchenko and Valla, 2003) and the model-based approach (Larsen et al., 2014) are proposed to suppress the powerline harmonic noise. In terms of the random noise, stacking is the most common method (Jiang et al., 2011). In addition, the time-frequency peak filtering is proposed for the random noise attenuation (Lin et al., 2011). The existing methods have been widely applied in MRS signal denoising, but the shortcoming of the methods are the need of prior assumptions of the MRS signal and noise, optimal filter parameter tuning and expensive time cost.

In this paper, we propose an intelligent denoising framework of MRS signal based on fully convolutional network (FCN). And the experiment has been conducted on the field data to test the FCN model can achieve an impressive denoising performance.

METHODS

The noisy MRS signal can be expressed by

$$y = x + n \tag{1}$$

where y, x and v are the noisy MRS signal, the effective MRS signal and the environmental electromagnetic noise, respectively. The basic idea of the proposed denoising model is to establish an end-to-end mapping relationship between the noisy MRS signal and the corrupted noise based on a neural network, as shown in eq. (2).

$$R(y_i;\theta) = \hat{v}_i \approx v \tag{2}$$

where R represents the residual learning network and θ contains network parameters. $\hat{v}$ is the estimated noise. To make $\hat{v}$ and v as close as possible, the common approach is to minimize the mean square error between the output noise data of the network and the expected noise data, which can be expressed as follows:

$$l(\theta) = \frac{1}{2N}\sum_{i=1}^{N}\left\|R(y_i;\theta) - (y_i - x_i)\right\|_F^2 \tag{3}$$

where $l(\theta)$ represents the loss function of the network; $R(y_i;\theta)$ is the corresponding output when the input is y_i, $\|\cdot\|_F$ represents the Frobenius norm, $\{(y_i, x_i)\}_{i=1}^{N}$ stands for the training data, and N is the number of data sets. After optimizing the network, the denoised signal can be expressed by

$$\hat{x} = y - \hat{v} \approx x \tag{4}$$

where $\hat{x}$ represents the denoised signal.

We adopt the FCN as the network architecture of the proposed denoising model, as shown in Fig. 1. The network consists of two parts, *i.e.*, encoder and decoder. The encoder is mainly used for feature extraction that transforms the input noisy signal into multidimensional feature maps. The decoder is a generator that reconstructs the output signal from the transformed feature maps. To concisely indicate the multilayer operation, the operations of the encoder are expressed in eq.(5):

$$Z = Encoder(Y) \tag{5}$$

where Y represents the input noisy signal to be processed, and Z denotes the feature map obtained by feature extraction from the input signal. Similarly, the operations of the decoder can be indicated as:

$$V = Decoder(Z) \tag{6}$$

where V represents the reconstructed noise signal from the feature map Z.

The size of the input layer of the network is a 1024. The depths of the encoder and decoder are both 10, which means that all of the depths of the conv, max pooling, upsampling, and deconv layers are 5. Because the network structure is symmetrical, the size of the output is also 1024. The number of training samples with each noise level is 1 million, and the noise set includes the artificial noise and the field noise. The proposed denoising network has been implemented in Python with TensorFlow support. The training of the network is performed using an NVIDIA 2080Ti GPU.

RESULTS

We apply the denoising network on the field data recorded from the North Lake, which is located in the suburbs area in Changchun, Jilin Province, China. The experiment was conducted on the JLMRS-III system developed by Jilin University. Fig. 2 provides an example of the denoised signal. Fig. 2 (a) show the noisy signal and the denoised signal processed by the FCN model in time domain, which shows that the model can suppress almost all three kinds of noise and that the denoised signal has an exponential decay trend. From the frequency domain and the time-frequency analysis in Fig. 2 (b)-(d), the effective signal is corrupted by spiky noise, powerline harmonics with frequency components of 2150 Hz and 2250 Hz exist, and random noise also occurs. And the corrupted noise was almost removed, and the effective signal was recovered. By calculation, the SNR of the recorded data is -13.4 dB and the SNR after processing increases to 12.6 dB.

CONCLUSIONS

To address the problem of the traditional denoising methods in processing produce, the proposed intelligent denoising framework of MRS signal based on deep learning is introduced. And we have verified that the FCN model can achieve good denoising performance when the network has been trained on large training dataset.

REFERENCES

Behroozmand, A. A., Keating, K. & Auken, E. 2015. A review of the principles and applications of the NMR technique for near-surface characterization. Surveys in Geophysics, 36(1), p. 27–85.

Jiang, C., Lin, J., Duan, Q., Sun, S. & Tian, B. 2011. Statistical stacking and adaptive notch filter to remove high-level electromagnetic noise from MRS measurements. Near Surface Geophysics, 9(5), p. 459-468.

Dalgaard, E., Auken, E., & Larsen, J. J. 2012. Adaptive noise cancelling of multichannel magnetic resonance sounding signals. GEOPHYSICS,. 191(1), p. 88-100.

Larsen, J. J., 2016. Model-based subtraction of spikes from surface nuclear magnetic resonance data. GEOPHYSICS,81(4), p. WB1-WB8.

Larsen, J. J., Dalgaard, E. & Auken, E. 2014. Noise cancelling of MRS signals combining model-based removal of powerline harmonics and multichannel Wiener filtering. Geophysical Journal International, 196(2), p.828-836.

Legchenko, A., & Valla, P. 2003. Removal of power-line harmonics from proton magnetic resonance measurements. Journal of Applied Geophysics, 53(2), p.103-120.

Lin, T., Zhang, Y., Yi, X., Fan, T., & Wang, L. 2018. Time-frequency peak filtering for random noise attenuation of

magnetic resonance sounding signal. Geophysical Journal International. 213(2), p. 723-738.

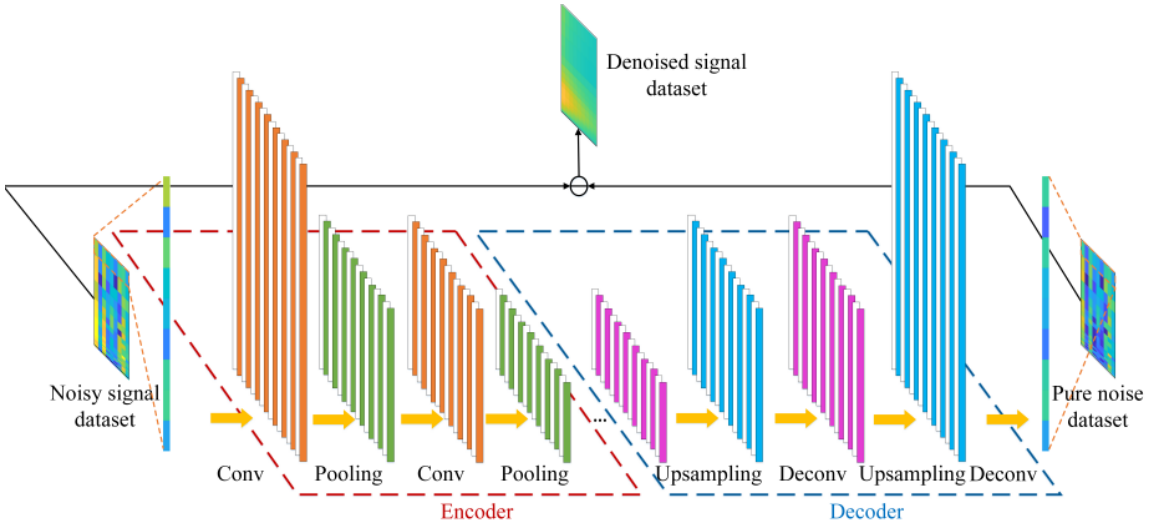

Figure 1. The structure of the FCN model.

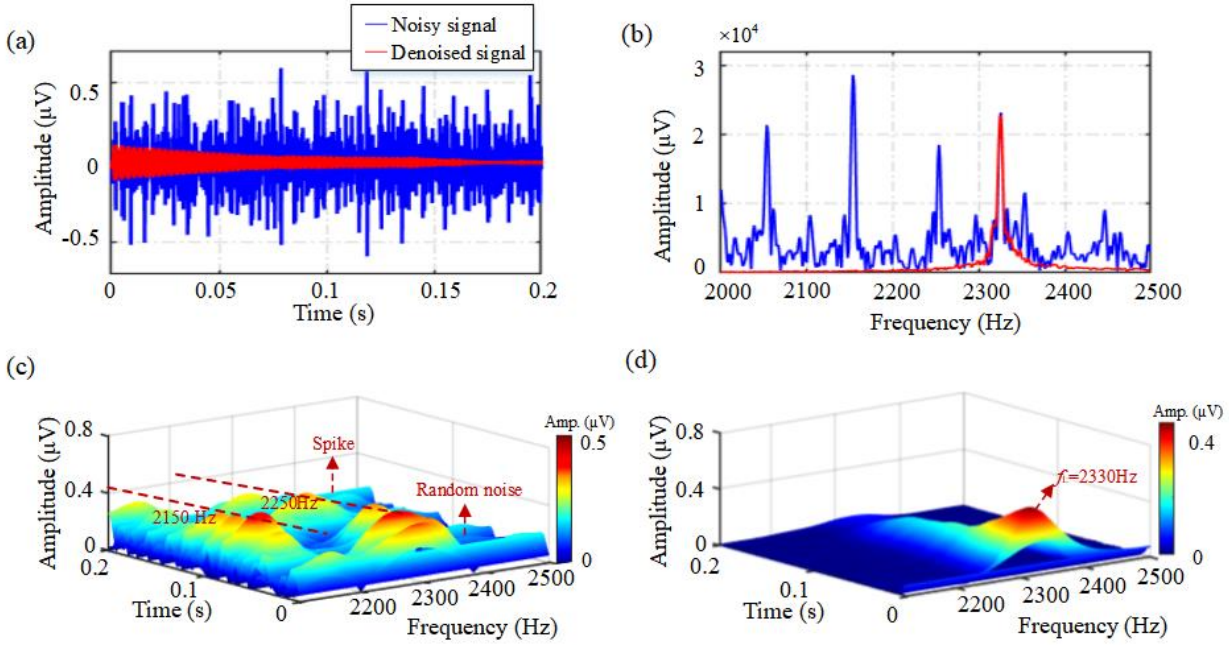

Figure 2. Denoising results of the FCN model. (a) The denoising result by using FCN model in time domain. (b) The spectra of the noisy signal and the denoised results. Time-frequency analysis of the noisy signal (c) and the denoised signal by using FCN model (d).

The Progress of Shutoff Circuit Design and Estimation for Pre-polarization SNMR Technique

Hanqing Zhao
College of Instrumentation and Electrical Engineering
Jilin University
Ximinzhu Street No.938, Changchun, China
hqzhao21@mails.jlu.edu.cn

Yujing Yang
College of Instrumentation and Electrical Engineering
Jilin University
Ximinzhu Street No.938, Changchun, China
yangyj16@mails.jlu.edu.cn

Kun Zhou
College of Instrumentation and Electrical Engineering
Jilin University
Ximinzhu Street No.938, Changchun, China
kunzhou19@jlu.edu.cn

Tingting Lin
College of Instrumentation and Electrical Engineering
Jilin University
Ximinzhu Street No.938, Changchun, China
ttlin@jlu.edu.cn

SUMMARY

The technique of surface magnetic resonance (SNMR) has been widely used for hydrological investigations by the advantage of locating the bulk of aquifer directly. However, the detected SNMR signals are limited to weak amplitude and are thus susceptible to environmental noise. In recent years, a pre-polarization (PP) pulse to significantly enhance the detected signals has been used in SNMR field applications. Meanwhile, the PP techniques and modelings are also introduced. In this paper, we further developed the present system and modelling. A fast controlling direct current shutoff circuit has been introduced based on the pre-polarization SNMR instrument to optimize the shutoff module, while a improved model is also considered to estimate the subsurface magnetization dynamics of polarized underground water. Overall, the research in this paper has practical value for the promotion of pre-polarization SNMR technology, especially under high-power transmitter conditions.

Key words: SNMR, Adiabatic Shutoff, Pre-polarization

INTRODUCTION

As a commonly used electromagnetic method for shallow aquifer measurements, the surface nuclear magnetic resonance (SNMR) technique has considerable potential for hydrological measurements, due to its direct sensitivity to groundwater (Roy et al. 2003; Legchenko et al. 2002). As the qualitative and quantitative characteristics, it also possesses great significance in the construction of public infrastructure for cities and towns, e.g., subways, bridges, and dams, as well as shallow engineering quality assessment and geological disaster prediction (Behroozmand et al. 2015). However, the weak responses of this method lead to difficulties for further extensions. Considering this problem, the polarization technology, which employs an extra static field to enhance the signal amplitude, has been introduced to this method, providing high-quality imaging results of 0-10 m shallow layers even in high-noise environments.

The pre-polarization technique has been considered to be applied to SNMR in 1997 (Callaghan et al. 1997). Some researches have assumed that PP is a supplementary strategy for surface SNMR, especially in certain cases, such as Antarctic conditions or for vadose zone monitoring. Nonetheless, due to technical limitations, field applications have been rare until recent years. Lin et al. demonstrated this method can be used for reliable exploration in the noisy environments that otherwise limit signal detection (Lin et al. 2017). Since then, researches and field applications about pre-polarization using in SNMR have been proceeded, and significantly advancing this technologies.

In this paper, we introduce the latest developments and progresses of pre-polarization system for Jilin University, which including the algorithm and hardware improved of pre-polarization magnetic field controlling.

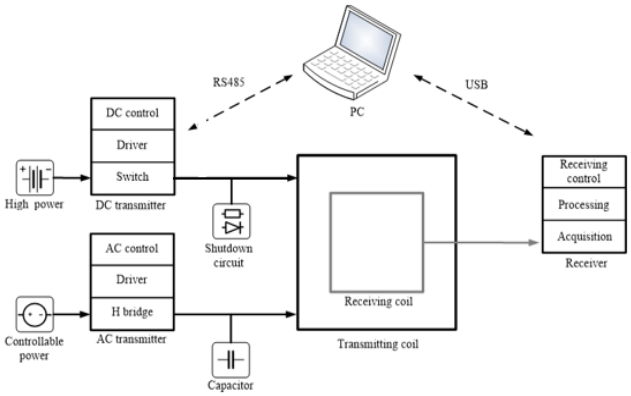

Figure 1. The overall structure block diagram of the pre-polarization SNMR instrument system.

PRE-POLARIZATION INSTRUMENT SYSTEM

Fig. 1 illustrates the schematic diagram of a pre-polarization instrument system, including transmitting coil (for direct current and alternating current transmitting), receiving coil and main control unit of signal detection. First, to enhance the macroscopic magnetic moments of hydrogen protons from M_0 (with only earth's magnetic field $\mathbf{B}_0$) to M_{Bp}, the transmitting coil forms a strong magnetic field $\mathbf{B}_p$ to pre-polarize the hydrogen protons by energizing a large direct current (DC). After $\mathbf{B}_p$ reaches a duration of about 4-8 s, shutdown the $\mathbf{B}_p$ field. Note that the shutoff circuit should control the DC pulse to shutoff in the form of adiabatic conditions, otherwise the pre-polarization effect will be greatly affected(Walsh et al.2011).

After that, the transmitting coil emits AC current at Larmor frequency lasting 20-40 ms, generating the excitation field $\mathbf{B}_{ac}$ to trigger the magnetic resonance phenomenon. After pulse terminations, the receiving coil will induce the enhanced electrical signals of SNMR, and then transmit the signal to the superior computer so as to obtain hydrological information through subsequent analysis of different AC pulses. During the measurement process, the main control unit monitors the running state of the system, completes the configuration of detection parameters with the upper computer, and controls the shutoff process of DC current.

OPTIMIZED RAPIDLY SHUTDOWN MODULE OF PRE-POLARIZATION CURRENT

According to the above instrument system, we focused on improving the polarization circuit module based on the traditional SNMR. Fig. 2 shows the schematic diagram of the polarized circuit and the synchronous shutdown circuit. In this case, the DC Tc was simplified as a series model of resistance and inductance. Then, the Insulated Gate Bipolar Transistors (IGBTs) connected in parallel were used as the fast switch to control the switching process of the polarization current of each DC Tc. Meanwhile, the Field Programmable Gate Array (FPGA)-based control circuit realizes the control of the drive circuit and the sampling of the polarization current, achieving the synchronous emission and shutdown of $\mathbf{B}_p$. Fig. 2b illustrates the passive SNUBBER circuit designed with multiple diodes and resistors, which attains the rapid release of the remaining energy of the DC Tc so that the shutdown process of the hydrogen nuclei in the aquifer meets the detection conditions.

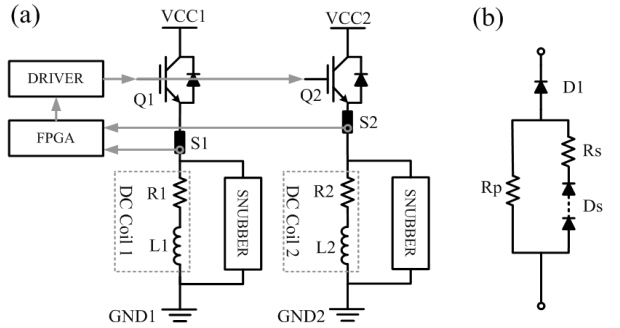

Figure 2. The schematic diagram of the polarized circuit and the synchronous shutdown circuit

The improved circuit parameters can adjust the shutoff time and ramp by changing the voltage value of capacitor C according to the actual requirements to achieve the ideal shutoff effect. Thus, the decay of $\mathbf{B}_p$ could be discribed by(Melton et al.2002)

$$\frac{\mathbf{B}_p}{\mathbf{B}_0} = k \cdot e^{-\tau/\Gamma} \quad (1)$$

where τ is a dimensionless variable, Γ is the exponential decay parameter. The corresponding fast adiabatic shutoff circuit is shown in the Fig.3.

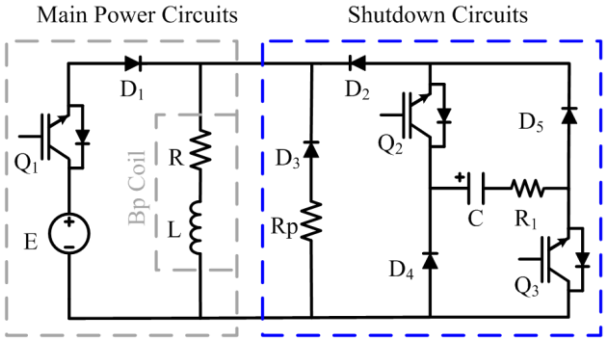

Figure 3. The corresponding fast adiabatic shutoff circuit

INSUFFICIENT ADIABATIC SHUTOFF IMPROVED MODELING

Notably, when the pre-polarization is introduced for SNMR, $\mathbf{B}_p$ provided by the surface DC coil produces an inhomogeneous magnetic field distribution with variational adiabatic conditions underground. As the energy-releasing circuit is built to satisfy the adiabatic condition constraints in most subsurface volumes affected by pre-polarization, the dynamic behavior of others protons can be investigated by solving the Bloch equation to improve the forward modeling precision:

$$\frac{d\mathbf{M}_{Bp}(\mathbf{r})}{d\tau} = \gamma \mathbf{M}_{Bp}(\mathbf{r}) \times \left[\frac{\mathbf{B}(\mathbf{r})}{B_0}\right] \quad (2)$$

where γ is the gyromagnetic ratio. Combining with Equation (1), we can expand the Bloch equation in three components:

$$\frac{dM_x(\mathbf{r})}{d\tau} = \frac{1}{B_0}[M_y(\mathbf{r})B_{pz0}(\mathbf{r}) - M_z(\mathbf{r})B_{py0}(\mathbf{r})e^{-\tau/\Gamma}] \quad (3)$$

$$\frac{dM_y(\mathbf{r})}{d\tau} = \frac{1}{B_0}\left\{M_z(\mathbf{r})\left[B_0 + B_{px0}(\mathbf{r})e^{-\tau/\Gamma}\right] - M_x(\mathbf{r})B_{pz0}(\mathbf{r})e^{-\tau/\Gamma}\right\} \quad (4)$$

$$\frac{dM_z(\mathbf{r})}{d\tau} = \frac{1}{B_0}\left\{M_x(\mathbf{r})B_{py0}(\mathbf{r})e^{-\tau/\Gamma} - M_y(\mathbf{r})\left[B_0 + B_{px0}(\mathbf{r})e^{-\tau/\Gamma}\right]\right\} \quad (5)$$

The above differential equations can be solved with the runge-Kutta method in variable step length and the magnetization of the insufficient adiabatic shutoff region can be obtained.

By comparing the 1-D kernel functions of the updated model with those of the previous model in Fig. 4, the differences can be observed for a 6-m-diameter square antenna with 8 turns for AC transmission and 30 turns for PP and receiving. For the pre-polarization pulse, a 300-A current is assumed to be applied for one turn with 5-ms shutoff considering the parameter $\Gamma = 8$. In comparison, the updated 1-D kernel displays lower sensitivity, especially at depths from -5 to -10 m, although the adiabatic condition is satisfied in most subsurface volumes. Consequently, the forward errors caused by insufficient adiabatic shutoff need to be considered and revised in certain cases.

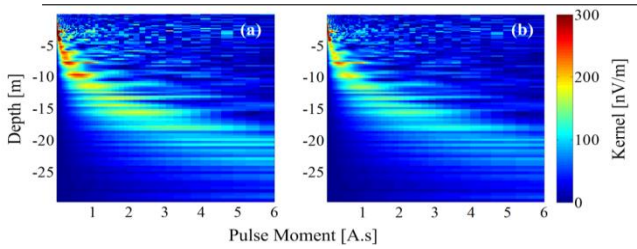

Figure 4. The 1-D kernel functions of the previous model(left) and updated model(right)

CONCLUSIONS

In this paper, we introduce the latest progresses of instrument system and modelling developments for pre-polarization instrument system. By optimizing the polarization fast shutoff circuit and forward modelling, the straightforward application of pre-polarization SNMR in high-noise environments can be further advanced.

REFERENCES

J. Roy and M. Lubczynski, "The magnetic resonance sounding technique and its use for groundwater investigations," Hydrogeology. J., vol. 11, no. 4, pp. 455-465, Aug. 2003.

A. Legchenko and P. Valla, "A review of the basic principles for proton magnetic resonance sounding measurements," Journal of Applied. Geophysics, vol. 50, DOI 10.1016/S0926-9851(02)00127-1, nos. 1-2, pp. 3-19, May 2002.

A. A. Behroozmand, K. Keating and E. Auken, "A review of the principles and applications of the NMR technique for near-surface characterization," *Surv. Geophys.*, vol. 36, no. 1, pp. 27–85, Jan. 2015.

D. O. Walsh, E. Grunewald, P. Turner, A. Hinnell, and P. A. Ferre,"Practical limitations and applications of short dead time surface NMR," *Near Surf. Geophys.*, vol. 9, no. 2, pp. 103–113, Apr. 2011.

Callaghan P T , Ec Cles C D , Seymour J D . An earth's field nuclear magnetic resonance apparatus suitable for pulsed gradient spin echo measurements of self-diffusion under Antarctic conditions[J]. Review of Scientific Instruments, 1997, 68(11):4263-4270.

Melton B F , Pollak V L . Condition for adiabatic passage in the earth's-field NMR technique[J]. Journal of Magnetic Resonance, 2002, 158(s 1–2):15-22.

Lin T , Yang Y , Teng F , et al. Enabling surface nuclear magnetic resonance at high-noise environments using a pre-polarization pulse[J]. Geophysical Journal International, 2017(2):1463-1467.

Author Index